UNIVERSIDAD DE SANTIAGO DE COMPOSTELA
FACULTAD DE FISICA
Departamento de Física de Partículas

Study of fast radiation-detectors based on fast halide scintillator crystals and their application to the CERN n_TOF experiment

María de la Soledad Robles Manzano
Septiembre 2016

USC
UNIVERSIDADE
DE SANTIAGO
DE COMPOSTELA

UNIVERSIDAD DE SANTIAGO DE COMPOSTELA
FACULTAD DE FISICA
Departamento de Física de Partículas

Study of fast radiation-detectors based on fast halide scintillator crystals and their application to the CERN n_TOF experiment

María de la Soledad Robles Manzano
Septiembre 2016

USC
UNIVERSIDADE
DE SANTIAGO
DE COMPOSTELA

UNIVERSIDAD DE SANTIAGO DE COMPOSTELA

Ignacio Durán Escribano, Catedrático de Física Atómica, Molecular y Nuclear de la Universidad de Santiago de Compostela,

CERTIFICA:

que la memoria titulada **Study of fast radiation-detectors based on fast halide scintillator crystals and their application to the CERN n_TOF experiment,** ha sido realizada por **María de la Soledad Robles Manzano** en el **Departamento de Física de Partículas** bajo su dirección y constituye el trabajo de **tesis** que presenta para optar al grado de **Doctora en Física.**

Santiago de Compostela, a 28 de septiembre de 2016.

Fdo. Ignacio Durán Escribano

Fdo. María de la Soledad Robles Manzano

Acknowledgements

The work of this PhD has involved the effort of many people and different laboratories: both the Experimental Group of Nuclei and Particles, GENP, at the Universidad de Santiago de Compostela and the n_TOF collaboration at CERN.

Firstly, I would like to thank my supervisor, Prof. Ignacio Durán for invited me to join the GENP group, specially when I was wondering why I used ^{152}Eu instead of ^{137}Cs and ^{60}Co to calibrate a detector in the students lab (if you continue reading this work, you will notice that using ^{152}Eu is still a good idea and indeed you can see nice europium spectra). Thanks Nacho for giving me this good opportunity to work in this field.

I can not forget the valuable help at the n_TOF collaboration of Eric Berthoumieux, Enrico Chiaveri, Nicola Colonna, Carlos Guerrero, Frank Gunsing, Andrea Tsinganis and Christina Weiss who made possible the setups and measurements carried out at the n_TOF facility. A special mention deserved to Emilio Mendoza and Daniel Cano for their help converting the files acquired at CERN and Jorge Lerendegui and Miguel Cortés for their help providing the simulation for the n_TOF spallation target.

I am very grateful to the PPACs experts: Laurent Tassan-Got, Laurent Audouin, Lou Sai Leong from IPNOrsay, Carlos Paradela from EC-JRC-IRRM, Diego Tarrío from Uppsala University and Ignacio Durán and Esther Leal from USC, who provided me the PPACs ROOT files for the coincidence analysis.

I specially thank Héctor Álvarez, Pablo Cabanelas and Paloma Díaz for their support with the simulations and David González for his wisdom and help when wrapping and encapsulating the crystals used in this work.

I can't forget the long and short discussions with Manuel Caamaño[1] about Physics and Metaphysics, specially about the fission process.

[1] Give me five!

I thank my collegues: Paloma Díaz, Noelia Montes (who guided my first steps in electronics), Martín Gascón (thanks for the scripts for the MCA and YOKO!), Yassid Ayyad (e Iris Ramos), Jossitt Vargas, Beatriz Fernández, Juan Ramón Pereira, Juan José Llerena (thanks for the spectra, all the lab stuff and the *Catalina* alias), Esther Leal, Diego Ramos, José Luis Rodríguez, David González, Carlos Paradela, Juan Alcántara, Diego Tarrío, Raquel Sorribas, Saúl Beceiro, Dolores Cortina, Marcos Seco (thanks for your valuable help with all my computers!), Vanesa Nimo and all the members of GENP for the stimulating discussions, for working together and for all the fun we have had in the last years.

Estos años no serían tan llevaderos sin los momentos pasados fuera del laboratorio y el despacho, gracias por todo a mis amigos de Santiago: Ana F., Ana H., Bárbara, Iria, Jose C., Jose (Oscar Luis), Marijose, Paloma, Pablo, Sofía y Teresa. A mis señoras de Almería: Carmen, Cristina, María del Mar, Marijose (¡gracias por ese respiro en Annecy!), Mariló, María Rosa (y el Sr. Nacho G.) y Soraya.

Gracias a Ángeles y Ramón, mis padres, que siempre me apoyan; sin ellos esto no sería posible. A mi hermano Gabriel y a mi familia, en especial a mis tíos José Luis, Maricarmen, Soraya, Gabriel y Carmen por su afecto y cariño. Y a ti, Gosha, por tu apoyo en todo, tu paciencia, los dibujos, los grandes momentos y los pequeños logros que compartimos.

"There is something breathtaking about the basic laws of crystals. They are in no sense a discovery of the human mind; they just are - they exist quite independently of us-. The most that man can do is become aware, in a moment of clarity, that they are there, and take cognizance of them."

-M.C. Escher

USC
UNIVERSIDADE
DE SANTIAGO
DE COMPOSTELA

Contents

USC
UNIVERSIDADE
DE SANTIAGO
DE COMPOSTELA

List of Figures

List of Tables

USC
UNIVERSIDADE
DE SANTIAGO
DE COMPOSTELA

Introduction

Nuclear experiments research require set-ups made of specific detectors as much accurate as possible in term of timing and energy resolution. This is the reason why new detectors should be developed taking advantage of the continuous advances in materials and techniques, to be used for detecting light nuclei, charged particles and γ radiation produced in nuclear processes. Most of them are based on the use of scintillation materials either plastics or inorganic crystals. The aim of this study is the characterisation of different nuclear detectors based on scintillation crystals and their possible uses in the detection of γ radiation from nuclear processes such as nuclear fission and neutron capture.

Along middle last century many studies of the scintillation detectors have been carried out [18]. Moreover, in last decade, the improvement of the crystal manufacturing and the new developed photodetectors has led to improvements in calorimetry, energy resolution, particle identification and timing resolution.

The radiation detectors based on inorganic crystals that are studied in this thesis work are: $CeBr_3$, CsI(Na) and CeF_3 scintillator crystals coupled to different photodetectors such as new photomultiplier tubes and PIN diode. In addition to this, very fast plastic scintillators were used to provide ultra-fast coincidences in order to discriminate charged particles from γ-rays. These detectors have been tested both in the detector development laboratory placed at Santiago de Compostela University (USC) and in the n_TOF facility at CERN, in Geneva, Switzerland.

Thesis structure

Chapter 1 explains the main problems when using fast detectors, particularly, fast scintillator detectors and proposed a number of solutions, both

in the hardware and in the software, to overcome those difficulties, such as the design of a shaping stage, a modified voltage divider to adapt the dynodes of a photomultiplier for hardware solutions as well as a set of software algorithms to performed Pulse Shape Analysis (PSA).

Chapter 2 contains the description of the fast scintillator detectors used in this work and as well as the simulation work of the scintillator crystals, $CeBr_3$ and CsI(Na), to calculate the γ-rays detection efficiency and the energy deposited by β particles.

In Chapter 3 the results obtained by the application of the solutions proposed in Chapter 1 such as the energy resolution, linearity and timing study as well as the PSA devoted to each the detectors are presented .

Chapter 4 is devoted to the measurements performed at the n_TOF experiment at CERN. A description of the facility is giving. The results obtained for the study of prompt γ-rays from radiative neutron capture reaction, (n,γ) for the isotopes ^{197}Au and ^{nat}Ag and nuclear fission induced by neutrons, (n,f), for ^{235}U reaction in coincidence with a PPAC chamber. Last section contained, the γ-flash effect and its characterisation is giving using the scintillator studied in this work.

Finally, the main conclusions are exposed and a seven Appendices are included at the end.

1. Hardware and Software solutions for fast scintillator detectors

In the quest for higher accuracy in the nuclear experiments, modern detectors and modern digitizers are often dealing with fast signals close or beyond 1 GHz, having a rise time lower than 1 ns. Thus, when developing the corresponding experimental set-ups, special care must be taken with these fast signals in order to hold all their available information. Particularly, concerning the shaping and the transmission of the electrical signals, more sophisticated rules than the elementary Ohm's Law are needed to simulate and improve these requirements. After Heaviside, it is commonly known that electronic components may be characterised through their resistance, capacitance and inductance being a complex impedance function of the signal frequency. However, the full Maxwell-Heaviside equations are not only hard to deal with, but sometimes non-useful, as the electronic components have not an easily known complex impedance. Its highest frequencies damping is not linear and, moreover, they are embedded in their environment that produces spurious parasitic impedances being almost impossible to characterise.

Nowadays, the CAD tools allow to reproduce in a quite realistic manner the behaviour of components, but its environment is still difficult to model. Moreover, as every detector shows some specific constrains, a trial-and-see method should be required and so some intuition is needed when looking for the optimal solution. In the following sections the main characteristic parameters of fast detector signals are mentioned and the software and hardware solutions adopted for the detectors used in this thesis work are described.

Firstly, the here used definition of the main characteristics of a pulse signal are given [19]:

- **Baseline** is the reference in terms of voltage or current to which the

signal pulse is digitised. Commonly the value for this reference is zero, however, it can be a different constant value and very often the tail of the signals affects the apparent baseline for the next signal, requiring specific hardware or software handling.

- **Pulse height or Amplitude.** It is referred to the distance in voltage or current from the baseline to the most highest absolute value (positive or negative) that the signal pulse achieves.
- **Rising Edge** is the transition from the low to the high amplitude values.
- **Falling Edge** is the transition from the high to the low amplitude values.
- **Rise time** is the time interval in which the signal amplitude evolves from the minimum to the maximum values. The most common definition is the time interval that takes the signal increases from the 10% to the 90% of its amplitude.
- **Fall time** similarly to the rise time, the fall time is most commonly defined as the elapsed time, between the 90% and the 10% of the amplitude when is decreasing.
- **Signal width** is defined as the elapsed time above 50% of its amplitude. It is commonly called: Full Width Half Maximum, onwads FWHM.

Problems related to very fast scintillator crystals coupled to PMTs. Some scintillation crystals recently becoming widely used, as, for instance, Lanthanum halides, BaF_2 or $CeBr_3$, have a huge Light Yield (L.Y.) with a very fast main component. When coupled to high-Q.E. (Quantum Efficiency) and high-gain Photomultiplier Tubes (PMTs), a very high current-peak associated with the rising edge of its signal pulse is produced. This current peak is very short in time (< 1 ns) and can be more than two orders of magnitude larger in amplitude than in typical scintillators. This is a challenge for the traditional Voltage Divider (VD) in the PMTs, making it non-linear and it creates a problem to the signal processing chain.

The peak of current originated by the fast component of the high L.Y. produces a sudden change of the bias voltage in the dynodes chain. This

change is, obviously, larger in the last dynodes and leads to a deviation from the linear behaviour of the PMT's gain. Moreover, the electron swarm, when going from the last dynode to the anode, creates a distortion of the electric field, leading to a dramatic miss-function of the whole PMT that remains unable to reproduce the original shape of the scintillator L.Y. This is a well known problem, having known remedies for pulses wider than a few nanoseconds. But narrowest pulses or more generally, those having a rise time of the order of a nanoseconds, need specific solutions.

On the other hand, these pulses, so short in time, create specific problems when analysed by the standard spectroscopic chains, that were designed to deal with signal timings of the order of few microseconds.

The output signal provided by the scintillator detectors, neither for CsI(Na)-PMT nor for $CeBr_3$-PMT, do not match the specifications of the standard spectroscopic chain, leading to undesirable non-linear effects, as it will be described in detail in Chapter 2. In Fig. 1.1 such effects can be appreciated, comparing three different SA models: CANBERRA Mod. 2022 [20], C.A.E.N. Mod. 968N [21] and ORTEC Mod. 570 NIM modules [22]. The ACQ system consisted on a Multichannel Analyser (MCA) from Amptek Inc. that acquired the spectra of the energy deposited by different radioactive sources. It can be seen how the channel/energy relation is not correct, as the higher energy peaks appears at channels lower than expected. In Fig. 1.1, the spectrum (a) shows a clearly non-linear effect as the energy ($\equiv$ *channel*) increases and the subsequent distortion of the shape of the photopeaks, and consequently their FWHM, that provides a wrong value of the resolution. In spectra (b) and (c) the most energetic peaks, $E \geq 1MeV$, do not appear in the spectra, observing in both cases a peak that corresponds to a saturation of the SA.

It is worth mentioning that such as non-linearity has been reported by number of previous authors, even suggesting to apply non-linear corrections Ref. Moreover, this effect is also found not only in analog standard spectroscopic chains, but also in digital sampling systems where the linearity of their input amplifiers should be not guarantee for frequencies beyond the GHz. In the following are described the different solutions taken into account along this Thesis work to deal with these different problems found when studying fast scintillator detectors.

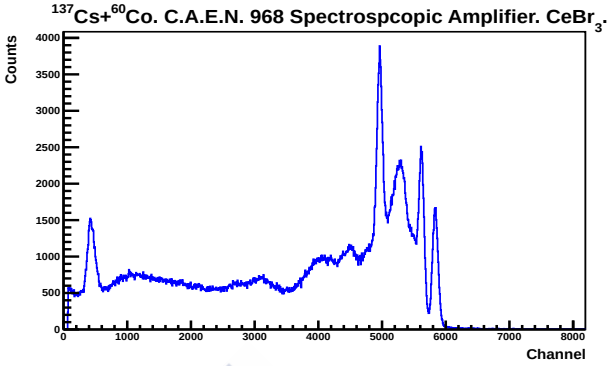

(a)

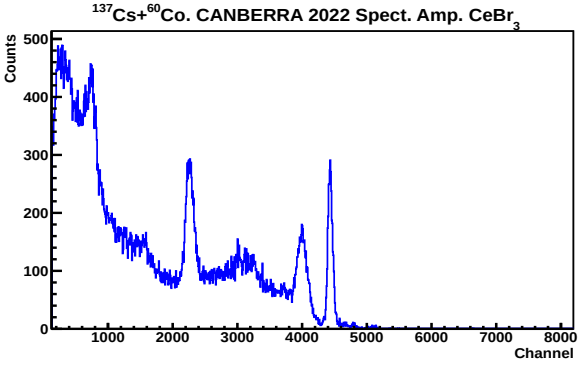

(b)

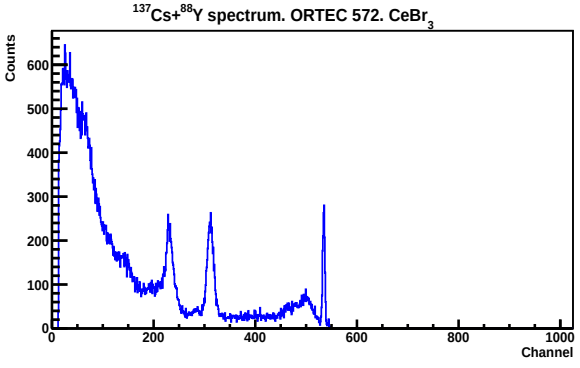

(c)

Figure 1.1.: The non-linear behaviour can be appreciated when the signals were not previously conditioned. ^{137}Cs+^{60}Co ((a) and (b)) and ^{137}Cs+^{88}Y (c) spectra measured with different standard spectroscopic amplifiers.

1.1. Hardware solutions

The challenge of dealing with a very high current peak produced in the optodevices by high-performance fast scintillator crystals, requires specific hardware solutions. Concerning PMTs, it was already commented the relevance of the design of the VD chain and how it influences the signal fidelity regarding the original shape from the scintillator. Furthermore, the sooner the signal is well shaped without loosing information on the relevant observables, the lower the undesired effects should be produced in the rest of the front end electronic chain.

The first temptation one has when dealing with such a fast crystals is lowering the HV in order to reduce the gain of the PMT. But reducing the gain results, in any case, in a reduction of the spectroscopic resolution and if the HV reduction is severe the resolution deteriorates even more by the fact of a bad focusing of the photo-electrons in the first stage. Some PMT manufactures suggest to use a Zener-diode in the first link of the VD chain, instead of a resistor, allowing so a certain margin of gain control without de-focusing the first stage. Other PMT manufacturers produce active chains, having transistors in the three last links of the chain, improving so the linearity for large pulses. Some users decide to pick-up the signal from the next to last dynode and reducing in consequence the load resistor at the anode, leading so to a better behaviour of the electron swarm in the last stage. Finally, there is the possibility of using an active circuit to reduce the gain in the last stages when a big scintillation is detected in the first ones.

Most of these remedies achieve very limited success when the raising edge of the scintillation is lower than 1 ns and very often create a ringing effect in the rest of the pulse.

An easy solution, used in this work with the $CeBr_3$ crystals, is to modify the VD by reducing the voltage in the last stages without changing it at the first ones. To do this, the penultimate and the ante-penultimate resistors were reduced by a factor of two and, besides this, reducing the HV in consequence to get a gain's reduction without affecting the focussing potential at the first dynode. In addition to this, when dealing with ultra-fast crystals, a commonly useful trick is to put a capacitor in parallel

with the load resistor. This capacitor acts reducing the impedance of the anode's load mainly for the higher frequencies.

It is worth discussing on the convenience of reducing the high frequency components by a capacitor in parallel with the anode's load. As a first advice one must refrain from using components in the VD (neither resistors, capacitors, diodes nor transistors) not being specified for frequencies well beyond the GHz range (normally, the SMD components used in fast electronics are compliant with, but most of the resistors and capacitors found in the shelves are not). Should the appropriate capacitors been used, the first observed effects are the slowing down of the rising time and the reduction of the peak amplitude. These effects seem to worsen the quality of the output pulse (both time and amplitude resolution should be affected) but this is not the case when both the extremely short rise time and the extremely high amplitude are creating a bigger trouble. In fact, the finally got time resolution depends on both the rise time and the time resolution of the Front End Electronics (FEE), in such a way that sending extremely fast signals to the FEE, paradoxically, does not result in a better time resolution and results in a poorer energy resolution. This is partly due to the fact of the higher frequency components of the signal not being well managed neither by the cables nor by the FEE. Concerning the amplitude of the pulses, the use of a well suited capacitor does not entail a loss of information on the energy deposited in the crystal, because the PMT's output is a current signal and all the charge integrated in the capacitor is always given back, provided we are using low loss HF components. Should the RC time constant become well adapted to the signals we are dealing with, both time and amplitude resolutions rest undamaged.

Problems produced by fast signals in cables and Front-End Electronic, FEE. The main effect produced in cables is a worsening of the Signal-to-Noise Ratio (SNR). Obviously, the longer the cable is the worst the SNR will be. Firstly because of the attenuation of the Very High Frequency (VHF) components, and secondly because cables are a source of noise, even if coaxial ones were used.

The connectors type and the electrical specifications of the cables take part in the propagation of the signal in an appropriate way, i.e., neither

producing loses nor modifying its shape. Most of the cables used in the nuclear experiments have loses. The larger the frequency is, the more the loses causes by propagation are. That means that signals whose frequency is less that decades of nanoseconds, the loses by propagating along the cable will be larger.

The attenuation is produced by the non-linear behaviour of the cable impedance, being function of the signal frequency spectrum. The wire resistance is affected by a spurious inductance and the capacitance by the so-called dielectric that insulates the wire and the grounding. Actually, the insulator is made of a material having a non-linear behaviour, neither in frequency nor in amplitude, in such a way that the nominal capacitance appears as having a non-linear ohmic resistance to ground. This is degrading so both the amplitude and the shape of the original signal. The specifications of cables and connectors must so match the shaping of the fast-detector output, and SMA standard connectors and cables must be used instead of LEMO or BNC standard ones, when required. Once again, the advantage of dealing with signals not having frequency components above few GHz becomes obvious.

A second effect due to coaxial cables is the fact of they are linking the ground of both the sending signal system and the receiving one. It is worth noting that all the current flowing in one direction through the signal wire must return via the cable ground mesh. This is specially relevant when dealing with a huge number of fast signal channels, because they produce peaks of current that disturb the ground system. Of course, the higher the frequency of the signal is, the more severe are the problems created in the ground systems. A commonly proven solution is the use of twisted-pair cables were both wires are floating and so there is no ground links. Moreover, in the twisted-pair configuration, both wires are picking-up the same noise, that cancels when reading in a differential mode. The use of HF twisted-pair cables is highly recommended, as far as possible.

1.1.1. Voltage Supply Network

PMTs having a high Q.E. and a high gain, when coupled to high L.Y. $CeBr_3$ crystals produce a high current signal peaks because of its short

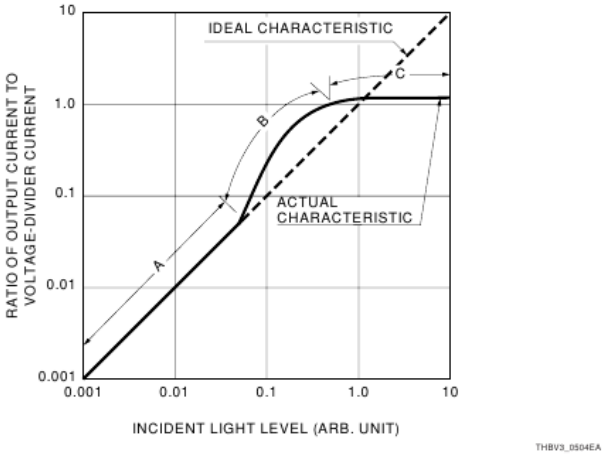

Figure 1.2.: Response curve of a PMT as a function of the Light Yield. Ideally the response is linear, shown with a dashed line. The solid line shows the non-linear relation for high Light Yield. (Figure courtesy of Hamamatsu Photonics K. K. [1]).

rising time and very fast decay component (see Table 2.1) that create a huge number of photoelectrons in the photocathode in a very short period of time. As a consequence it was commented above, the dynode stages saturated leading to a degradation in the output linearity.

To solve this problem a new VD was designed. To assure a low SNR factor, this development was done based on D Type Socket Assembly Normal Divider mod. E5996 from Hamamatsu [23] (see Fig. A.1 (left) in Appendix A).

1.1.2. Bias voltage curve

Hamamatsu Photonics provides a exponential correlation of gain versus the voltage supplied (see Fig.1.3) to the PMT R7600U-200 for the standard VD circuit (see ref [23]). The newly designed VD circuit, requires a new calibration and two measurement methods have been carried out for this purpose:

The first method consists on the acquisition of the detector output signal

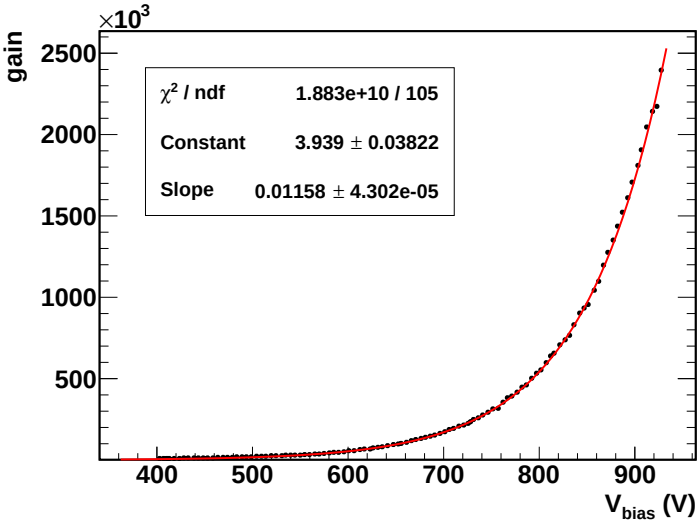

Figure 1.3.: Gain vs Voltage Supply of the PMT R7600U-200+E5996 socket. Courtesy of Hamamatsu Photonics K.K.

directly connected to a YOKOGAWA oscilloscope [24]. A large amount of pulses were acquired for every value of a set of supplied voltages so long as the $CeBr_3$-PMT was irradiated by a ^{137}Cs radioactive source. Clearly, the amplitude of the signal is proportional to the charge produced in the PMT, and therefore, to the gain. Then, the waveform of every pulse was analysed using a digital algorithm, (which will be explained in detailed in Chapter 2) to find out the relation between the maximum amplitude of every acquired pulse and the supplied voltage supplied to the PMT.

The observable maximum amplitude, related directly to the PMT gain, and the voltage supplied correlation is proportional to the gain vs. voltaged supplied correlation provided by the manufacturer, following an exponential dependence. See Fig. 1.4 (a).

The second method is based on the correlation between the centroid of the ^{137}Cs radioactive source spectra acquired using a spectroscopic measurement chain (that will be explained in detail in following sections in Chapter 1) consisting on several active stages: an electronic preamplifier, an spectroscopic amplifier mod. 2022 manufactured by CANBERRA and

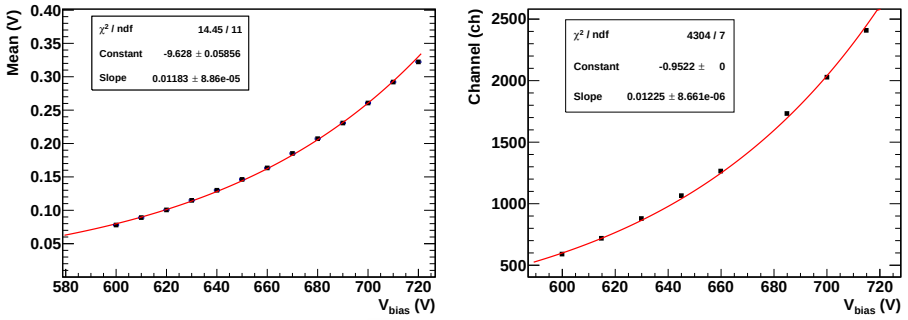

(a) **(b)**

Figure 1.4.: Maximum pulse amplitude vs supply voltage of the PMT R7600U-200+USC-VD, measured using PSA of signals recorded with a YOKOGAWA oscilloscope (a). Centroid for 662 keV γ-rays froam a ^{137}Cs vs supplied voltage measured with a spectroscopic measurement chain: preamplifier, shaper, spectroscopic amplifier and multichannel analyser (b).

a MCA from AmpTek. This analysis of the centroid of the photopeak of 662 keV γ-rays from ^{137}Cs. confirms the exponential dependence as well. See Fig. 1.4 (b).

1.1.3. Spectroscopic chain measurements

In nuclear physics experiments, besides simply detect the production of a certain events (counters), one could need to measure some specific observable magnitudes such as, for instance, the time (timers), the deposited energy (spectroscopic analysers), the signal shape (Pulse Shape Analysers, PSA), or any combination of them. The electronic pulses must so be adequately handled in order to preserve its characteristics related to the observables of interest.

When dealing with spectroscopic analysers, a typical set-up consists on mainly five different stages: the detection system, the preamplification stage, the shaping amplifier, the spectroscopic amplifier (SA) and the acquisition system, as sketched in Fig. 1.5.

The detector produces either a voltage or a current signal (see Refs. [19, 25]) or very often something intermediate, and so the preamplifier must be specifically chosen to match the detector output. A typical voltage signal should be coupled to an extremely high-impedance input amplifier whereas a typical current signal will require a low-impedance input to drain the charge produced by the detector. Commonly, the output impedance of the detector is a complex impedance and so the preamplification stage can be seen as an active filter, adapting the input/output impedances (transimpedance). It must be placed as close as possible to the detection system to avoid unwanted effects due to the stray capacitances of cables. Shaping amplifiers are used to amplify the signal modifying its shape to make it appropriate to the rest of FEE. Tipically, the SA's, on top of its amplitude gain, manage parameters such as the polarity, the timing, the shape, and also perform a baseline restorer in order to condition it for the down stream spectroscopic ADQ system. The spectroscopic systems usually consists on a MultiChannel Analyser (MCA) or an Analog to Digital Converter (ADC), as it will be shown in Chapter 3 and Chapter 4.

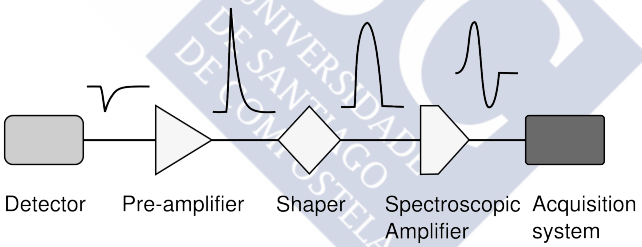

Figure 1.5.: Typical measurement chain for measuring the deposited energy, called spectroscopic chain. It consists on five stages: the detection system, the preamplifier stage, the shapery amplifier, the spectroscopic amplifier and finally, the acquisition system. The evolution and modification of the signal is schematically represented in the line.

1.1.3.1. Non-linearity effects

To overcome the problem of lack of linearity when the time characteristics of the analog signal from the detectors were not matching the specifications of the SA and the MCA, a hardware solution is proposed.

Since the non-linearity effects observed are due to a problem of signal conditioning, the characteristics of the output signal from the optodevices coupled to the scintillator detectors must be cope with the specifications of the spectroscopic amplifier (SA); otherwise, when designing the electronic chain, an specific shaping stage must be implemented.

The spectroscopic amplifier chosen for that purpose is the CANBERRA Mod. 2022 whose main requirements for the input signals are[20]:

1. Signal polarity: positive or negative pulses.
2. Rise time less than shaping time chosen: $<$0.5 μs, 1 μs, 2 μs, 4 μs, 8 μs or 12 μs.
3. Decay time larger than 40 μs for 0.5 μs, 1 μs, 2 μs, 4 μs, 8 μs or 100 μs for 12 μs.
4. Amplitude $\pm$10 V divided by the selected gain for linear response.

Regarding the output signals from both $CeBr_3$-PMT and CsI(Na)-PMT scintillator detectors in Figs. 3.18 and **??** respectively, it is noticeable that both decay times -around 30 ns and 600 ns respectively- are below the required by the SA CANBERRA Mod. 2022 specified in the requirement 2.

***Stretcher* Printed-Circuit-Board design** To be consistent with the discussion above, the following considerations were taken into account when designing the shaping circuit, that in following is called *stretcher*:

1. The conditioned signal must maintain proportional to the observables to the initial signal.
2. The decay time of the conditioned signal must be at least 500 ns.
3. The used components must be appropriate for the frequencies of the initial signal and the subsequent ones (see Appendix B).

The designs of the both *strecher PCBs*, one for $CeBr_3$-PMT another for CsI(Na)-PMT, were simulated using the software package OrCAD 10.5 [26] including, among other programs, PSpice, Capture CIS and Layout Plus. A detailed explanation of the designs can be read in Appendix C. Fig. 1.6 shows the *strecher PCBs* for $CeBr_3$-PMT detector.

The non-linear spectra, badly obtained without its specific signal conditioning stage, avoid an appropriate characterisation of the response of the scintillator detectors in terms of resolution and linearity. Concerning the energy resolution, it can be calculated by the Eq. 1.1

$$R(E) = \frac{FWHM}{E} \times 100 \equiv \frac{2.35\sigma}{E} \times 100 \tag{1.1}$$

where E is the energy deposited in the detector, the Full Width High Maximum (FWHM) must be given in the same units as E and is related to the standard deviation for peaks whose shape is Gaussian, as it is most often the case of the spectra peaks from radioactive sources. Consequently, good linearity is needed to provided an accurate value of the energy resolution as it was explained above.

The different *stretcher PCBs* were done to solve these problems, conditioning the output of the scintillator detectors by taking into account the requirements of the SA. Both *stretcher PCBs*, for $CeBr_3$-PMT and CsI(Na)-PMT, provide linearity after the signal passing the SA, solving the problem discussed previously. In Fig. 1.7 a ^{137}Cs and ^{60}Co spectra for $CeBr_3$-PMT and CsI(Na)-PMT respectively are shown, without having the non-linear effects present in Fig. 1.1 are solved.

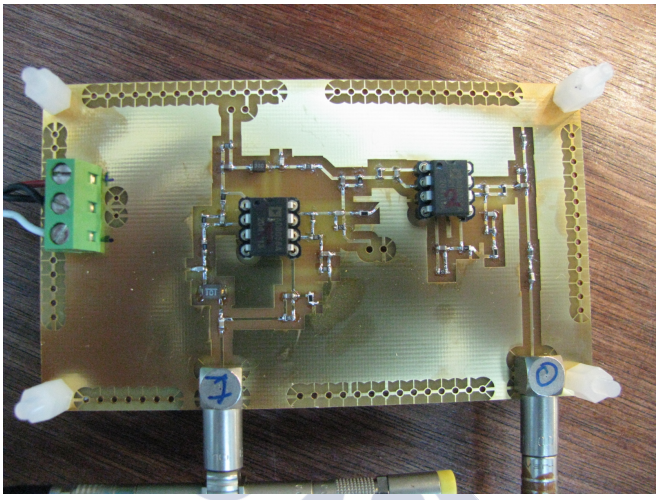

(a)

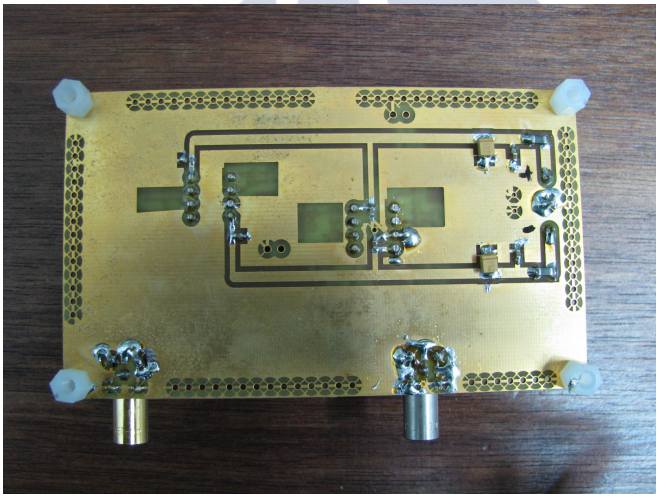

(b)

Figure 1.6.: *Strecher* Printed Circuit Board for $CeBr_3$-PMT detector. (a) Top layer, (b) Bottom layer

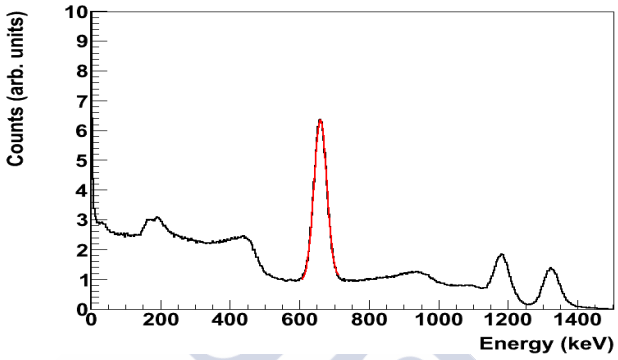

(a)

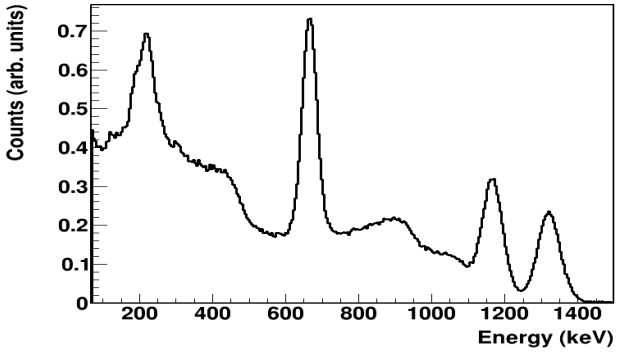

(b)

Figure 1.7.: ^{137}Cs+^{60}Co acquired using the *strecherPCBs* for signal conditioning of $CeBr_3$-PMT, (a), and CsI(Na)-PMT, (b). The non-linearity problems are solved.

1.1.4. Attenuator design

Into the frame of this thesis work, when trying to disentangle the n_TOF γ-flash puzzle (detailed described in Chapter 4) , several test were done by putting scintillator crystals exposed to the neutron beam halo radiation. At these points a very wide energy spectrum was detected due to both γ-rays and charged particles, mostly related to the spallation target γ-flash. At n_TOF, the acquisition systems has an acquisition scale up to 5 V, maybe 10 V, that implies that the amplitude of detector signals can not overshoot this amplitude barrier.

A solution to these drawbacks is presented in this section. The proposed hardware design is an attenuator based on Zener diode.The Zener diode used in the design is the D2W047 manufactured by Panasonic [27]. The main characteristics of this electronic component is its ability to behave as a extremely high impedance for signals whose negative voltage amplitude is comprised, nominally, between 0 and -4.7 V, having at this breakdown voltage a sharp knee, going its impedance down to a low and almost constant value.

The system acquisition available in the n_TOF experiment have the characterics to choose the sampling of the ADCs. The following design (see Appendix D) is proposed:

Advantages:

1. A slightly shaping of the rise time is made in consequence, the number of sampling is larger to the posterior pulse analysis.

2. Signals higher than the Zener breakdown are attenuated.

The design have been simulated using PSpice program in the OrCAD 10.5 framework. The pulses were simulated using a double exponential voltage source: the rise time corresponds to a rising exponential function and a the decay time corresponds to a decreasing exponential function. The parameters of the simulated source were chosen in order to match the output signal for the CsI(Na)-PMT scintillator detector. The attenuation effect is observed, in Fig. 1.8 showing the relation of the output pulse height and the amplitude of the input signal. The results of the proper operation of the attenuator are shown in Chapter 4.

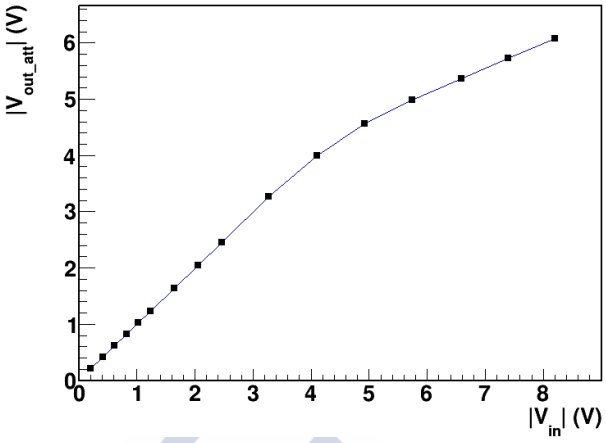

Figure 1.8.: Amplitude of simulated output signa of the attenuator based on Zener diode depending on the pulse height input signal for CsI(Na)-PMT scintillator detector

1.2. Algorithms for digital signal processing

The digital information of the pulses stored by flash-ADCs has to be accessed and analysed in a systematic way, in order to extract its useful information. This is usually done off-line, and, for that purpose, pulse shape analysis (PSA) algorithms are widely used. Output of these programs are, for instance, the digitised pulse area, width, amplitude or time of arrival, after dealing with baseline shifts and noise.

Problems observed when digitising fast signal using flash-ADC acquisition. Once the best-shaped analog signal arrives to the front-end data acquisition system, flash analog-to-digital converters, onwards fADC, are the faster way to digitise it. Based on a cascade of in parallel comparator circuits whose number is determined by the resolution given by the number of bits, 8-10 bits in the most of the cases, of the circuit, are suitable for applications requiring very large bandwidths. Considerable power consumption, low resolution and higher cost may be considered as their main disadvantages.

The sampling frequency, f_s, of the fADC must agree with the Nyquist-Shannon sampling theorem (see Ec.1.2) in order to reproduce the analog input signal with a frecuency f_H, as closely as possible.

$$f_s > 2 \cdot f_H \tag{1.2}$$

The major problem when analog signals are to be digitised, concerns the sampling of the high frequency rising flanges (either the one coresponding to the signal or to the noise spikes): a poor sampling frequency means few number of samples to reproduce the critical part of the input signal and thus, increasing the uncertainty to measure the observable rise time. [28]. Therefore, fast signals require sampling frequencies above hundreds of MHz or GHz, as well as a good optimisation of the design of the sampling clock.

The parameter design, resolution, number of bits to quantify the signal amplitude is also crucial to reduce the uncertainty of the off-line analysis of the digitised signals. The more number of bits, the less uncertainty will be in the quantisation process. In the particular case of signals coming from a radiation detector, a scarce quantisation of the signal amplitudes means a loss of energy resolution, which is related to the height of the signal.

Moreover, if the analog signal to be digitised comes from a fast PMT detector, whose frequency associated to the rise time is larger than the f_S given by the fADC, a signal smooth should be a solution to decrease the rise time frequency. This smooth solution consists on welding a low value resistance using the serial method in the output cable what will produce a slight signal integration together with the stray capacitance of the coaxial cable.

Therefore, both sampling rate and quantisation must be appropriate to digitise the analog signal accurately.

The linearity of the acquisition is an important issue: in the case of the charge input signals non-linear effects might exist which implies a non precise reproduction of the original analog signal. On the other hand, concerning the long intervals of the clock time stamp, non-linear effects can

be observed and may introduce uncertainties in that cases, when absolute time measurement is relevant as for instance in case of time-of-flight technique.

1.2.1. Raw signal analysis

PSA methods can be classified following a simple criterion based on whether signal was conditioned or not. The later are the so-called raw signal algorithms. The most common procedures for such an analysis are based on the direct comparison to known waveforms. The former methods are based on signal conditioning, often called filters, for simplicity. That means that the recorded waveform undergoes a transformation which enhance certain properties of the signal but, sometimes, others can be reduced. The most common filters are the Finite Impulse Response (FIR) and the Infinite Impulse Response (IIR) filters. FIR filters are well defined in time and the response ends but in the other case, the presence of feedback can lead to an infinite response function or oscillation. This work will be focus on FIR filters.

The raw signals produced in radiation detectors contain information about the incident radiation and the definition of observables, such as the pulse height, the rise time or the pulse area, becomes of interest when asking the ability of the detector to resolve, for instance, the time of arrival, the deposited energy or the pulse shape of the raw signal, that varies depending on the kind of the incident radiation because of the interaction type with the detector material.

Normally, the intrinsic noise induced in the detector and the conditioning electronics worsen the SNR leading to complicate the analysis of the original signal. The FIR filters described below help to improve the SNR ratio still conserving the information on the raw signal observable.

1.2.2. FIR filter

Digital filtering of discrete-time signals is done by performing a discrete convolution of the form:

$$y[n] = (f * g) = \sum_{m=-\infty}^{\infty} f[n-m] \cdot g[m] \tag{1.3}$$

where f is the convolution function, commonly called *kernel*, and g is the input. Concerning FIR filters, function f is replaced by a set of N coefficients, h_i, where N is a natural number that defines the order of the filter. These coefficients dictate the weight of every sample included in the order of the filter. Thus, the convolution of the FIR filters is as follows:

$$y[n] = \sum_{i=0}^{N} h_i \cdot g[n-i] \tag{1.4}$$

The choice of the order of the filter must be made carefully, taking into account the number of samples of the entire digitised signal. One the one hand, in case the number of samples is close to the order of the filter, the output will be reduced in samples, having N-n samples, and the information contained in the signal might be lost. On the other hand, if the order is smaller than it should be, the output might not fulfil the requirements. Another important filter parameter is its width, that influences amplitude and delay of the output. Moreover, the choice of the values of the coefficient and their sign, defines different filter types and behaviours. For instance, two filters whose absolute values of the coefficients are the same, but their sing are the opposite, may implement either an integrative or derivative effect. In the following, some of such FIR filters are going to be introduced.

Moving Average Filter The moving average filter is one of the most simple FIR filters. It operates by averaging a specific number of samples (bins), related to the order of the filter, of the digitised signal.

$$y[n] = \frac{1}{L} \sum_{i=0}^{L-1} g[n+i] \tag{1.5}$$

Seeing Eq. 1.5, the moving average filter is a convolution of the digitised signal with a rectangular pulse having an area of one.

It may be implemented by two options:

- The filter considers a number of samples L forward to calculate the filtered signal, reducing so by L the final number of samples.
- The filter considers for the i_{th} sample the same number of samples backwards and forward, that implies an odd number of coefficients, this is commonly called symmetric moving average filter, reducing or not the number of final samples.

Triangular smooth: tends to Gaussian function. Triangular or Bartlett FIR filter are commonly applied as a smooth of signals or spectra that present high frequency noise (see Fig. 1.10). The most commonly used triangular filter are the 3^{rd}, 5^{th} and 7^{th} order, which implies a set of 3, 5 and 7 coefficients respectively, they are calculated according the Eq.(1.6) where, in order to assure a unit-gain smoothing the sum of the coefficients must be equals one.

$$\begin{array}{l} \frac{n+1}{(\frac{N-1}{2}+1)^2} \; if \; n \in \left[0, \frac{N}{2}\right] \\ \frac{N-n}{(\frac{N-1}{2}+1)^2} \; if \; n \in \left(\frac{N}{2}, N-1\right] \end{array} \tag{1.6}$$

A remarkable feature of these filters is that recursive application, twice or more, results in a higher order smooth tending to a Gaussian filter kernel as it can be seen in Fig. 1.9

Trapezoidal filter This filter is called trapezoidal due to the shape of the resulting output signal when it is applied to a step function, however both the low and high constant values are separated not by an abrupt step but by a steeped slope. The filter is formed by two moving average filters separated by a time gap, G, (see Eq. 1.7) usually shorter than the rise time of the signal to be filtered.

$$y[n] = \frac{1}{L}\left(\sum_{i=0}^{L-1} g[L+G+n+i] - \sum_{i=0}^{L-1} g[n+i]\right) \tag{1.7}$$

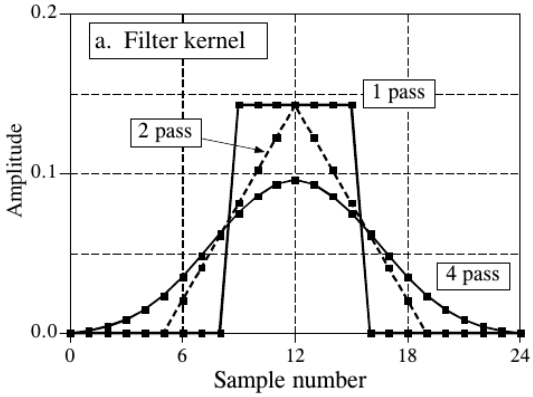

Figure 1.9.: Filter kernel when a 7^{th} order filter is passed over the digital signal once, twice and four times. Note trends to a Gaussian kernel [2].

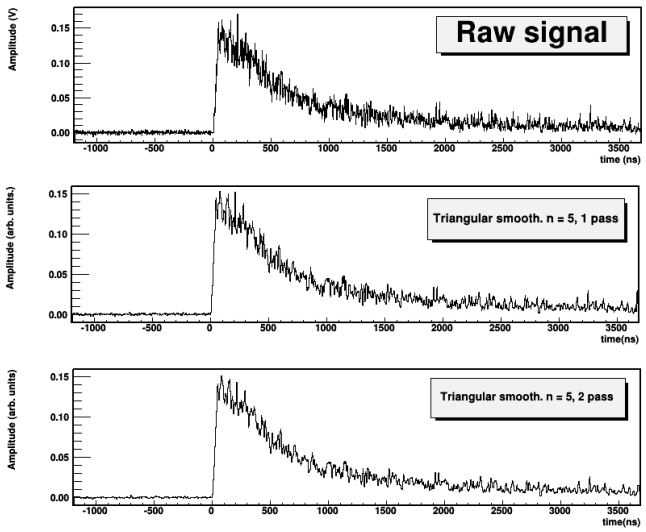

Figure 1.10.: Signal smoothed by a 5^{th} order triangular filter. Raw signal is shown is the first canvas. 1 pass filter in second canvas. 2 pass filtered in third canvas. Note the smooth of the shape as the number of passes increases.

Hann filter The Hann (or Hanning) filter has a sinusoidal shape, a good frequency resolution and can be used in most cases because of its good continuity properties that reduces the spectra leakage. The Hann filter may cause a distortion of the initial signal and therefore some corrections should be done to obtained an accurate result [28, 29].

The coefficiencies of a Hann filter

$$f(t) = \frac{1}{2} + \frac{1}{2} cos\left(\frac{2\pi n}{N-1}\right), \quad 0 \leq n \leq N \tag{1.8}$$

1.3. Conclusions on the hardware and software solutions proposed

The fast signals produced by fast scintillator detectors must be handle taking into account the problems related to its digital signal processing by the acquisition system used. For high L.Y. crystals, the photodetector output must be adapted to avoid saturation problems. Solutions have been proposed by means of the modification of the original VD in order to adapt the high amount of light produced by $CeBr_3$ crystal. The supply voltage to the dynode stages of the PMT were modified by simply adding a few components in parallel to the original ones. To obtain an accurate energy resolution and an appropriate signal conditioning two electronic circuit, one for $CeBr_3$-PMT and one for CsI(Na)-PMT, have been designed and developed. To avoid saturation problems in fADC systems when signals overcome the input signal amplitude accepted by the system, an ad-hoc attenuator were designed and tested. The simulation, measurements and results obtained indicate that the solutions proposed solved the problems found when dealing with fast scintillation crystals. Good linearity response of the detector in terms of energy resolution, calibration and non-saturation were obtained after having adapted appropriately the signals to the requirements of the acquisition systems.

USC
UNIVERSIDADE
DE SANTIAGO
DE COMPOSTELA

2. Scintillator detectors

Scintillator detectors are based on the property of some kind of plastics and crystals of producing and transmitting light when energetic charged particles slow down by ionising or exciting its electronic states. It is worth to recall that energetic enough photons (X- or γ-rays) can also produce free electrons, being in this way detected inside the scintillator volume. The amount of subsequent scintillation-photons depends so on the total energy deposited by the incident radiation, being the dynamics of the secondary processes depending also on the radiation's kind, and so, leading to different shapes of the scintillation pulse. A deep analysis of these pulse parameters will give the access to valuable information about the original physical processes.

To a better understanding of the results of the measurements performed in Chapter 3 and Chapter 4 is needed to bear in mind the basics principles of the radiation interaction in matter and of the scintillation processes. For a deeper comprehension of the detectors used in this work, a realistic Monte Carlo simulation of the deposited energy by both electrons and photons is also included in this Chapter.

2.1. Interaction of radiation with matter

The energy loss due to collisions with electrons by a charged particle in a given material, also called stopping power, was firstly calculated classically by Bohr [30] and the Bethe's theory included then corrections for quantum effects [31]. This theoretical formula, depending on Z, the electron density of the stopping material and a parameter, I (called "mean excitation potential"), was successful but showed deviations from the experimental data, at energies below around 200 keV. Bloch [32] introduced corrections, leading to the so called Bethe-Bloch formula, even though that further

corrections have been introduced later (see Appendix E).

2.1.1. Energy loss by heavy charged particles

Heavy charged-particles loss their energy mainly by the Coulomb interaction with the bound electrons of atoms of the material. In such interactions, the atoms can be either excited or ionised, depending on the energy of the charged particle. In the region of interest of this work, the ionisation process is dominant, as the energy of the incident particle is much larger than the bound energy of the atomic electrons.

The Bethe-Bloch formula describes well for $0.1 \leq \beta\gamma \leq 1000$ the mean energy loss by a charged particles in intermediate Z materials with an accuracy of a few percent. In Fig. 2.1, the mass stopping power for positive muon, μ^+, in Cu is plotted as a function of $\beta\gamma = p/Mc$. Below the lower limit, $\beta\gamma < 0.1$, the velocity of the particle is comparable to the atomic electron "velocities", and above the upper limit, the radiative effects become relevant. Note that particles with $\beta\gamma \sim 3$, the minimum value of the stopping power formula, are called "minimum-ionising particles" or by its acronym, mip's. In practical cases, most relativistic particles (e.g., cosmic-ray muons) have mean energy-loss rates close to the minimum [3].

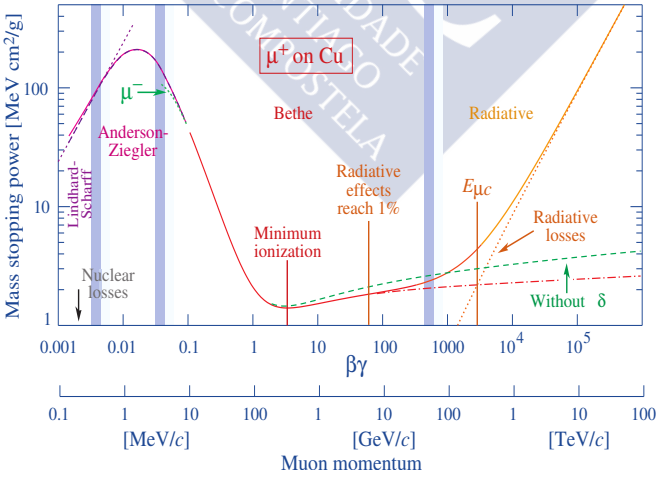

Figure 2.1.: Mass stopping power [3].

2.1.2. Energy loss by electrons

The two main processes observed when electrons (or positrons) lose their energy interacting with matter are: collisions with other electrons in the material and, on the other hand, Bremsstrahlung. It is important to understand that the electrons tracks become straggly, as their mass is small, and so the corresponding Bethe-Bloch formulas are given for the linear mean path, instead of for its actual straggled one. Therefore:

$$\left(\frac{dE}{dx}\right)_{tot} = \left(\frac{dE}{dx}\right)_{coll} + \left(\frac{dE}{dx}\right)_{rad} \tag{2.1}$$

The energy lost by electronic collision is roughly given by the Bethe-Bloch formula in Eq. E.3, however, it should be modified because two reasons: the small mass of electrons (which means that can be notably scattered in the matter on the contrary of heavier charged particles) and the fact of dealing with collisions between indistinguishable particles. Taking into account these two reasons, the linear Bethe-Bloch formula leads to:

$$\left(\frac{dE}{dx}\right)_{coll} = -K\frac{Z}{A}\frac{1}{\beta^2}\left[ln\frac{m_e\beta^2c^2\gamma^2T}{2I^2} + F(\gamma)\right] \tag{2.2}$$

where T is the kinetic energy of the electron and the function F is a correction factor different for electron or positrons.

The Bremsstrahlung energy-loss mechanism is created by the Coulomb field of the nuclei, resulting in the emission of braking-radiation. The linear specific loss through this radiative process is

$$\left(\frac{dE}{dx}\right)_{rad} = -\frac{NEZ(Z+1)e^2\alpha}{m_0^2c^4}\left(4ln\frac{2E}{m_0c^2} - \frac{4}{3}\right) \tag{2.3}$$

This process becomes relevant at energies above a few ten's of MeV where its contribution is greater than the collision process [33].

Since the energy loss by braking-radiation depends strongly on the absorbing material, an important parameter is defined: the critical energy, E_c, where the probability of the radiation loss equals the probability of

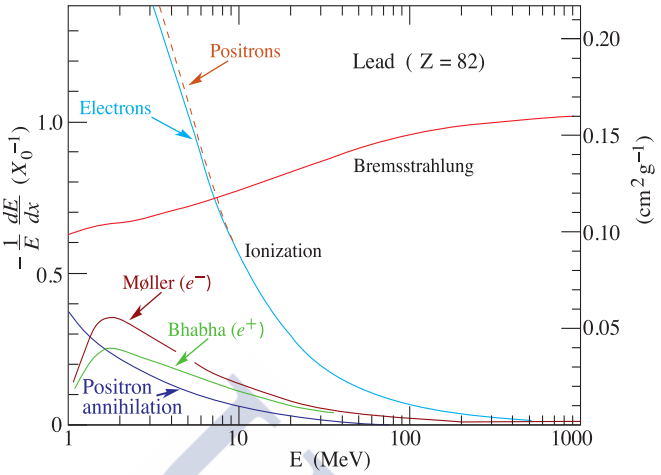

Figure 2.2.: Fractional energy loss per radiation length in lead as a function of the electron or positron energy [3].

collision loss , defined by Eqs. 2.2 and 2.3. Fig.2.2 shows the contributions of both components for lead: the critical energy is around 7 MeV. and so former becomes dominant at lower energies and the latter at higher energies.

2.1.3. Energy deposited by photons

When a photon interacts with matter, the processes involved are dependent on the energy of the incident photon and on the atomic number (Z) of the material. The main interaction of X-rays and γ-rays with matter is basically due to the three processes that will be shortly described here (for a more detailed explanation, see, for instance, Refs. [33, 19, 3]):

- The photoelectric effect.
- The Compton scattering (including Rayleigh scattering).
- The pair production.

Photoelectric effect This effect is the more likely for photons of low energies and consists on the total energy transfer from the photon to an

atomic electron, that is then ejected from the shell of the absorbing atom, and so the energy transferred to the outgoing electron is:

$$E_e = h\nu - \phi \tag{2.4}$$

where E_e is the energy of the ejected electron, hν is the energy of the incident photon and ϕ is the binding energy of the electron. It is worth bearing in mind that the ejected electron can have energy enough to produce further excitations or ionisations, in a chained way.

Compton scattering The Compton scattering process is dominant at intermediate energies. The incident photon interacts elastically with an electron and the total energy and momenta are conserved after deflecting an angle θ. The energy of the deflected photon is dependent on such angle,

$$h\nu' = \frac{h\nu}{1 + \frac{h\nu}{m_0 c^2}(1 - \cos\theta)} \tag{2.5}$$

The highest energy that can be deposited, corresponding to full backscatter, is called the Compton edge. For low scattering angles, the energy transferred approaches to zero, meaning that the gamma is not detected. The outgoing electron can go through secondary interactions, and the deflected photon can, either escape or undergo a new photoelectric or Compton interaction.

Pair Production (PP) The pair production contribution starts when γ-ray energies are larger that the sum of the rest masses of the lightest leptons (e^- and e^+), being this energy threshold $\bar{1}.022$ MeV. Such process involves the presence of a nucleus in order to conserve momentum and so the angles of the created leptons partly depend on the energy of the initial γ-ray. Once again, it is worth mentioning that the lepton pair will produce further interactions in its track, being remarkable the case of the positron, that will ends by anhilitation with one electron of the medium, creating so two back-to-back photons of 511 keV that can newly interact at random.

In Fig. 2.3 is shown the total interaction cross section for two different materials as a function of the energy of the incident photon . The figures

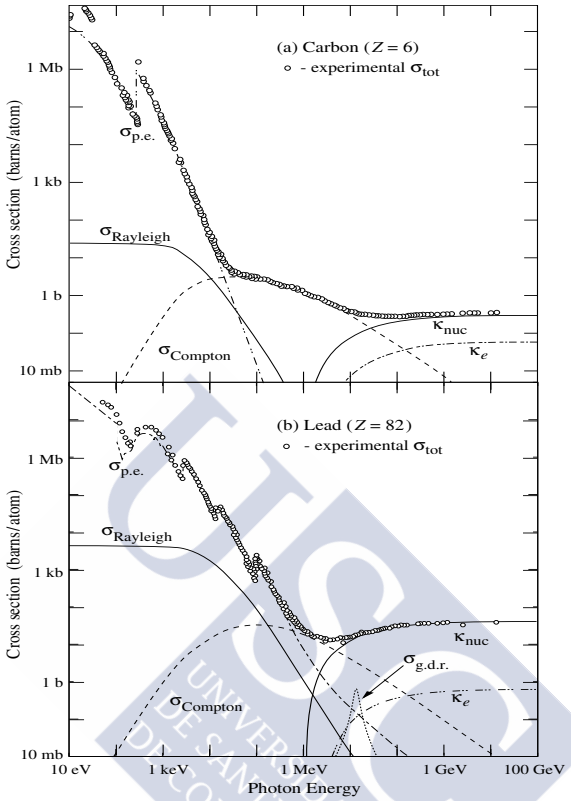

Figure 2.3.: Photon total cross sections as a function of incident photon energy in carbon and lead [3]:
$\sigma_{p.e.}$ = Atomic photoelectric effect
$\sigma_{Rayleigh}$ = Rayleigh (coherent) scattering-atom neither ionised or excited
$\sigma_{Compton}$ = Incoherent scattering (Compton scattering off an electron)
κ_{nuc} = Pair production, nuclear field
κ_e = Pair production, electron field
$\sigma_{g.d.r.}$ = Photonuclear interactions, most notably the Giant Dipole Resonance. In these interactions, the target nucleus is broken up.
Original figures through the courtesy of John H. Hubbell (NIST).

show the difference on the contribution of such processes being remarkable the higher contribution of the pair production in the lead case, because of its higher Z.

2.2. Scintillation detectors

A generic scintillation detector is made of a scintillator optically coupled to a photodetector, and can be simply seen as a transducer of the ionisation radiation or charged particle crossing its active volume, into an electronic pulse able to be handled by the corresponding front end electronics.

The scintillation mechanism

The energy deposited by the impinging ionising particle or photon will be followed by the emission of photons in the visible or near the visible energy range. This effect requires a further explanation based on the use of the energy-levels model of a crystal.

An inorganic scintillator crystal has a valence band, where all the energy levels are occupied by electrons and a conduction band that are ideally empty and separated a distance in energy called bandgap. When ionisation radiation hits the material, it creates a number of electron-holes pairs proportional to their incident energy. In Fig. 2.4, where a simplified process of scintillation is sketched, one can see the creation of an electron-hole pair by the interaction of a photon with an electron that occupied a energy level of the valence band. The electron is promoted to the conduction band and then captured by the highest energy levels of the dopant material and, correspondingly, the hole is captured by the lowest levels. The recombination of both in the luminescence centre results in the emission of a photon. See Refs. [18, 34] for deeper information about the scintillation process.

Most of inorganic scintillator crystals are impurity-activated, what means that the final light produced in the scintillation process is due to the presence of a small concentration of specific impurities (dopants), here called luminescence centres. In non-doped crystals, the scintillation process can

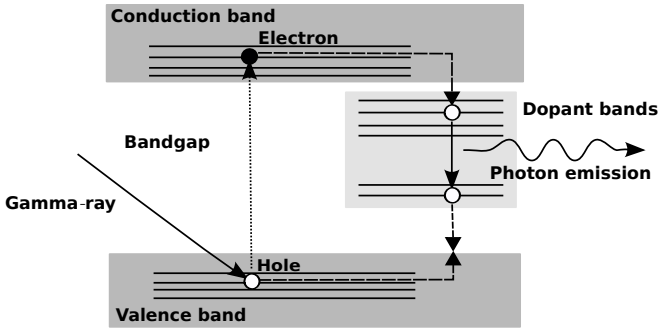

Figure 2.4.: Schematic representation of the electron structure in a scintillation material with a dopant, that play a role as luminescence centre. The scintillation process is also shown. Other processes involved are neglected for the sake of simplicity.

still be present due to the fact of a stoichiometric excess of one of the constituents of the crystal occupying interstitial positions in the crystal lattice and so working as a luminescence centres. Such materials are called self-activated. The presence of such luminescence centres creates additional and localised energy levels, narrower than the energy bandgap of the crystals, that bandgap must be larger than around 3 eV, the typical energy of visible and UV photons, in order to the material be transparent to the visible light.

The electron-hole pair creation needs a minimum energy equals to the band-gap energy E_g. The number of pairs created by an incident γ is given by

$$N_{e-h} = \frac{E_\gamma}{b\ E_g} \tag{2.6}$$

where the parameter b has a value that depends on the nature of the host matrix. For the crystals studied in this work, $b \approx 2$. Following this model, the maximum number of photons created by an incident photon or charged particle should not exceed the number of pairs; as from Eq. 2.6, i.e., this maximum is one tenth the energy of the impinging photon, roughly speaking. This value is typically provided in units of photons/MeV, being known as intrinsic light yield [25], because the actual L.Y., (what it is in

fact achieved) is lower due to self-absortion and the energy lost in different mechanisms, as the creation of phonons, among others.

Taking into account the timing of these processes, the time profile of the light glint should have a very fast leading edge (the time spent in the excitation of the luminiscence centres), typically followed by a simple exponential decay (corresponding with the mean life. τ, of the excited states) given by:

$$L(t) = L_0 e^{-t/\tau} \tag{2.7}$$

This simple model is a rough approximation, appropriate for many scintillator materials, however, more contributions to the exponential decay are appreciated, including long lived luminiscence. Some crystals can have two or more kind of luminiscence centres, with different time constants, [33] leading to a more realistic timing behaviour given by:

$$L(t) = \sum_{i=1}^{n} \frac{A_i}{\tau_i} e^{-t/\tau_i} \tag{2.8}$$

where τ_i is the decay constant for each component and A_i is the proportional weight of each one of the n components [35].

For a scintillation detector (composed of the scintillator and the optodevice coupled to them), the capability of the scintillation light to quickly be collected by the optodevice is an important aspect for the preservation of the light yield and, therefore, of the energy resolution. As the light produced at the luminiscence centres is isotropic, several reflections in the wrapping reflector are expected. Moreover, real crystals are always characterized by the presence of some impurities that may also absorb photons. As a consequence, the size, shape and finishing of the scintillator crystals determine its properties, as the longer the distance a photon has to travel inside them, the higher is the probability to be lost. In Ref [7] is shown how, for very fast crystals, as $CeBr_3$ and $LaBr_3$:Ce, the size affects not only the energy resolution but also the apparent scintillation decay time.

Photodetectors

The light flashes produced within the scintillator crystals require fast photodetectors with the highest quantum efficiency (Q.E.), in order to detect the reduced number of visible photons produced during the scintillation process. Moreover, the scintillator L.Y. is distributed along a certain wavelength spectrum, matching more or less the spectral sensitivity of the photodetector, that has a Q.E. depending also on the wavelength. The convolution of the L.Y. function with the Q.E. one, will give the overall spectral efficiency of the detector. Furthermore, the appropriated optical coupling plays a very important role, as well as the matching between the size of the exit window of the crystal and the active area of the photodetector.

2.3. Scintillator detectors used in this work.

In the last decades more and more new types of inorganic scintillator crystals have been developed, enhancing properties of traditional scintillators, where the former reference was NaI(Tl). Used widely in both nuclear and high-energy physics, as well as for medical applications and industrial systems, the improvement of their properties such as light yield, energy resolution, detection efficiency, pulse linearity or timing resolution is a continuous challenge. When growing those crystals, where dopant materials are normally included, both the density of dislocations and the uniformity of the dopant distribution, influence the luminiscence properties of scintillators.

In this work, four halide crystals have been characterised: two scintillators based on the Ce^{3+} ion ($CeBr_3$ and CeF_3) and a CsI(Na).The main properities of these scintillator crystals can be found in Table 2.1 and their dimensions are listed in Table 2.2

It can be seen that the best balanced crystal is $CeBr_3$, having a fast decay and the highest L.Y., besides an emission peak matching well the Bialkali photocathodes sensitivity. The CeF_3 crystal has the fastest decay constant, besides the higher density and effective atomic number, with the drawback of the poorer L.Y., by a factor of ten, being so competitive only at energies well above 1 MeV. The CsI(Na) crystal is not the better but it

is the cheaper and does not behaves so bad, as will be explained along the next Chapters.

Scintillator crystal	CsI(Na)	$CeBr_3$	CeF_3
Density (g/cm^3)	4.51	5.20	6.16
Decay constant, τ (ns)	630	18-20	5,27
Emission peak, λ (nm)	420	380	300,340
L.Y. (ph/keV)	35-42	45-60	4.3
Refractive index, n	1.84	2.09	1.62
Crystal structure	Cubic	Hexagonal	Hexagonal
Efective atomic number, Z_{eff}	54	45.9	53
Hygroscopicity	Yes	Yes	No

Table 2.1.: Main characteristics of scintillator crystals: $CeBr_3$, CsI(Na) and CeF_3.

Scintillator crystal	$CeBr_3$	CsI(Na)	CeF_3_L50	CeF_3_L40
Dimensions(mm^3)	18x18x25	18x18x25	18x18x50	18x18x40
Finishing	Polished	Polished	Non-polished	Polished
Encapsulation by	Scionix	USC	USC	USC
Manufacturer	Scionix	MolTech	MolTech	MolTech

Table 2.2.: Main characteristics of the scintillator crystals used in this work

It is worth mentioning that Cerium has an ionic radius smaller than the Lanthane one (122pm vs. 130pm) and, as a consequence, $CeBr_3$ density is slightly larger than that of $LaBr_3$:Ce, (5.18 g/cm^3 vs. 5.07 g/cm^3). On the other hand, the CeBr3 effective atomic number, Z_{eff}, is larger than that of $LaBr_3$:Ce, (45.9 vs. 45.3) and so a few percent advantage in gamma detection efficiency is expected for $CeBr_3$, compared to $LaBr_3$:Ce, at energies dominated by pair-production where the interaction probability rises approximately as Z^2_{eff}.

2.3.1. Wrapping and encapsulation

In order to collect as much light produced by the ionising particles or γ-rays, the crystals are wrapped by reflective materials that have been proved

to be more efficient when they are dispersive. Both the election of wrapping materials, as well as a good tight coverage, are crucial when looking for the best efficiency in the scintillation light collection that redounds to the higher energy resolution. The most common used wrapping material is PTFE (Teflon) because of its high light reflection and its use ease; the ever most efficient material is Enhanced Specular Reflector (ESR) from 3M, [36]) whose reflectance is higher than 98% (see Ref [37] for a comparative study).

The hygroscopicity of the materials can degrade the properties of the crystals, affecting to their transparency, (the so-called *yellowing*) and worsening the transmission of the light created in the scintillation process. Therefore, an appropriated encapsulation must be made in cases of high hygroscopicity to avoid the absorption of moisture from the environment.

$CeBr_3$ $CeBr_3$ crystal is highly hygroscopic and, therefore, the encapsulation was made by the manufacturer. The crystal was surrounded by a 0.5 mm of Teflon reflector, and a quartz window ($n_{quarz} = 1.54$) was placed over the exit window of the crystal. The assembly was then encapsulated in an aluminium housing with 1.5 mm thick walls.

CsI(Na) CsI(Na) crystal is less hygroscopic than $CeBr_3$, and so, the encapsulation could be made by us in our USC laboratory. The wrapping of the crystal consisted in two foils of ESR. Black adhesive tape was wrapped around plus two 2 mm sheets of G-10, in order to tight the crystal to the walls of the aluminium housing (30mm x 30mm x 30mm). The input crystal face was sealed using an aluminium adhesive tape of 0.75 mm thickness from 3M.

CeF_3_L50 This crystal is non-hygroscopic. Similarly to CsI(Na), the CeF_3_L50 crystal wrapping consisted of two foils of ESR and black adhesive tape, plus two sheets of G-10 in an aluminium package of 25 mm x 25 mm x 50 mm.

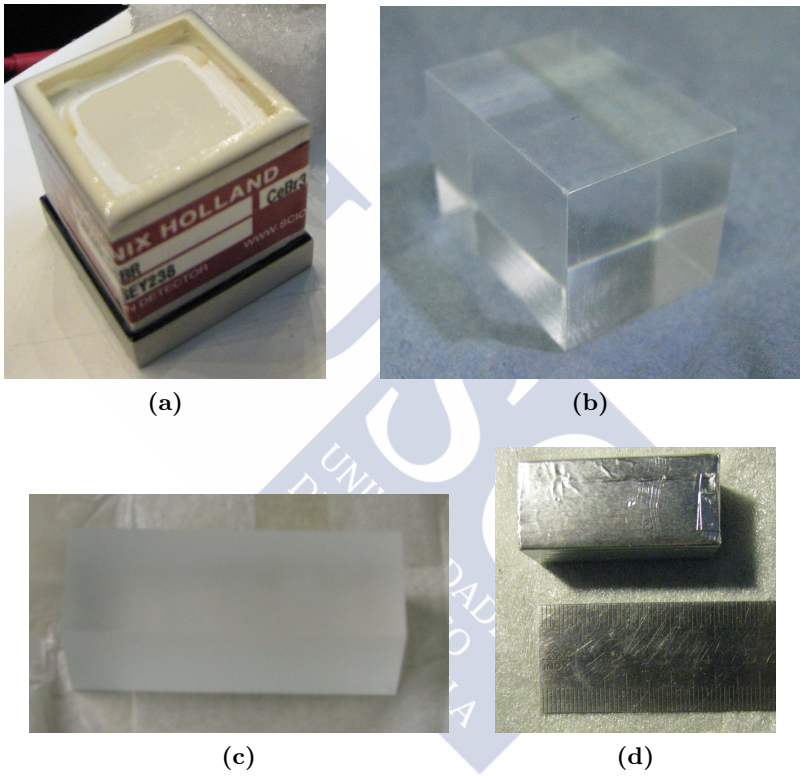

Figure 2.5.: Scintillator crystals used in this work: (a) $CeBr_3$ crystal encapsulated by Scionix. (b) CsI(Na) crystal. (c) CeF_3 crystal L = 50 mm. Note the non-polished surface. (d) CeF_3 crystal L = 40 mm wrapped by two foils of ESR from 3M reflector material.

CeF_3_L40 CeF_3_L40 was simply wrapped using two foils of ESR without aluminium housing. Depending on the sort of measurements, two wrapping configuration were performed:

- A: having an opening of 2 mm in the input surface to let the α particles interact with the crystal.
- B: a whole wrapping of two foils of ESR.

2.3.2. Photodetectors used

Photodetectors can be classified mainly in two groups: Photomultiplier tubes (PMT) and Si-based photodetectors, as PIN diode (PD), Avalanche photodiode and Silicon PMT (SiPM).

The photomultiplier tubes and PIN diode photodetectors will be briefly described in the following. For SiPMs see Ref. [38].

R7600U-200 Photomultiplier Tube The advances on PMTs in 90s decade had led to improvements in their design and development. An step forward was done by Hamamatsu at the R&D for the Super-Kamiokande experiment, boosting the technology applied to them. For instance, the noise level was reduced by interposition of insulator materials between the adjacent dynodes, preventing ions and light feeding-back to the photocathode in the electron multiplication process. The positions of the first and second dynodes were optimised for a good efficiency collection. In order to focus photoelectrons by electron-lens effect, more efficiently guiding photoelectrons from the photocathode to the first dynode, a new technology to arrange grid pattern between the photocathode and immediately in front of the first dynode was developed.

The PMT R7600U-200 manufactured by Hamamatsu, besides the properties above mentioned, has also improved the feedback prevention by using metal packages (technology developed in 1992). In addition, a novel technology for optimising the position between the first and second dynodes has been used; this technology was invented for metal channel dynodes with no grid patterns (see Fig. 2.6) [4]. As a result of this inheritance, Hamamatsu developed the smallest TO-8 metal package photomultiplier

tubes. The cubic shape of such PMT facilitates stacking the photodetectors, when a big detector requires large segmentation [39].

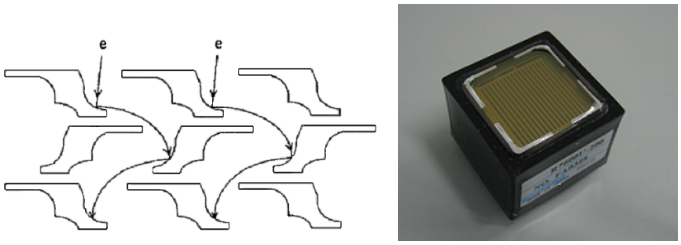

(a) **(b)**

Figure 2.6.: Cross section of metal channel dynodes[4] (a). PMT mod. R7600U-200 from Hamamatsu (b).

The PMT R7600U-200 also offers a very high photocathode quantum efficiency, 43 % at 430 nm, called "ultra bialkali" (UBA). Former photocathodes, with high sensitivity, called "superbialkali" (SBA), deliver a lower quantum efficiency of 35% at 350 nm. Fig. 2.7 shows typical spectral response curves of the UBA, SBA and BA photocathodes.

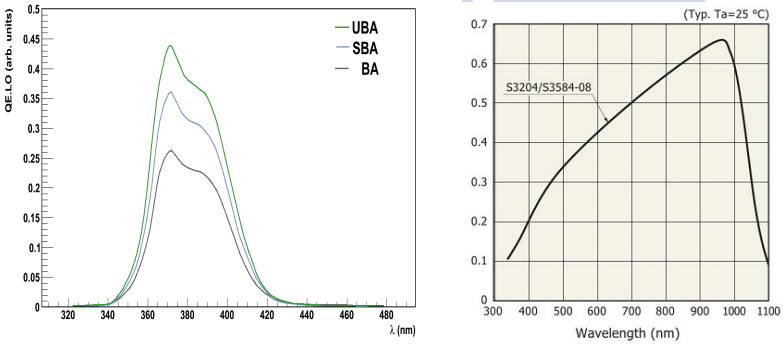

(a) **(b)**

Figure 2.7.: Q.E. of UBA, SBA and BA photocathodes for $CeBr_3$ (a). Spectral response of PIN diode model S32004-08. Courtesy of Hamamatsu Photonics K.K. (b).

Just to see the evolution of the photocathode efficiency, let us mention

that the Q.E. of the first PMT, built in 1930, was less than 1 % at peak wavelength and then, the research and development of the photocathode materials got improved the Q.E. up to 25% in the mid-1960s. These increments of the Q.E. becomes very relevant for those applications and experiments where the number of photons emitted by the photon source (scintillator crystal) is scarce [40].

PIN Diode S3204-08 The PIN diode was one of the first developed silicon, Si, photodetectors. Their inner structure roughly consists on the junction of three silicon layers (in order): a Si layer heavily doped with donors (n+ region), a Si intrisic piece and a Si layer heavily doped with acceptors (p+ region). This configuration is reverse-biased, forming a depleted region that contains the whole intrinsic piece and extending to both the p+ and n+ regions, forming a wide light detection area (see Fig. 2.8). PIN diodes are usually covered by a thin layer of highly transparent resin for an optimal coupling as well as preventing a possible mechanical damage of the first doped silicon layer. Solid-state devices are advantageous over PMTs when operating in the presence of a magnetic field, that disturbes the swarm of electrons created in the PMTs stages and do not in the PIN diode case [5]. As a drawback the Q.E. of the PIN diode decreases at the wavelengths of our interest, being so its overall efficiency much lower that in the PMT R7600U-200. The radiant response for PIN diode S3204-08 is shown in Fig. 2.7 (b).

The PIN diode, model S3204-08 from Hamamatsu, has a large active area with a compact design, as can be seen in Fig. 2.8; and its power supply voltage for a gain of x10 is around 70 V, as specified in Table 2.3.

	PMT R7600U-200	PIN diode
Bias Voltage(V)	-800	70
Gain	10^7	10

Table 2.3.: Photodetectors biasing.

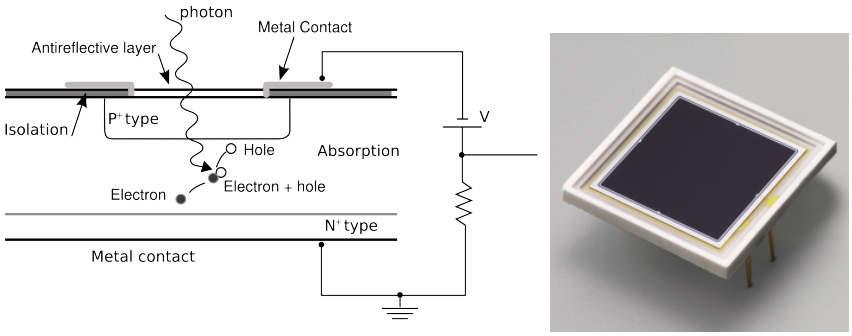

Figure 2.8.: Structure of a PIN diode, (a) [5]. PIN Diode S3204-08 from Hamamatsu (b). Courtesy of Hamamatsu Photonics K. K. [6]

2.3.3. Coupling scintillators to photodetectors

The four crystals were coupled to two different photodetectors attending to their output window and their emission spectra. Both the L.Y. of an scintillator crystal and the Q.E. of the photodetectors, are light wavelength dependent. The result of the convolution of both curves, called Photoelectron Yield, P.Y., is calculated and plotted in Fig. 2.9 for the three crystals, $CeBr_3$, CeF_3 and CsI(Na) coupled to a PMT R7600U-200. Note the high P.Y. for $CeBr_3$.

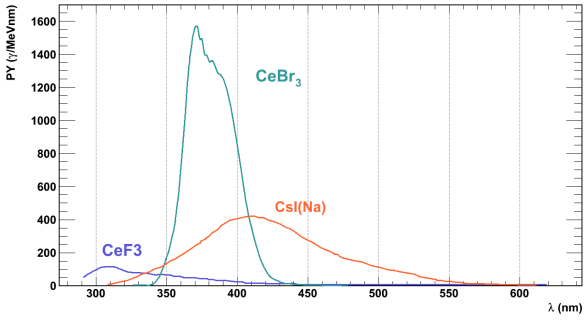

Figure 2.9.: Photon Yield of $CeBr_3$, CsI(Na) and CeF_3 [7],[8], [9]

Final assemblies

$CeBr_3$-PMT The R7600U-200 PMT and the $CeBr_3$ were coupled using two coupling materials: a Silicon Pad, mod. BC-634A, and optical grease, BC-630, both from Saint-Gobain Crystals [41]. The results obtained with the optical grease were comparable to those obtained when coupling with Silicon Pad. The set assembly will be called $CeBr_3$-PMT onwards.

CsI(Na)-PMT An aluminium piece was machined in order to a proper assembly between the crystal encapsulated and the surface of the R7600U-200 PMT. This piece was glued to the plastic coating of the PMT. A ESR mask surrounding the borosilicate window that is set in order to avoid light losses. The coupling is made using a bi-component adhesive Scionix RTV 681 from Scionix [42]. The set assembly will be called CsI(Na)-PMT onwards.

CeF_3_L40-PMT and CeF_3_L50-PMT Both crystals are coupled to the R7600U-200 using optical grease, BC-630 and an ESR mask as the decribed previously [41]. The sets assembly will be called CeF_3_L40-PMT and CeF_3_L50-PMT respectively onwards.

CsI(Na)-PIN The CsI(Na) crystal is glued to the PIN diode S3204-08 using Meltmount n = 1.582 adhesive [43]. The set assembly will be called CsI(Na)-PIN onwards.

2.4. Simulation work

Simulations are essential to understand the response of detectors to different kind of particles in function of its kinetic energy. Therefore, the simulations performed for two different type of crystals are described here in order to better understand the response of the scintillator crystals, for both γ-rays and electrons. Finally the results and conclusions will be presented. The features of the simulation program here used, EnsarRoot [17], are described in the Appendix F.

2.4.1. Description of the simulation

Two punctual radiation sources -one for γ-rays, one for electrons, e^-- have been simulated. The sources were placed at 1 cm from the input window of the crystals. Their emission angles are $0^o \leq \theta \leq 15^o$ and $0^o \leq \varphi \leq 360^o$. The simulation medium is vacuum. The software provides an output ROOT file with different observables. The most relevant parameters for this study are the deposited energy in the crystals for different incoming energies in order to find out the efficiency of the crystals for a certain energy of the γ-rays and the most probable value of the deposited energy in the electrons case.

This simulation work has been performed for both $CeBr_3$ and CsI(Na) scintillators, with dimensions close to the ones having the real detectors used in the rest of the Thesis work. For the sake of simplicity, CsI(Na), the material simulated was CsI. The aim of the simulation performed in this work is to determine the energy deposited in each crystal and, therefore, the dopant, (Na in this particular case) does not alter significantly the characteristics of the CsI. The characteristics not affected by the dopant are the density of the material and its radiation length. See Table 10.9 in Ref. [44]. Nevertheless, the optical characteristics, such as wavelength emission or refractive index were significantly modified.

Three different configurations were defined for each crystal as follows:

a) Bare crystals. Dimensions (close to the real ones): 18x18x25 mm^3.

b) Crystals in contact with an Al foil. 1.5 mm thick and an area of 18x18 mm^2.

c) The same as in the configuration c) but with a foil thickness of 5 mm.

The simulation results leads to the spectrum of deposited energy in the crystal as well as to an estimation of the counting efficiency. In order to get more realistic results an experimental smearing is included for each crystal, corresponding to the global detector resolution at 1 MeV..

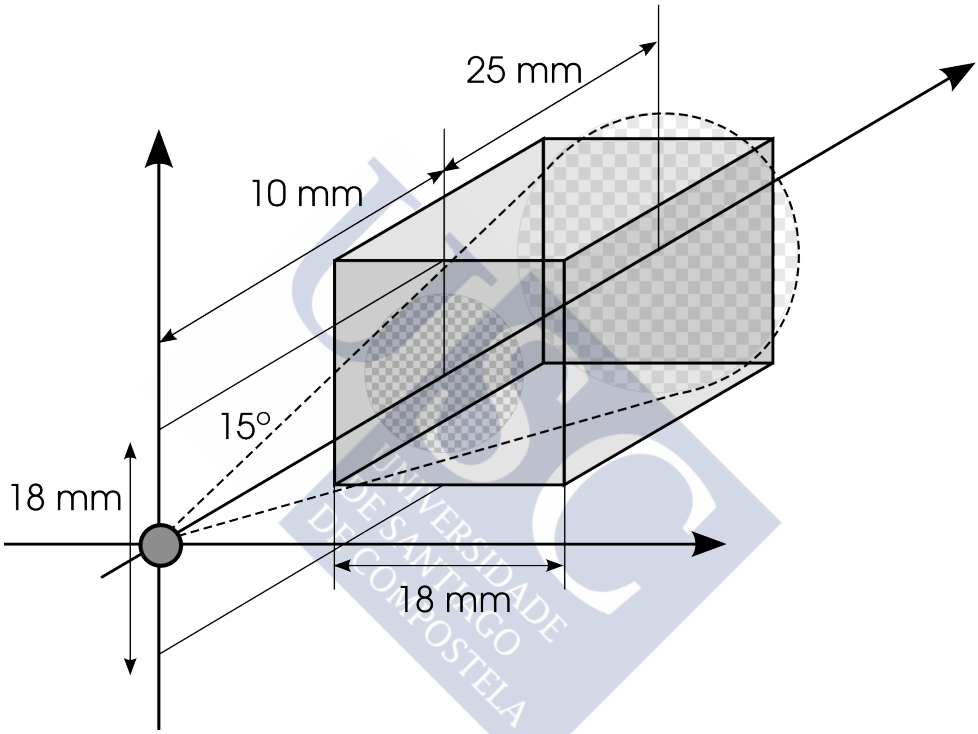

Figure 2.10.: Schematic set-up for simulations. The simulated source is sketched by the circle placed a t the origin of coordinates. The parallelepiped crystal is shown as well in the figure. The dash-line represents the solid angle from the source to the end of the crystal.

2.4.2. Photon simulations

The photon simulation consists on the emission of monochromatic γ-rays in a wide range of initial energies: from a few MeV to GeV. The simulation output provides a ROOT Tree that contains a set of observables, stored in a event-by-event basis. The observable of interest for the γ-ray simulation is the deposited energy by every incident γ-ray recovered from the Tree, using a script runs in ROOT. The same range of incident energies is simulated for the three configurations, stated above, of both crystals. The simulations were performed over 15000 events (15000 incident γ-rays).

A study of the detection efficiency of the $CeBr_3$ and CsI was made. The detection efficiency relates the ratio of number of events registered by the crystal having an amplitude above a threshold well above a tipical SNR >1, over the events impinging on the crystal. In Fig. 2.11, (a) and (b), the respective values of such efficiencies for each incident energy and each configuration are shown. It is observed that the detection efficiencies rising up to 60% from a few MeV to GeV, where the efficiency saturates, because (see the spectra in Appendix G) the most probably deposited energy in these crystals never exceeds 20 MeV.

A similar behaviour is observed in the case of the CsI crystal, although the efficiency values are slightly below than the ones in the $CeBr_3$ for low energies and slightly above at high energies.

It is worth pointing out that at low energies, the photopeak efficiency, (the efficiency of the crystal when the the full-energy of the incident particle is registered by the crystal), decreases as the incident energy increases, (see Fig. 2.14) as it was observed in γ-rays radioactive sources spectra experimentally acquired in Chapter 3. It is clear that the size of the crystal plays an important role when dealing with the photopeak efficiency: larger crystals have higher photopeak efficiency because less energy escapes from the crystal. In this particular case, the crystals can be classified as small detectors in agreement with the mean free path of the γ-rays in the material [33]. From Fig. 2.11 it becomes clear how for 2 MeV the photopeak and Compton energies are the most probable, whereas at 5-10 MeV the escaping peaks becomes very relevant.

As a conclusion, both crystals behaves very similarly and the effect of

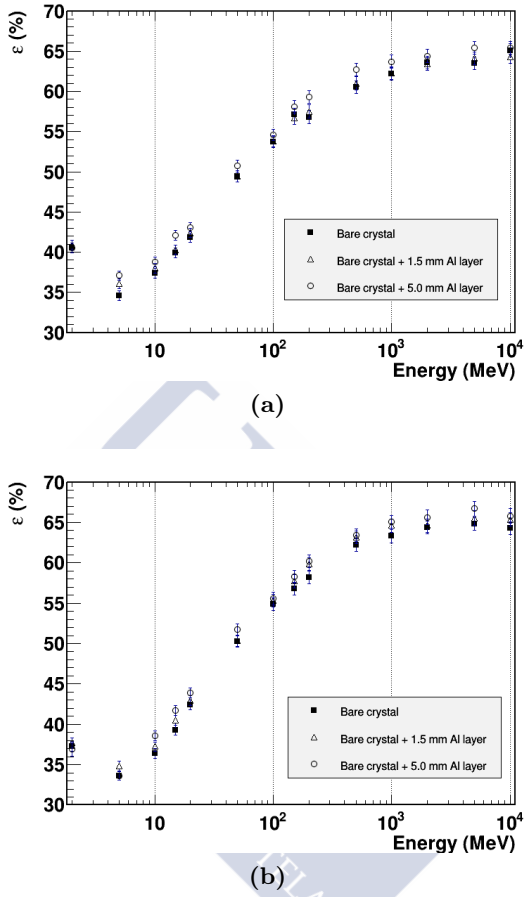

Figure 2.11.: Detection efficiency of $CeBr_3$ (left) and CsI (right). The three simulation configurations are shown in both cases.

having aluminium sheets (the three configurations here simulated) is not so relevant, showing similar counting efficiencies all along the energy range of interest.

2.4.3. Electron simulations

A similar simulation was performed for electrons. The crystals size and the simulation configuratios were as in the previous Subsection. Monochromatic electron sources were used as event generator and he range of incident energies spans from 2 MeV to 10 GeV and isn Fig 2.15 are the simulated energy spectra of electrons in the $CeBr_3$ crystal. It can be seen the difference with respect to those created by γ-rays as in this case the energy deposition mechanism is simpler. Nevertheless, above 5 MeV the Bremsstrahlung effect opens the way to photons escaping from the active volume. Once again, for the higher energies is worth distinguishing between the most probable energy deposition in these so small crystals is around 20 MeV. The most probable value of the deposited energy in the crystal, onwards **mode**, and the mean value of the deposited energy, onwards **mean**. A comparison between both observables provides information about the distribution of the deposited energy for each incident energy in Fig. 2.12.

For both crystals, the mode and the mean value increase in parallel untilaround 50 MeV, getting values up to around 20 MeV where the mode rising stalls whereas the mean value continues to grow, even though its uncertainty increases dramatically. It is worth to note how the mode rise again above 1 GeV, even tough its uncertainty starts to increase too. It is notable that of the energy region where the mean and mode values begin to differ is well above the critical energy of both crystals, being 11.7 MeV in CsI and 17.5 MeV in $CeBr_3$ [45], that implies that above such region, the Bremsstrahlung emission being predominant, starts to significantly escape from the active volume.

See Fig. 2.13. In Figs. 2.12 and 2.13 is shown how at the lower energies, for the third configuration, the electrons barely deposit energy in the crystals due to the fact that the 5 mm thick aluminium foil attenuates the least energetic electrons, preventing so their detection in the crystals. In the range from 50 to 1000 MeV the mode get a plateau and from that energy on the mode is increasing again.

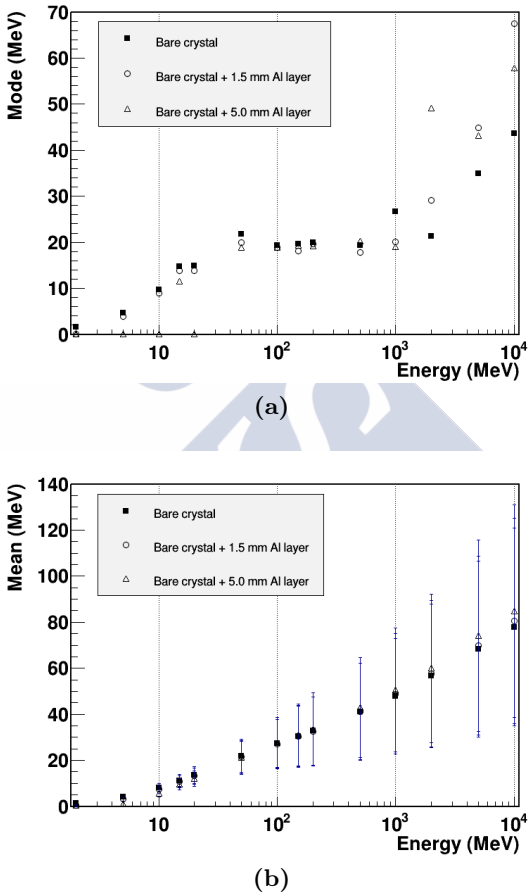

Figure 2.12.: Mode value (left) and mean value (right) for $CeBr_3$. The three simulation configurations are shown.

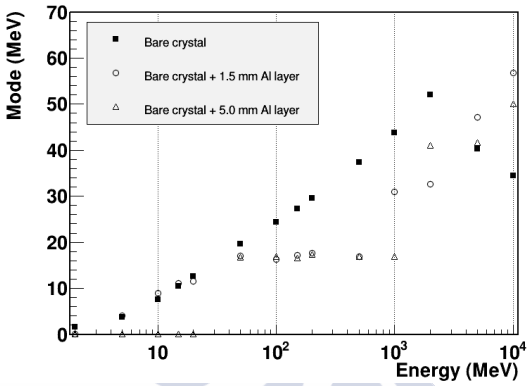

(a)

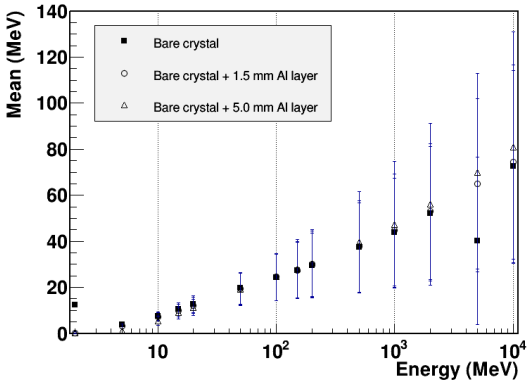

(b)

Figure 2.13.: Mode value (left) and mean value (right) for CsI. The three simulation configurations are shown.

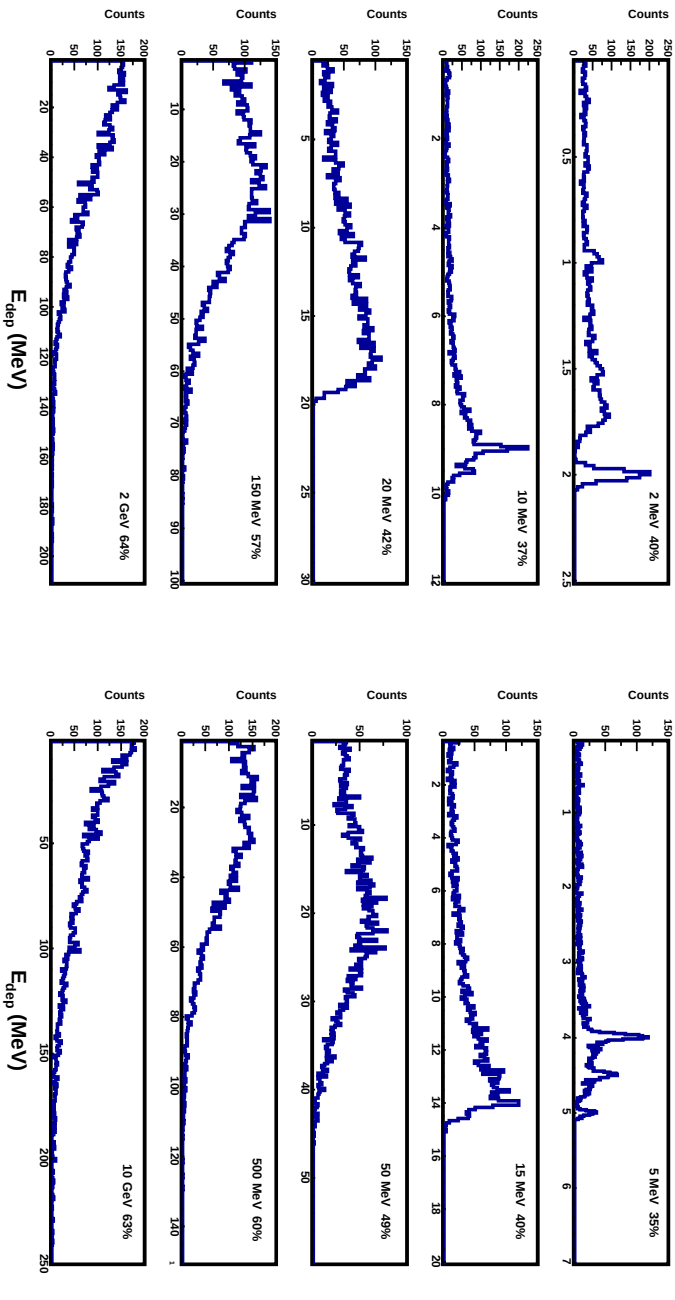

Figure 2.14.: $CeBr_3$ bare crystal. Energy deposited spectra at different initial energy for γ-rays. The counting efficiencies are shown for each energy

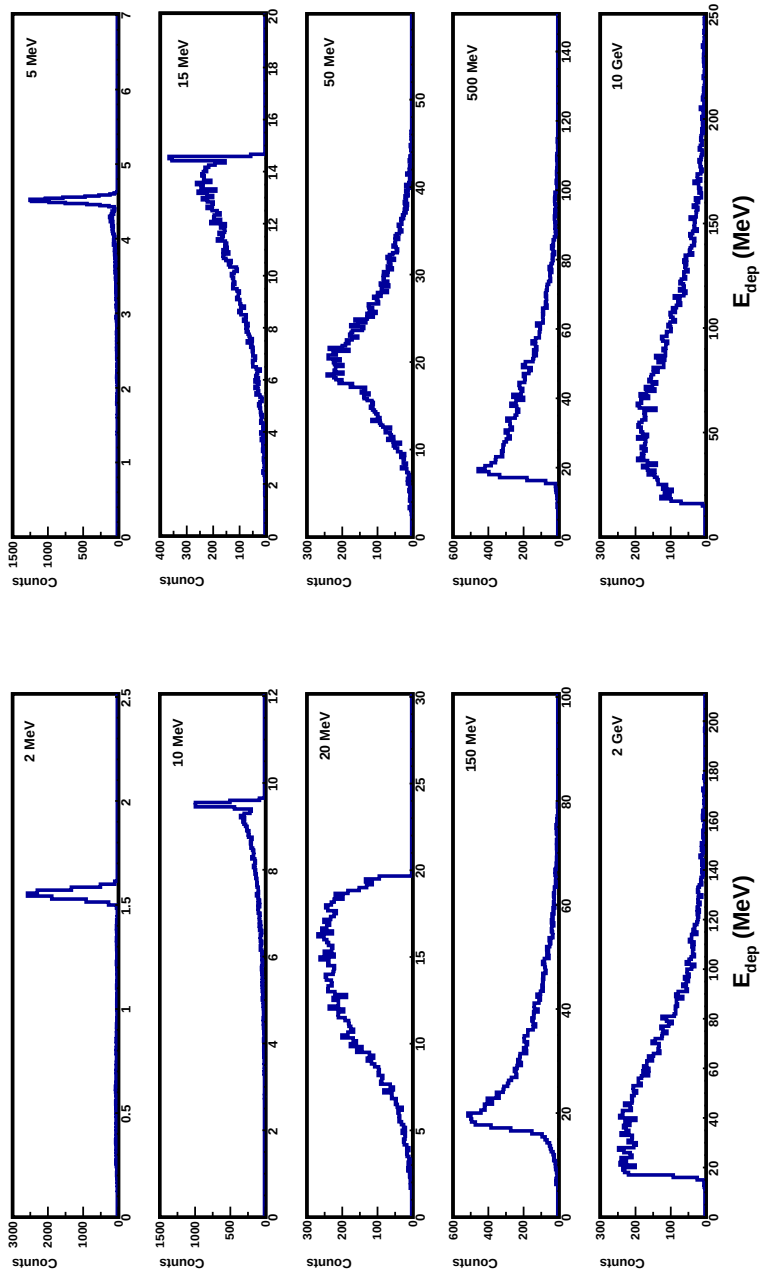

Figure 2.15.: $CeBr_3$ bare crystal. Energy deposited spectra at different initial energy for electrons.

2.5. Conclusions to the Chapter 2

After reviewing the mechanisms of creating a certain light yield in scintillation crystals and the way this light is converted to an electronic pulse by the corresponding optodevice, are presented the simulation work done to better explain the results gotten both in lab bench tests and in the CERN-n_TOF experimental facility. The simulations performed using the EnsarRoot simulation program for $CeBr_3$ and CsI crystals have the clues to interpret provided the behaviour of both crystal for γ-rays and β particles. It is worth mentioning the high detection efficiency for γ-rays, greater than 40 % in the energy range studied and increasing up to 60 % at energies larger than 100 MeV. An simulation for the deposited energy by β particles in both crystals provides accurate information about the threshold energy when radiation losses become relevant.

3. Tests result with radioactive sources and cosmic-rays

In the previous Chapter those scintillator detectors studied in this work have been introduced and the challenges of dealing with fast and high-L.Y. scintillator crystals, as well as some technical solutions to face them were discussed in Chapter 1. In this Chapter is shown how the application of such techniques permits a proper characterisation and a better performance of these fast radiation detectors. Tests with radioactive sources were performed in order to characterise the response to the deposited energy, so that the detectors linearity, energy resolution, timing resolution and efficiency will be discussed.

3.1. Detectors calibration: spectra acquisition and linearity

The radioactive sources using in the following sections in this chapter are mainly γ emitters, namely ^{152}Eu, ^{137}Cs, ^{60}Co and ^{88}Y, but also a β emitter, ^{90}Sr, an α source, ^{238}Pu, and finally, one of Am-Be, giving both γ and neutron source were used. The tests done with these radioactive source allows a study of the detectors behaviour in a range of energies from 121 to 4444 keV.

3.1.1. Energy resolution and linearity

The typical set-up to get the different spectra was described in Section 1.1.3 and the procedures there described have been used here. The low-noise high-stability HV power supply from ISEG, module NHQ 225M [46], was feeding the optodevices and the signal output was sent to a preamplifier

and shaping stage (either the *stretcher* PCBs described in the Appendix C, or the MPR-1 module from Mesytec [47] in the case of CsI(Na)-PIN), then connected to a SA, CANBERRA mod. 2022, and, finally, the amplified and shaped signals were acquired by a MultiChannel Analyser MCA-8000A from AmpTek [48], that digitises and transfers the data to a PC where the client software have been installed.

The spectra acquired from ^{88}Y and AmBe radioactive sources were performed by the $CeBr_3$-PMT and CsI(Na)-PMT detectors and both sources were placed at the EAR1 in the CERN-n_TOF facility. In this case, the set-up differed slightly from the measurements done at the USC laboratory with the chain above mentioned: the *stretcher* PCBs used were an early versions of the final designs, and the SA employed was an ORTEC mod. 570, from the shelves in the n_TOF experimental facility.

The ^{152}Eu source was used for the calibration of the $CeBr_3$-PMT, CsI(Na)-PMT and CsI(Na)-PIN detectors because it features eight peaks of relatively high intensities. Their energy (in keV) and BRs are, respectively: 121 (25.6%), 244 (7.6%), 344 (26.5%), 778 (12.9%), 964 (14.6%), 1085 (10.2%), 1111 (13.6%) and 1408 (21.0%). The resolution of the photopeaks (see in Fig.3.1) were calculated, for every scintillator detector, from the parameters given by fitting to a gaussian function plus a linear function [49] after subtracting the background radiation.

It is worth saying that the two peaks at 1.086 and 1.112 MeV are 26 keV apart from each other, what is around 2.36% of the peaks' energy and, therefore, it can not be resolved. Nevertheless, its BRs are quite similar and so, in this study, the apparent peak shape has been unfolded in two gaussians, getting in this way the resolution attainable at its middle point, 1.1 MeV.

3.1.1.1. $CeBr_3$-PMT

In Fig. 3.2 (a), the channel-energy linear calibration is shown when used the *stretcher* PCBs originally designed for this work. In Fig. (b), the energy resolution obtained for the photopeaks of ^{152}Eu were fitted to

$$R(E) = \frac{p_0}{E^{p_1}} \tag{3.1}$$

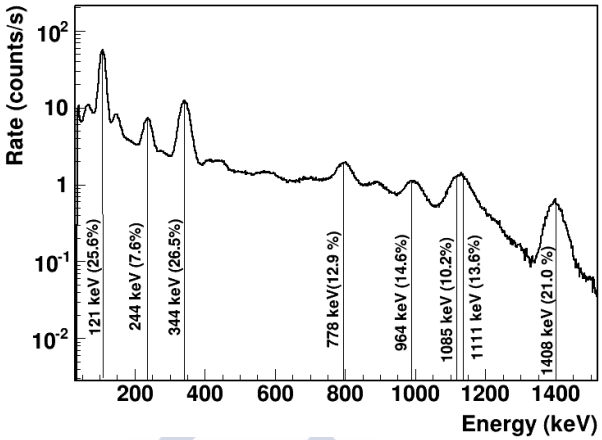

Figure 3.1.: The ^{152}Eu spectrum (in this case with the $CeBr_3$-PMT detector).

The energy resolutions given here are the result of the intrinsic resolution of the scintillating process in the detector, plus the gaussian dispersion of the L.Y., plus the dispersion of the multiplication by the opto-device, plus the contribution from the electronic chain. In order to quantify this electronic chain contribution, the signal output from the $CeBr_3$-PMT was simulated, by an artificial pulse generator connected to the rest of the spectroscopic chain, including the stretcher and the SA. The output from a signal generator was shaped, by differentiation of its squared pulse by means of a RC circuit. The amplitude of this signal was arranged to be similar to the signal produced by a γ-ray of 662 keV; The result seen in Fig. 3.3 (b), showing a sigma = 4 (FWHM = 9.4), is leading to a R_{pulser} = 1.4 %. This dispersion includes the stability of the pulse amplitude from the signal generator, that was calculated by means of a 5 GS/s digital oscilloscope to have a σ/amplitude = 0.5 %. We concluded, therefore, that the resolution factor introduced by the electronic chain was R_{elec} = 1.3 % $\pm$ 0.2 % and the overall resolution was then unfolded by means of

$$R^2_{detector} = R^2_{total} - R^2_{elec} \tag{3.2}$$

A spectrum of ^{88}Y+AmBe was measured. Fig 3.4 shows the efficiency

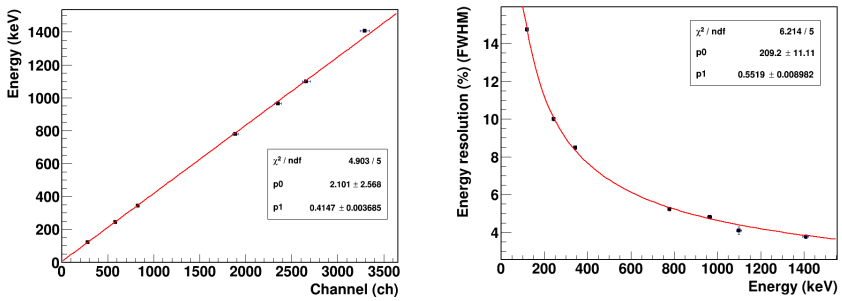

(a) **(b)**

Figure 3.2.: Calibration energy (left) and energy resolution (right) for $CeBr_3$-PMT

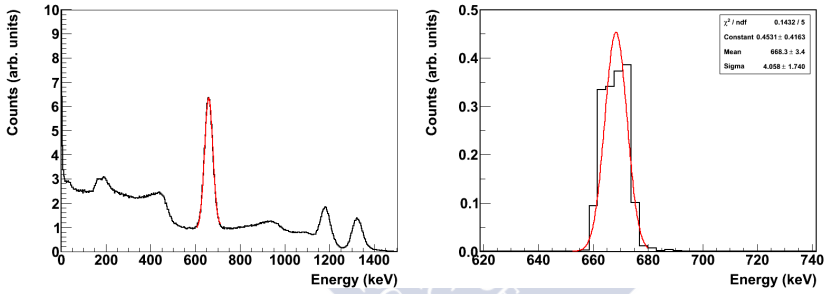

(a) **(b)**

Figure 3.3.: ^{137}Cs+^{60}Co spectra using $CeBr_3$-PMT detector (a). Electronic contribution resolution (b).

of the detector to detect γ-rays of 4444 keV. The efficiency for such as high energies is low because of the small size of the crystals. Indeed, as it was shown by the simulations performed in this work (see Section 2.4 in the previous Chapter): this low photopeak efficiency is due to the high probability of secondary photons escaping by the crystal boundaries (see Section 2.1).

In some published works, Refs. [50] [7], on crystals of $CeBr_3$, inner background have been measured because the presence of contaminants

in the material that could disturb the measurement of γ-rays spectra. The background acquired in this work along 24 hours, see Fig. 3.5, does not show the presence of contaminants in the $CeBr_3$ scintillator crystal provided by Scionix.

Test with a β emitter A ^{90}Sr source was used to find out the ability of the $CeBr_3$-PMT to detect β particles. The spectra is shown in Fig. 3.6. Two contribution of the continuous spectrum can be distinguished, in spite of its aluminium housing: one is coming from the emission of the $\beta-$ disintegration of ^{90}Sr whose endpoint energy is 546 keV and the other is coming from the $\beta-$ disintegration of the ^{90}Y, whose endpoint energy is 2284 keV, being thus energetic enough to be able to pass through the aluminium sheet and to deposit energy in the crystal.

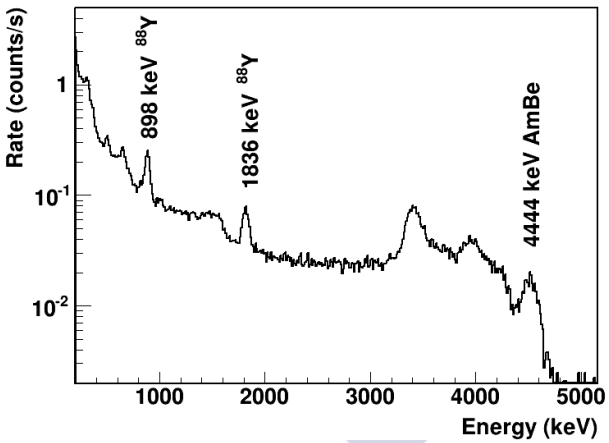

Figure 3.4.: ^{88}Y+AmBe spectrum acquired using $CeBr_3$-PMT detector.

3.1.1.2. CsINa

Similarly to $CeBr_3$-PMT, the linear energy-channel calibration as well as the energy resolution depending on the energy (see Fig. 3.7. were calculated for CsI(Na)-PMT using the ^{152}Eu radioactive source.

In Fig. 3.8 is observed the ability of the CsI(Na)-PMT to detect γ-rays from 662 to 4444 keV with good resolution, although the detection

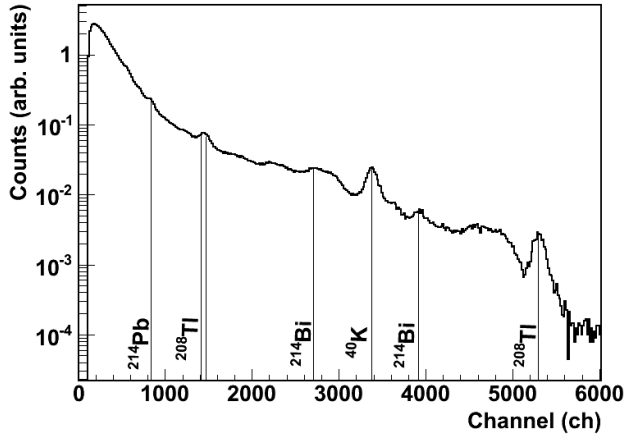

Figure 3.5.: Background radiation spectrum measured using $CeBr_3$-PMT detector. No intrinsic activity is observed.

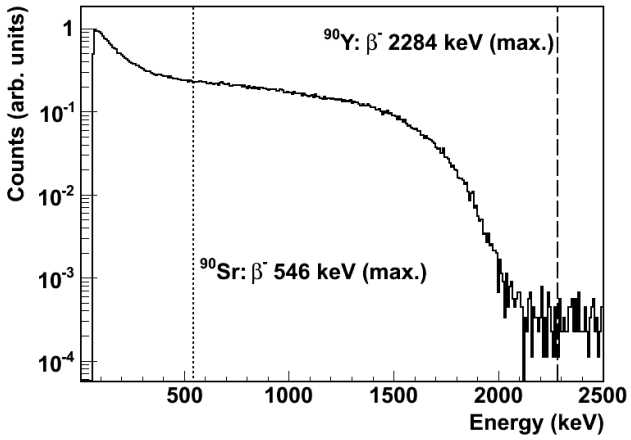

Figure 3.6.: ^{90}Sr spectrum. Note the two contribution of the desintegration branches at 546 keV and 2284 keV, after passing the Al wall.

efficiency becomes lower at the higher energies.

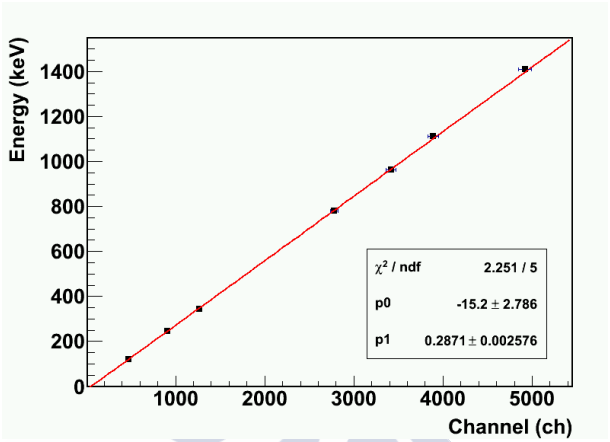

(a)

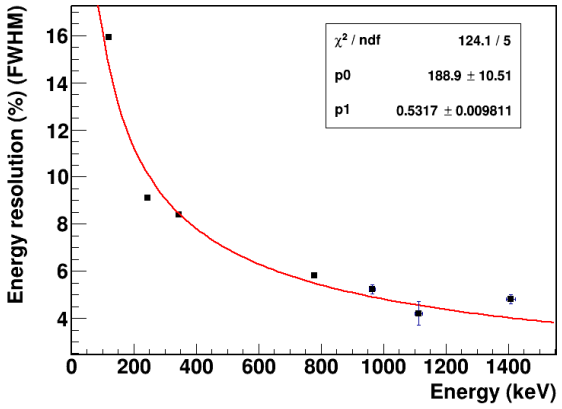

(b)

Figure 3.7.: Calibration energy (left) and energy resolution (right) for CsI(Na)-PMT

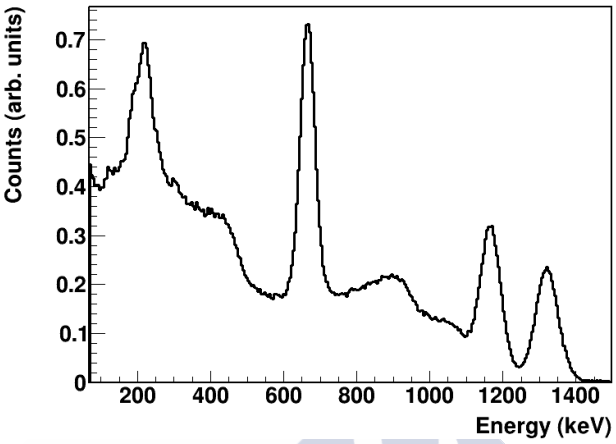

(a)

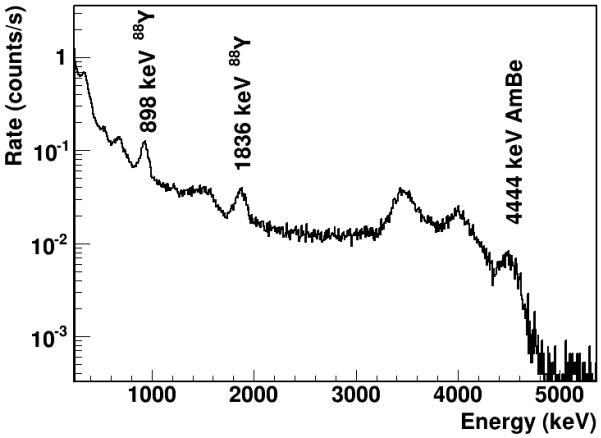

(b)

Figure 3.8.: CsI(Na)-PMT ^{137}Cs+^{60}Co (a) and ^{88}Y+AmBe spectra (b).

3.1.1.3. CsI(Na)-PIN

The CsI(Na)-PIN detector also shows a good linear behaviour. See Fig.3.9

In Figs. 3.8 and 3.10 the ^{137}Cs and ^{60}Co spectra measured by the CsI(Na)-PMT and CsI(Na)-PIN can be seen for comparison. Both detectors shows a good linearity. The photopeaks in the CsI(Na)-PIN are broader than in the CsI(Na)-PMT ones, meaning a poorer energy resolution.

3.1.1.4. CeF_3_L40-MPT

The CeF_3 is not a hygroscopic material, therefore its inner properties are not worsen in moisture presence and so it do not need to be encapsulated. Thanks to that the α particles emitted by a radioactive source, ^{238}Pu in this case, can interact with the crystal and deposited their energy in it. Conversely both $CeBr_3$ and CsI(Na) crystals were encapsulated, as it was described in Section 2.3.1, due to their hygroscopicity, preventing so to measure α particles coming from ^{238}Pu, since they stopped in the material used for sealing.

The chain of measurement consists on the CeF_3_L40-PMT coupled to the *strectcher* PCB designed for the $CeBr_3$-PMT. In the CeF_3_L40-PMT case this PCB behaves linearly, and the output was directly plugged to the SA CANBERRA 2022 that provides the shaped signal to be acquired by the MCA from AmpTek.

When the detector measured 662 keV γ-rays from ^{137}Cs the energy resolution for such photopeak was 31.9% as can be seen in Fig.3.11, what it is clearly poor than the other crystals. These signals will be used later when dealing with the PSA studies.

Concerning the α particle test, three configurations, in order to besure that α were detected:

a) the α source in contact with the input window of the CeF_3.

b) a gap of 1 cm of air between the source and the input window of the crystal.

c) a sheet of paper interposed between the source and the input window

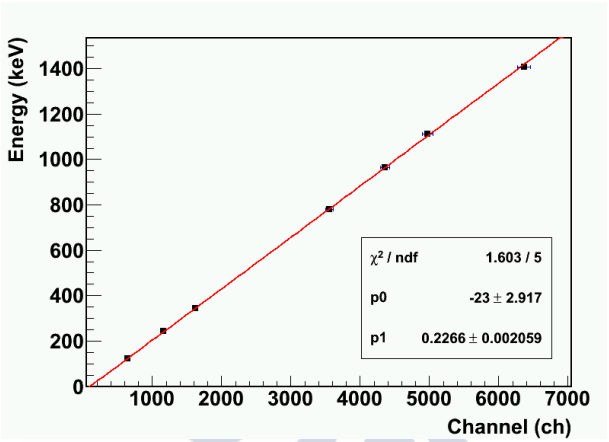

(a)

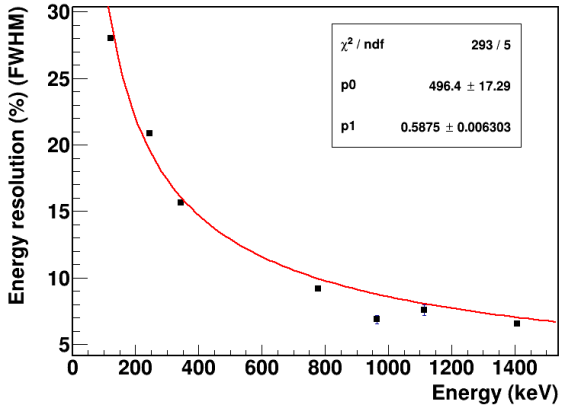

(b)

Figure 3.9.: Calibration energy (left) and energy resolution (right) for CsI(Na)-PIN.

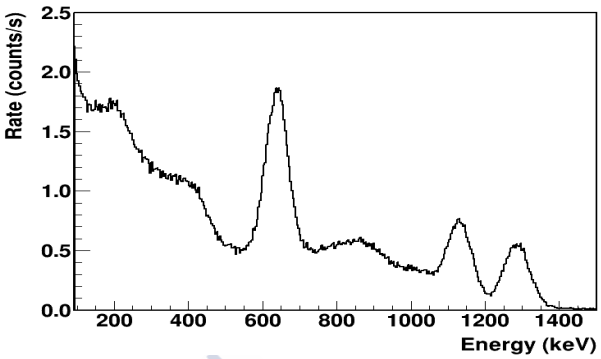

Figure 3.10.: 137Cs+^{60}Co spectra acquired using PDCsINa detector.

of the crystal.

The three spectra acquired can be seen in Fig. 3.11, where the ^{137}Cs spectrum is drawn in the same canvas as a reference of deposited energy. As well-known, the α particles energy-loss follow the Bethe-Bloch formula being quickly attenuated in only few centimeters. In the case of the ^{238}Pu the α particles are completely attenuated in 6.6 cm length in air [45]. Despite the initial energy is 5.593 MeV when referencing the α spectrum to the 662 keV γ-rays, the deposited energy appears much lower even in the configuration (a). This can be explained by the non-linear response to the energy deposition due to high ionisation density produced very close to the crystal boundary, what it is observed in all scintillators [51, 52]. Concerning the results for the configurations (b) and (c), the energy deposited is lower as expected because the interposed material.

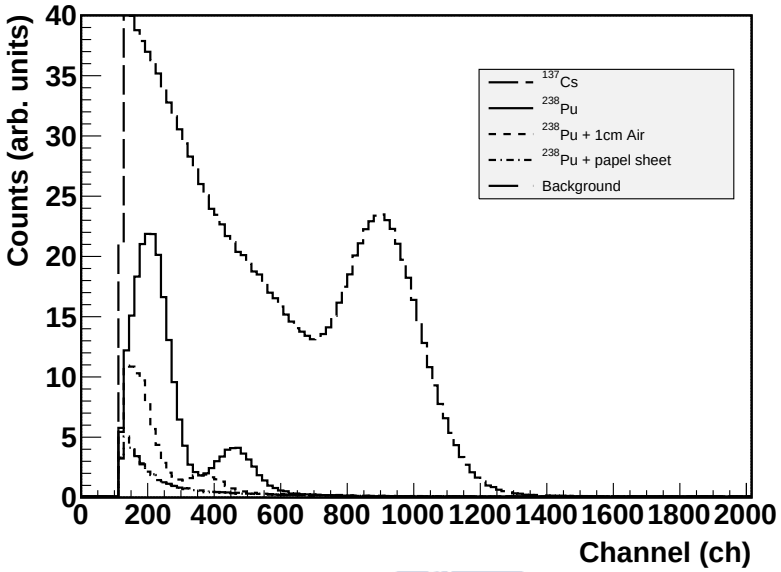

Figure 3.11.: ^{238}Pu spectrum using CeF_3_L40-PMT for different set-ups. The ^{137}Cs spectrum is added as deposited energy reference.

3.1.2. Temperature dependence

The scintillation process is claimed to be temperature dependent, and differently for every material [18]. Similarly, the photodetectors based on Si shows also a worsening of the detection performances as the temperature increases, due to the creation of dark currents contributing to the noise in the output signal. CsI(Na)-PMT, CsI(Na)-PIN and $CeBr_3$-PMT detectors were tested in order to know their behaviour when temperature varies in a range around the room temperature.

All the set-ups for the temperature measurements were performed inside a light-tight box (60x50x27 cm^3) made of wood covered with cooper to avoid the environment RF noise. A thermometer, RS-1315 type K [53], by RS Components, set in contact with the detectors. The thermometer readout was watched by a PC, getting an accuracy of ±0.5 %. The sampling rate is 0.5 Hz (2 s.)

Temperature dependence for CsI(Na) A set of ^{137}Cs spectra was acquired in 15 minutes slots with a time lapse of 3 minutes in between, whereas the average temperature was recorded for every slot. The total measured time was 6 hours and the temperature variation was 1.8 ^{o}. In

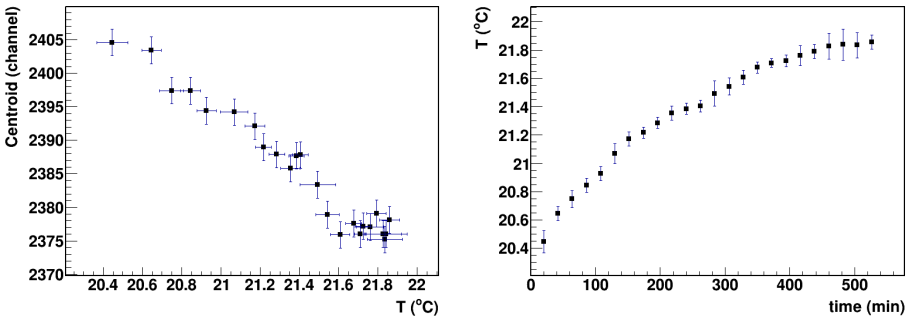

(a) (b)

Figure 3.12.: Centroid temperature dependence CsI(Na)-PMT detector.

Figure 3.12, can be seen how decreases the centroid position related to the detector gain, whereas the temperature is increasing; the temperature

data were averaged over the 15 min time slot of every data taking. On the other hand, the energy resolution has not a clear temperature dependence.

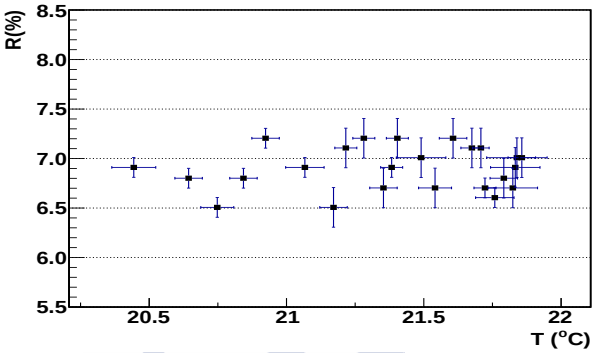

Figure 3.13.: R temperature dependence CsI(Na)-PMT detector.

Temperature dependence for CsI(Na)-PIN In order to measure in a wider range of temperature, a cooling brick was introduced inside the light-tight box close to the detector. Once the temperature is stabilised at its lowest value, the cooling brick was extracted and the measurements started. The temperature was sampled at a rate of 0.5 Hz (2s), while the ^{137}Cs spectrum was acquired for 2 min time slots with time lapses of 1 minute between them. See the temperature evolution along the time in Fig 3.14 (b).

A similar behaviour than that of the previous study was observed. The energy resolution is not affected by the variation of temperature in the range of studied as it seen in Fig. 3.15.

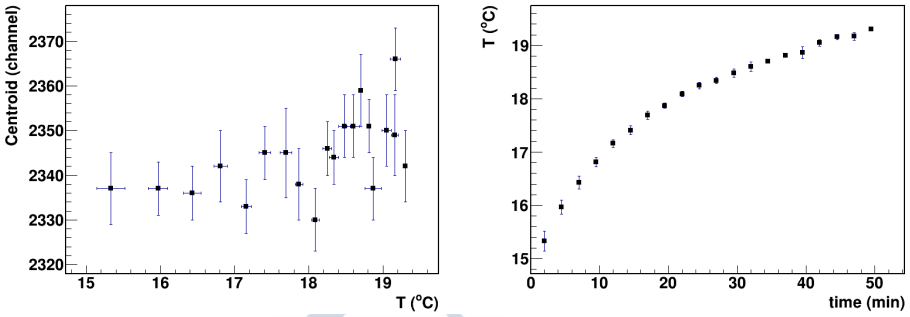

(a) (b)

Figure 3.14.: Temperature variation over the time for CsI(Na)-PIN detector.

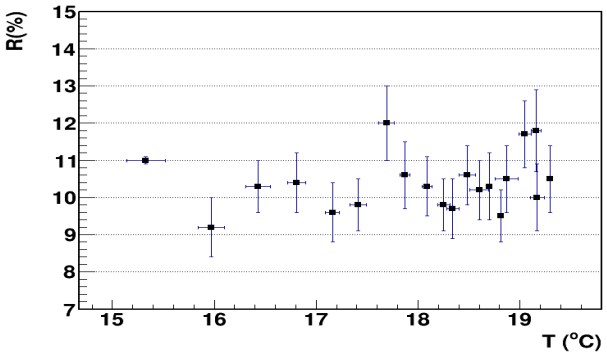

Figure 3.15.: Resolution variation over the temperature for CsI(Na)-PIN detector.

Temperature dependence for $CeBr_3$-PMT The method to measure the temperature variations was the same than described for the CsI(Na)-PIN. The temperature range measured in this case, can be seen in Fig. 3.16

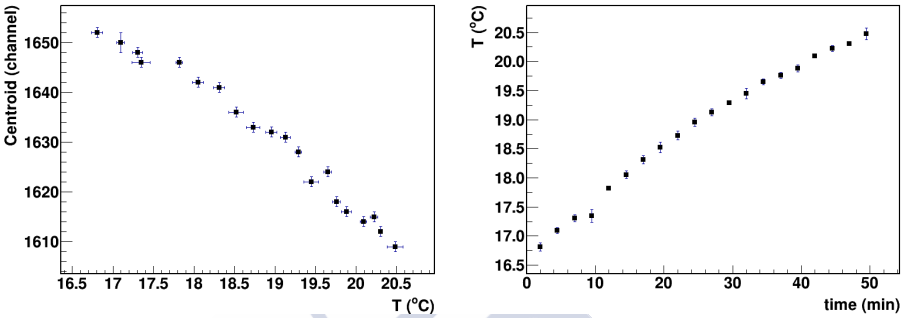

(a) (b)

Figure 3.16.: Temperature variation over the time for $CeBr_3$-PMT detector.

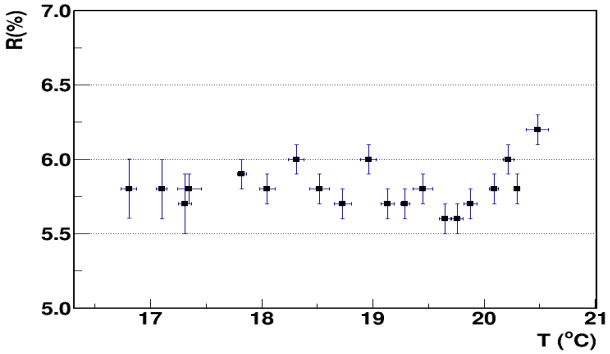

Figure 3.17.: Resolution variation over the temperature for $CeBr_3$-PMT detector.

As it was shown in the preoviuos measurments, for the $CeBr_3$-PMT the temperature do not greatly affect the resolution values obtained for the photpeak of 662 keV γ-rays. This agrees with Fig. 9 in Ref [54], where the deviation of the L.Y. is around 1 % in the range of temperatures studied.

3.2. Pulse Shape Analysis

The shape of the pulses generated by either the ionising particles or the γ-rays is an brings out some information about its kind. The signals produced by the interaction of different ionising particles γ-rays, β particles and cosmic-muons will be analysed in this Section using the techniques described in Chapter 1

3.2.1. PSA through digital algorithms

The signals provided by the scintillator detectors, $CeBr_3$-PMT and CsI(Na)-PMT, were acquired and digitised by the oscilloscope YOKOGAWA DL9140 (Max. sampling rate 5Gs/s and Freq. BW = 1GHz) and transferred to a PC for the analysis explained in the following sections.

3.2.1.1. Raw signal analysis

The decay time of each detector was firstly calculated by a fitting method; secondly the shapes of the signals produced by the three different particles mentioned previously were compared; and finally, the timing resolution of the detectors was obtained by the coincidence with an ultra-fast organic scintillator detectors.

Decay time constant In order to obtain the decay time for each detector, the profile of a set of signals haven been calculated. The profile consists on the calculation of the mean value of each same sample of the many signals acquired. In this case, the signals were produced by the 622 keV γ-rays from a ^{137}Cs source. The decay time constants were calculated from a exponential fitting (as shown if Eq. 2.8) of the decay time of the profile. Figs. 3.18 (a) and (b), show the fitting for $CeBr_3$ and CsI(Na) respectively. The τ_{CeBr_3} is 12 ns, in agreement with the value provided by the references in Table 2.1. When fitting the CsI(Na) profiles two decay time constants have been found : $\tau_{1,CsI(Na)} = 473$ ns and $\tau_{2,CsI(Na)} = 2588$ ns. The first constant differs from the provided in Ref. [9], where the value is 630 ns. But it is excelent agreement with Ref. [55] where a decay

constant equals to 472 ns have been reported. The result of 473 ns found in this work rules out the value of 630 ns given by Saint-Gobain Crystals [9].

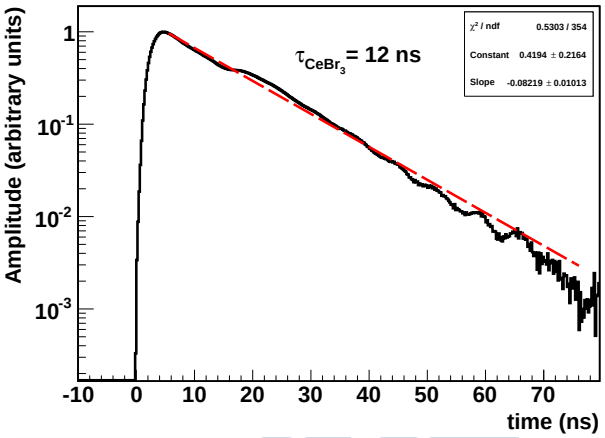

(a)

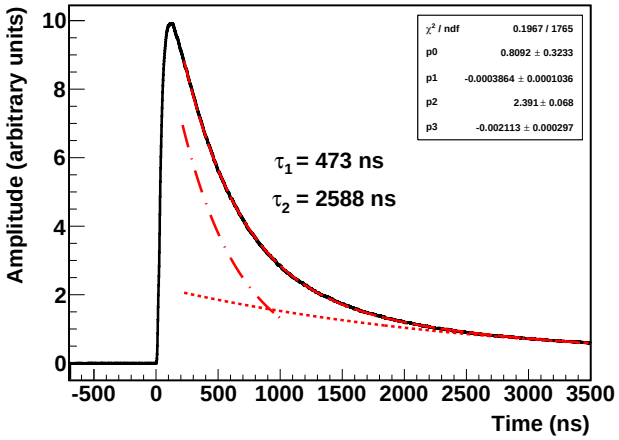

(b)

Figure 3.18.: $CeBr_3$ and CsI(Na) decay times.

Pulse shape for γ-rays, β particles and cosmic-μ's The linearity is relevant when studying both the timing and energy resolution properties of the detectors. The profile of a set of signals from three different ionisation particles (γ-rays from ^{137}Cs, β particles from ^{90}Sr and cosmic-μ's) has been calculated in order to find out if their respective pulse shape show variations. The setup for measuring the cosmic-μ's is detailed described in Section 3.2.1.1

In Figs. 3.19 and 3.20 the profiles for each ionisation particle has been normalised to the integral of the pulse. It is is remarkable that, both for $CeBr_3$-PMT and CsI(Na)-PMT, the three pulse shapes are similar without any noticeable deviation. It worth mentioning that mean maximum amplitude of the cosmic-rays μ's is around 10 times larger than the case of the corresponding to the 662 kev ^{137}Cs, concluding the noteworthy linearity of both detectors.

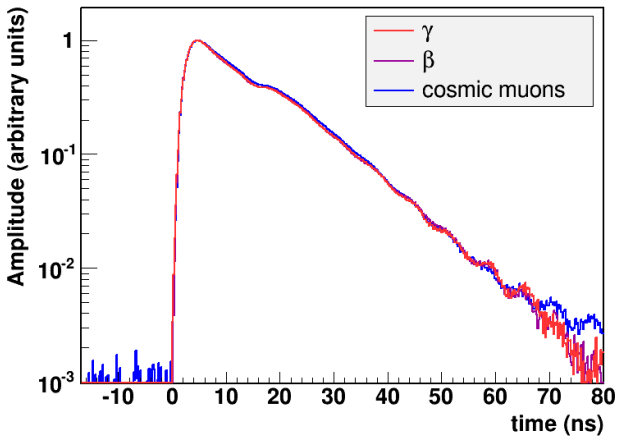

Figure 3.19.: $CeBr_3$-PMT profiles for γ-rays, β particles and cosmic-rays.

Timing resolution A plastic model EJ-232 from ELJEN TECHNOLOGY, wrapped with a foil of mylar and black adhesive tape, coupled to a PMT mod. R4998 by means of a Silicon Interface Pad. BC-634A, manufactured by Saint-Gobain Crystal, was placed in parallel with the scintillator detector. The signals produced both in plastic detector and in the scintil-

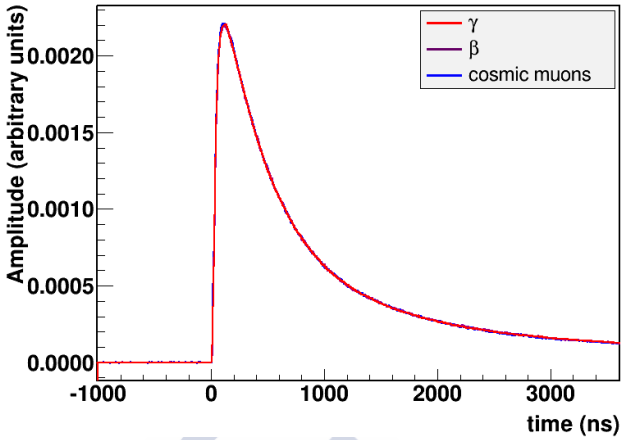

Figure 3.20.: CsI(Na)-PMT profiles for γ-rays, β particles and cosmic-rays.

lators detectors were registered in the oscilloscope YOKOGAWA DL9140 using a coincidence trigger. Most of these registered events are cosmic rays muons, the most abundant charged particles at sea level, whose mean energy corresponds to $\approx$ 4 GeV [3]. The incident angle of the majority of muons at sea level is close to the zero zenith angle and their flux is $\sim$ 1 muon/cm^2 minute.

The time resolution (σ) was is obtained by the characterisation of the statistical distribution of (t_{CeBr_3}-$t_{Plastic}$), where t_{CeBr_3} is time obtained by the intersection of the linear extrapolation of the rising edge with the baseline. The $t_{Plastic}$ is the time when the signal crossed a constant threshold. The rising time of the plastic scintillator is shorter than 4 samples of the digital signal.

The distribution was fitted with a gaussian function. As shown in Fig. 3.21 the timing resolution (σ) for the $CeBr_3$-PMT is 0.230 ns.

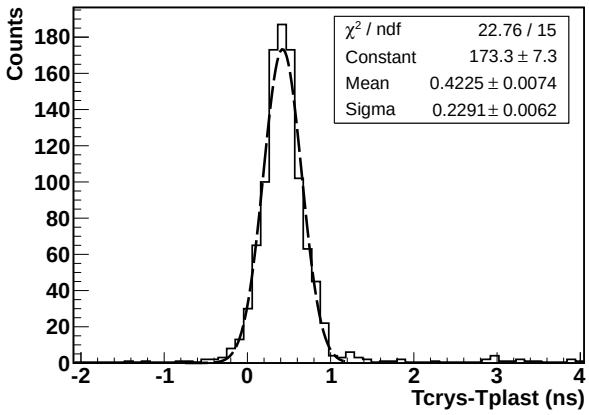

Figure 3.21.: $CeBr_3$-PMT timing resolution distribution.

3.2.1.2. Using Triangular and Trapezoidal filters

Triangular smooth The registered output signals from CsI(Na)-PMT, produced by γ-rays from ^{137}Cs and ^{60}Co sources, shows an inaccurate shape that hinder the accuracy when defining the observables. To improve such inconvenient, a smooth filter is passed over the original signals. A triangular filter is chosen an its number of parameters is 5. The filter is passed twice over the signal. In Fig. 3.22 the improvement in the shape for one signal can be appreciated. Fig. 3.23, the rise region is enlarged to show the improvement in the shape of the original signal after one and two pass of the smooth filter.

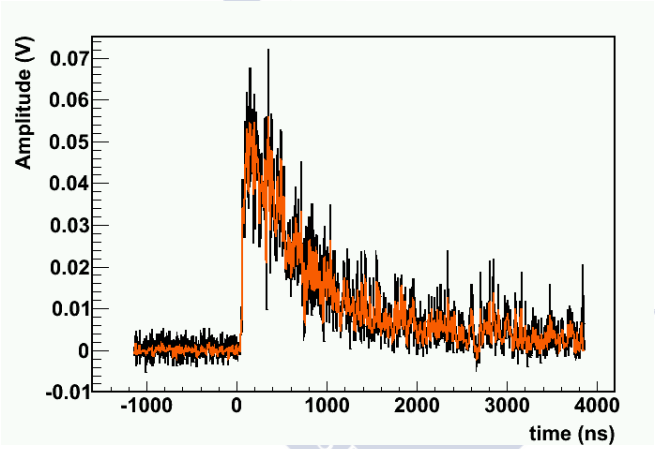

Figure 3.22.: Original pulse from CsI(Na)-PMT (black) and smoothed pulse (orange).

Once the signals have been conditioned, the same procedure that was detailed for the $CeBr_3$-PMT detector is used to calculate de CsI(Na)-PMT timing resolution. The timing distribution is shown in Fig.3.24 where the timing resolution (σ) 0.920 ns for the CsI(Na)-PMT.

The observable pulse area have been calculated for the set of pulses. This observable contained information about the deposited energy of the γ-rays emitted from the ^{137}Cs and ^{60}Co. In Fig. 3.25 the distribution of this observable can be seen. The three photopeaks emitted by the sources, 662 keV, 1173 keV and 1332 keV can be distinguished. The peak at 662

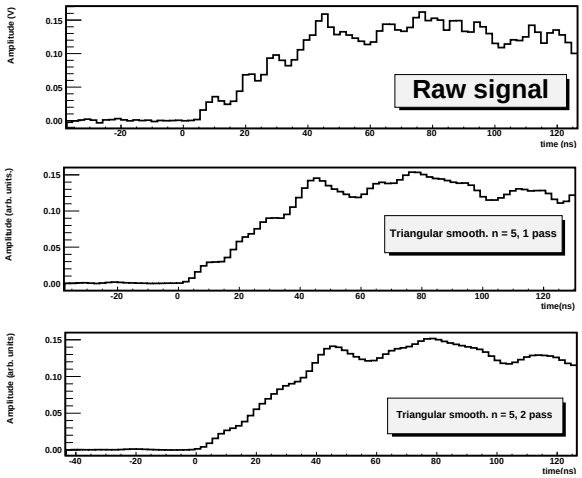

Figure 3.23.: Rising time for a CsI(Na)-PMT pulse. Upper Fig. Original signal. Middle Fig. Signal after one pass 5^{th} order triangular smooth. Lower Fig. Signal afer two pass 5^{th} order triangular smooth.

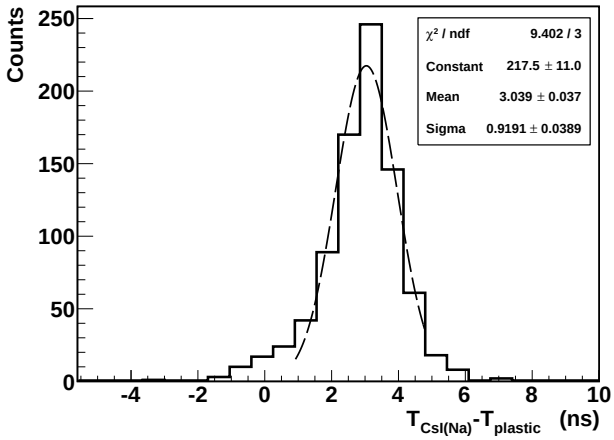

Figure 3.24.: CsI(Na)-PMT timing resolution distribution.

keV was fitted using a Gaussian function in order to obtained a energy resolution value of such spectrum. The resolution obtained is R(%) = 6.7 ± 0.1, which is in agreement with the resolution value measured using the spectroscopic chain in Section 3.1.1.2.

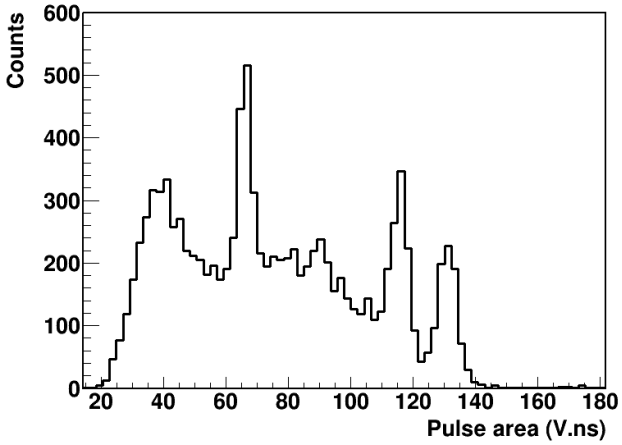

Figure 3.25.: ^{137}Cs and ^{60}Co spectrum obtained after a smoothing of CsI(Na)-PMT signals. The energy resolution for 662 keV R(%) = 6.7±0.1

Trapezoidal filter The trapezoidal filter was applied to the digitised points of the pulses produced by the $CeBr_3$-PMT. In Fig. 3.26 the original signal and the filtered can be seen. The parameter chosen was L = 12 ns, G = 4 ns. It is noticeable the reduction of the SNR that simplifies the calculation of the observables such as time stamp, pulse height or area. Figs. 3.27 shows a ^{137}Cs and ^{60}Co pulse height spectra for $CeBr_3$-PMT. The peak was fitted to a Gaussian function, giving as a result an measured energy resolution R(%) = 8.2 % 0.1, a value poorer than in the measured in the case of the spectroscpic chain case. See Section 3.1.1.1.

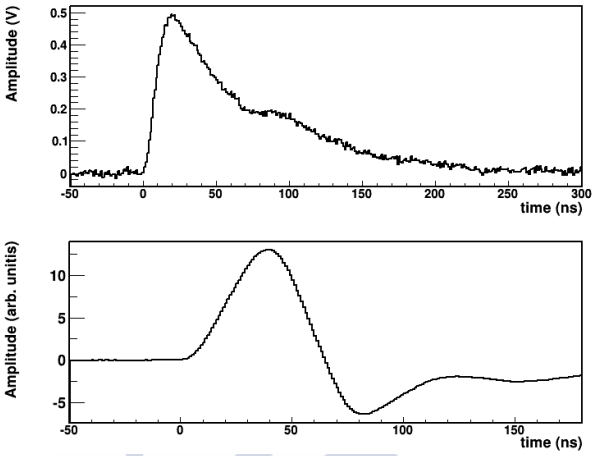

Figure 3.26.: Raw signal from $CeBr_3$-PMT (above). Filtered signal using a trapezoidal filter (below).

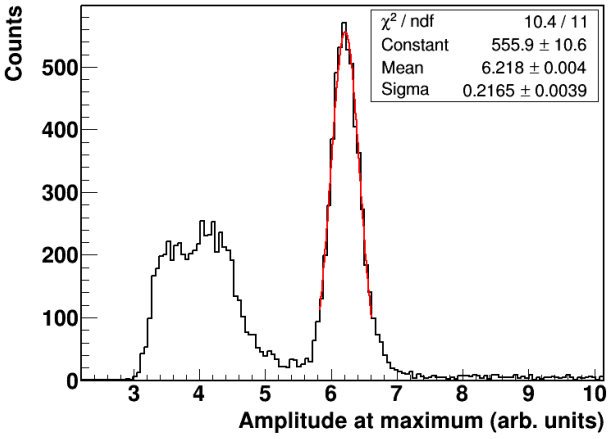

Figure 3.27.: FIR filter ^{137}Cs spectra obtained from the filtered signal of $CeBr_3$-PMT using a trapezoidal filter. R(%) = 8.2 ± 0.1

3.2.2. α/γ identification using CeF_3_L40-PMT

Some scintillators have properties that made them appropriate for particle identification. By means of the study of PSA the identification can reveals, for intance, through the different decay time components of the crystal. The CeF_3 crystals have been used for such purpose as it seen in Ref. [56]. In this section, an analysis of the shape of the pulses, applying some techniques explained in previous sections, provided by an α and γ-ray source is shown.

Two sets of measurements were made:

- A set of 40000 signals produced by α particles emitted by a ^{238}Pu radioactive source
- A set of 40000 signals produced by γ-rays emitted by a ^{152}Eu radioactive source

both were recorded and registered by the oscilloscope YOKOGAWA DL9140 for further analysis.

Profile identification The profile of each set of signals shows that the pulses produced differ in shape depending on the incident particle or γ-ray.

In Fig. 3.28 (a) both profiles were normalised to their respective areas. In (b), the profiles were normalised to the maximum amplitude. In both figures it differences in shapes are obviuos. Therefore, this leads to define observables related to such differences.

Event-by-event analysis The method consists in the analysis of the raw signals produced by the detector after correcting the baseline through the subtraction of the mean value of the firsts 12ns recorded by the oscilloscope. Taking into account the differences observed in the profiles, the observables are defined: the slope of the rise time of the pulse calculated by a linear fitting taking as a range the time stamp when the signal overcome an constant amplitude trigger and after at least 3.6 ns is increasing and the signal area in a fix interval after the initial time plus 3.6 ns and 140 ns.

The results obtained are shown in Fig. 3.29. The observables previously

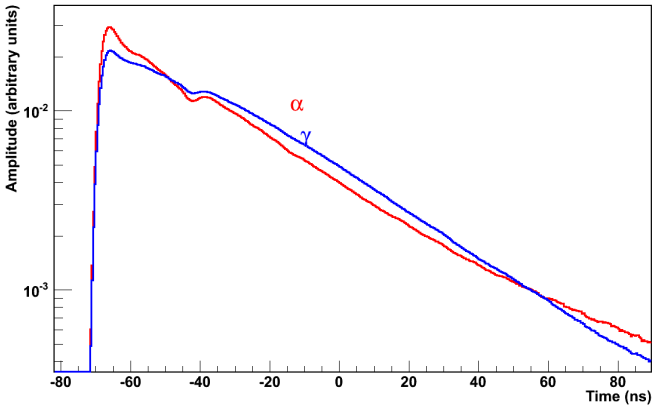

(a)

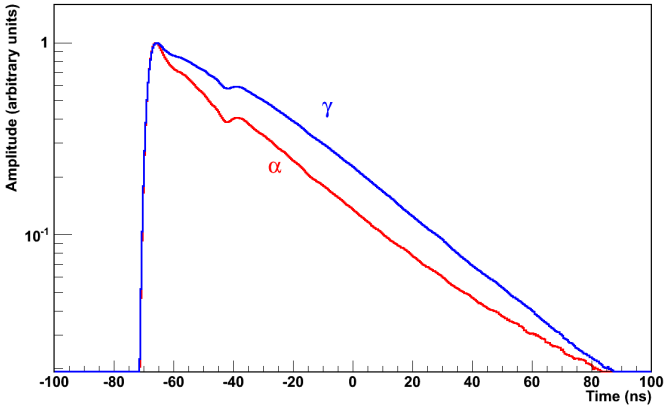

(b)

Figure 3.28.: CeF_3_L40-PMT profiles of a sets, one for α particles, one for γ-rays, of digitised signals from CeF_3_L40-PMT detectors. Fig. (a) shows the profiles of both sets normalised to the area of each profile shape. Fig. (b) shows shows the profile of both sets normalised to the amplitude of each profile shape.

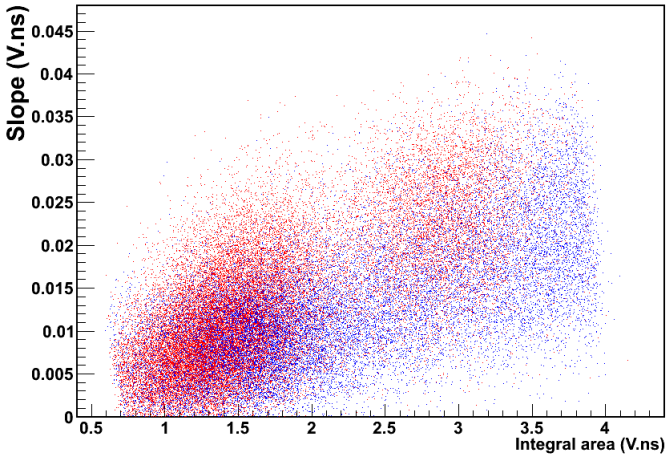

(a)

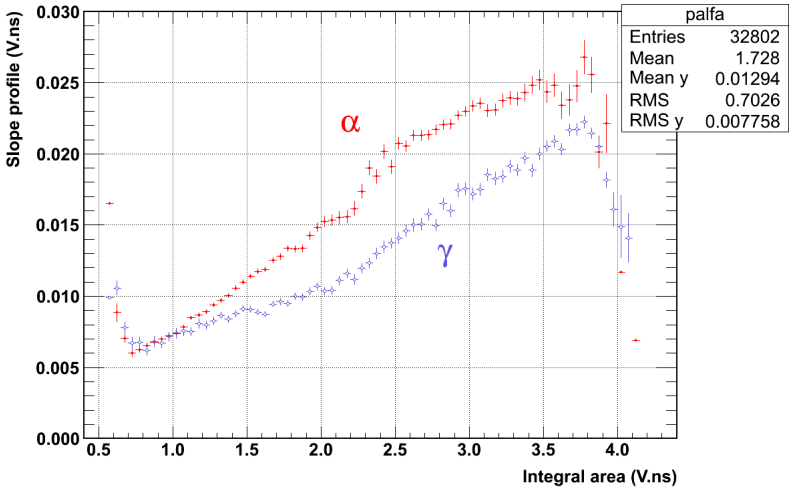

(b)

Figure 3.29.: (a) Slope as a function of the integral area event-by event. (b) Mean slope value as a function of integrated area. Note the splitting between α and γ-rays samples.

defined are plotted in Fig. (a) were α particles are the red dots and γ-rays the blue ones. It is observed that there is a slightly difference for both detected but not clearly. Using the profile again for each particle, Fig. (b) it is clearer that from values 1.0 to 3.5 of integral area a identification is possible, however it is not strong enough to discriminate α from γ-rays.

3.3. Conclusions on the results

The results obtained in this Chapter show that the linearity of the detector is obtained by using the *strecherPCBs* designed and proposed in Chapter 1. The obtained value for the decay time of the CsI(Na), $\tau_1 = 473ns$, ends with the controversy found in previous works. The FIR filters triangular and trapezoidal were applied to filter the signals for $CeBr_3$-PMT and CsI(Na)-PMT detectors. The results conclude that passing such filters improve the calculation of observables, such as the timing resolution, and still contained the information of the original signals. A method in order to discriminate α particles from γ-rays was proposed. The results shows that the signal produced by both show difference nevertheless, the ability of the method is not stronger enough to discriminate such particles events by events.

The results obtained for the energy resolution in this chapter are shown below:

Detectors' comparison The resolution of the 662 keV peak was calculated from the parameters of a Gaussian function plus a linear function [49] were fitted to the peaks after subtracting the background γ-ray spectrum from the initial spectrum.

The resolution values obtained by the fitting of Fig. 3.2 (b), 3.7 (b) and 3.9 (b) are also shown in Table 3.1. In Table 3.2 the results for CeF_3_L40-PMT and CeF_3_L50-PMT detectors can be found.

Scin. detector	$CeBr_3$-PMT	CsI(Na)-PMT	CsI(Na)-PIN
R(E) at 662 keV (Best value)	5.4±0.1	6.4±0.1	9.4±0.3
R(E) at 662 keV (Mean value)	5.6±0.1	6.7±0.1	10.4±0.1
R(E) at 662 keV ($^{152}Eufit$)	5.8±0.1	6.3±0.1	10.9±0.1
R(E) at 662 keV (FIR filters)	8.2±0.1	6.7±0.1	-
R(E) at 1 MeV ($^{152}Eufit$)	4.6±0.1	5.1±0.1	8.5±0.1

Table 3.1.: Energy resolution for CeB_3-PMT, CsI(Na)-PMT and CsI(Na)-PIN scintillator detectors.

Scin. detector	CeF_3_L40-PMT	CeF_3_L50-PMT
R(%) at 662 keV	31.9±0.1	35±3

Table 3.2.: Energy resolution for CeF_3_L40-PMT and CeF_3_L50-PMT detectors.

USC
UNIVERSIDADE
DE SANTIAGO
DE COMPOSTELA

4. Beam-tests in the n_TOF experiment

The significantly high flux of neutrons attainable from the high-intensity short-pulsed 20 GeV protons on the nTOF spallation target, together with the very special characteristics of the two lines of neutron time-of-flight, mades the n_TOF measurements superseding those at any other neutron source world around. These kind of facilities are devoted to enlarge and improve the existing libraries on nuclear data, that are foundations of Nuclear Science, because the knowledge of nuclear evaluated data is essential for the deeper understanding of many of the processes occurring in Nature. In particular, for disentangling the puzzle of the nucleosynthesis of elements beyond Iron in stars, via the s- and r-processes [57] and on the other hand, for boosting the development of technologies related to the better functioning of present nuclear reactors [58] as well as the future ones (Generation-IV) aiming at minimizing the production of nuclear waste or at burning it [59] in Fast reactors, namely in ADS [60]. This makes it necessary to perform new and more accurate measurements of many isotopes and reactions, which are summarized for instance by the Nuclear Energy Agency in its High Priority Request List [61].

In Chapter 3, the detectors have been characterised in a lab bench, where the measurement conditions can be largely controlled, whereas in an experimental area devoted to the study of nuclear reactions the environment becomes challenging when performing the measurements. The scintillator detectors previously characterised were moved to the n_TOF experiment facility at CERN in Geneva (Switzerland), in order to test their behaviour in a real environment, providing new information for future possible use in new detectors.

This chapter deals with the measurements related to the n_TOF facility at CERN) done in the frame of this Thesis work. The detectors $CeBr_3$-PMT and CsI(Na)-PMT were firstly tested in the n_TOF facility by measuring the prompt γ-ray emission in the neutron capture reactions

(n,γ) for the isotopes ^{197}Au and ^{nat}Ag. In addition to this, the prompt-γ produced in neutron-induced fission ^{235}U(n,f) were measured in coincidence with the PPAC gaseous chambers. Then, after a brief description of the n_TOF facility, the measurements and results obtained on the study of its γ-flash are shown in Section 4.4.1.

4.1. n_TOF Facility

The neutron time-of-flight facility n_TOF features a white neutron-source produced after nuclear spallation reactions in the hadronic cascades originated in a huge lead target by protons bunches of 7 ns (rms) from the Proton Synchrotron (PS) of 20 GeV/c, having 7x10^{1}0 ppp, at a repeating rate of 0.8 Hertz. The facility, aiming primarily at the measurement of neutron-induced reaction cross sections, was operative at CERN between 2001 and 2004, and then underwent a major upgrade in 2008 (See Ref. [62] and references therein). The required high energy-resolution is attained by making the pulsed neutron-beam, that spans over an available energy range wide of ten decades, to travel a distance long of 185 m before reaching the sample under study. In this technique the kinetic energy of the neutrons is so determined from their time of arrival at the measuring station, ranging from some 600 ns, for those travelling close to the speed of light, up to around 80 ms for the thermal ones.

The lead spallation target, whose dimensions are 40 cm long and 60 cm in diameter, is sketched in Fig. 4.2. Two different water layers are besides the target: one of 1 cm of distillated water acting as cooler and another of borated water, 4 cm wide, that works as moderator of the initial fast neutrons to enhance the low energy part of the spectrum. A wider and flatter energy spectrum, from thermal energy to relativistic neutrons, was so obtained (see Fig 4.3).

During the spallation process, besides neutrons, a huge quantity of particles are produced due to both electromagnetic and hadronic processes. Therefore, the neutron beam line is tilted 10^o respect to the proton beam, in order to suppress the presence of some of the produced neutral particles such as π^0, K^0 and Λ, as well as reducing the g-flash.

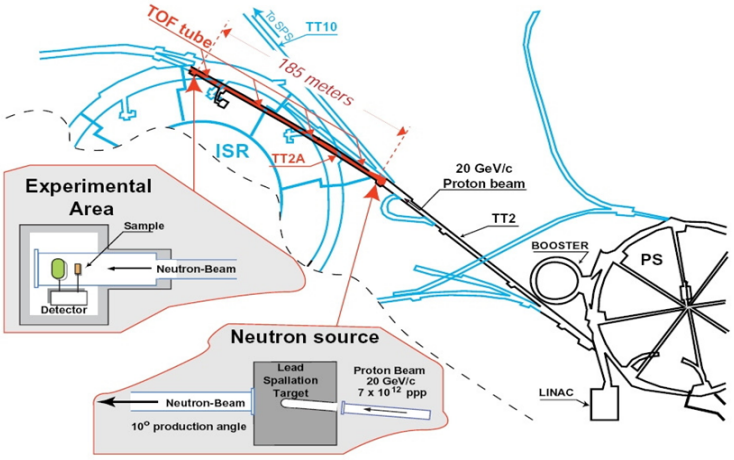

Figure 4.1.: n_TOF facility

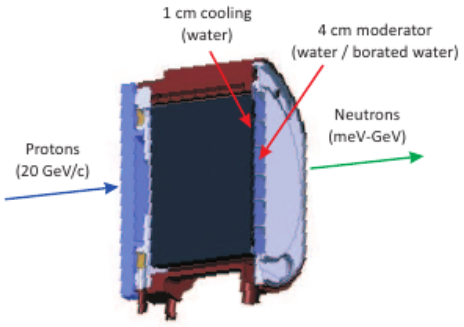

Figure 4.2.: Lead spallation target.

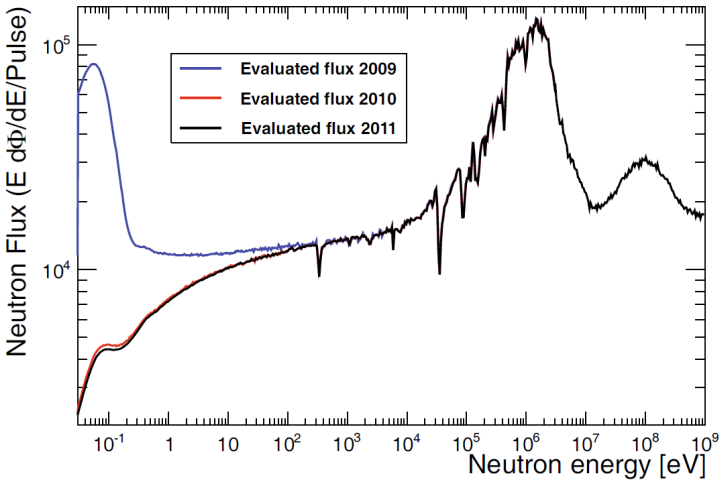

Figure 4.3.: Evaluated neutron flux for different spallation targets in the EAR1 [10].

To sum it all up, the n_TOF facility provides a very high instantaneous intensity of around 10^7 neutrons/pulse in a collimated beam of 3.5 or 10 cm, and an excellent energy resolution in the complete energy interval of interest. Due to these characteristics, the n_TOF facility stands today among the world leading facilities for measuring neutron-induced reactions.

Beam line to EAR1

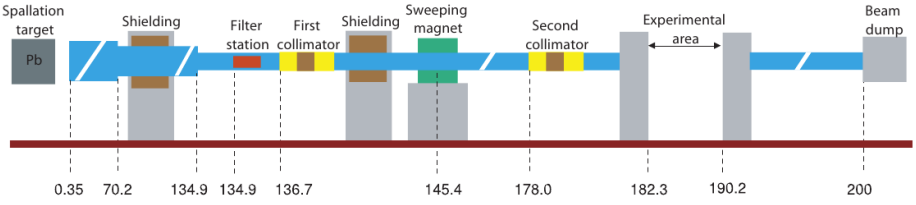

Figure 4.4.: Beam line EAR1.

This beam line was done taking advantage of a service tunnel already existing at CERN. It goes from the spallation target to the Experimental

Area 1 (EAR1), having a length of 182.3 meters with different elements that are placed all along the beam line, as sketched in Fig. 4.4. In order to clean-up the neutron beam a 3.6 Tm sweeping magnet (200 cm in length, 44 cm gap) at 145.4 m, deflects the charged particles that are in the beam. After this magnet, at 151 m, a 3.2 m thick iron wall plays a role as μ shielding because of the in-flight decay products (mainly μs and νs) from the $K^{\pm}$s and $\pi^{\pm}$s coming from the spallation process. The coarse shielding at around 80 m and two collimators are included in the beam-line in order to get a well defined neutron beam, as clean of halo as possible. The first collimator is at 136.7 m and the second one at 178 m. Two configurations for the second collimator can be chosen, depending on the measurement requirements: a 18 mm diameter with 235 cm of steel plus 50 cm of borated polyethylene is chosen to measure capture reactions, and a 80 mm diameter, with 50 cm of borated polyethylene, plus 125 cm of steel, plus further 75 cm of borated polyethylene, to measure fission reactions. A 3 m width broad concrete wall separates the previous elements from the EAR1. Finally, a 1.6 m deep concrete wall at 190 m separates the EAR1 from the DAQ area. where the experimental set-up is deployed; the beam line prolongs some 10 m from the end of the EAR1, performing a scape-line ending in a borated polyethylene cube at 200 m, to dump the beam [62] in order to minimise the back rebounding neutrons [63].

Beam line to EAR2

In summer 2014, a new neutron beam line was added to the n_TOF facility, going to the Experimental Area 2 (EAR2). It is vertically oriented, starting on top of the spallation target, which is there surrounded by only the layer of 1 cm of de-mineralised water acting as coolant.The entrance window is made of an Al foil coupled to the vacuum pipe flange.

Different elements are distinguished along the beam pipe, at distances taken from the center of the spallation target. The first collimator at 7.4 m above the target, consisting of a Fe cylinder 1 m in length with 20 mm of inner diameter. At 10.4m a permanent dipole magnet is installed to deflect the charged particles produced during the spallation process. The magnetic field created is 0.253(4)T in the center of the magnet, whose length is 1.134 m. The integrated field of the magnet is 0.287 Tm. The

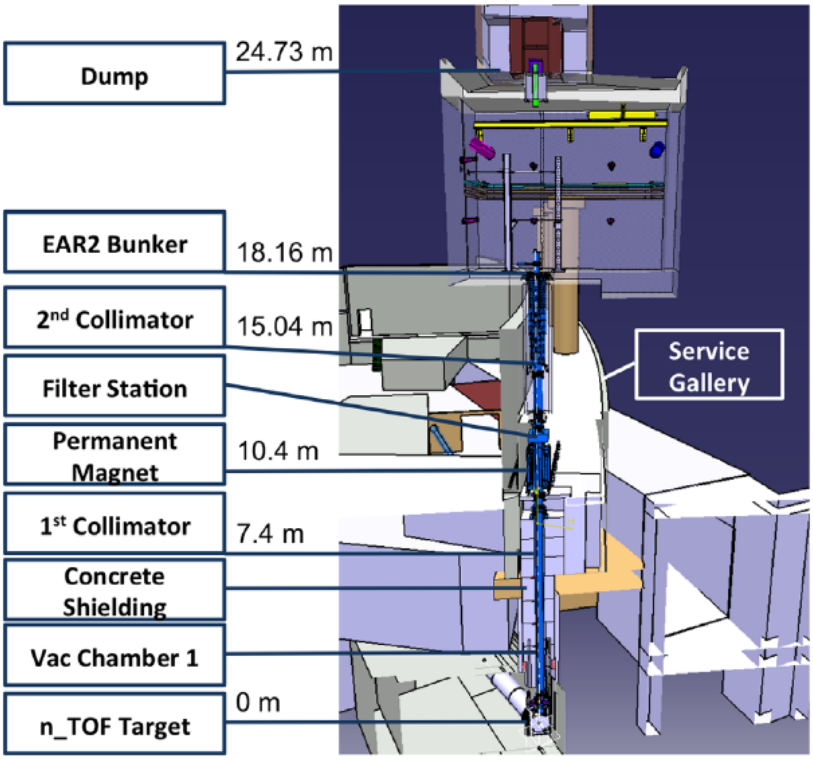

Figure 4.5.: Beam line EAR2.

dipole magnet inner gap is 340 mm, where the vacuum pipe is installed. A second collimator is installed at 25.04 m inside a large vacuum vessel with 680 mm outer diameter. The collimator consists of 2 m Fe and 1 m borated polyethylene (B-PE), where a core of boron-carbide (B-C) cylinders are inserted in the last 0.4m. The diameter of the collimator is variable following a conical shape, decreasing as the distance is closer to the experimental area, from 70.0 to 21.8 mm. The exit of the second collimator is situated at 120 mm below the floor of the EAR2. The focal point, which is theoretically the position of the narrowest spatial beam profile, is positioned at 1.08 m from the floor of the EAR2. The floor of the EAR2 is located at 18.16 m while ceiling is at 23.66 . The first meter from the floor is devoted to a neutron flux monitor, which is installed inside the vacuum pipes in the lowest section of the EAR2 and a Pb shielding. The different detection systems can be placed thanks to a set of support structures which are mounted on a pillar system the exit of the neutron beam. Finally, the beam dump is hanging from the roof of the building, being designed to respect the limits of dose rate of radiation protection for low-occupancy areas, 2.5 μSv/h, outside the building. It consists of three layer of B-PE, B-Fe core+ Fe blocks and concrete to fully the neutron beam. Fig. 4.5 sketched the beam line 2. See ref [64] for further details.

In order to minimised the background, the following considerations have been taked into account:

1. From 0.9 m above from the spallation target up to 7 m concrete elements are placed.
2. 4 tons of stainless steel spheres formed the shielding in the middle part of the beam line, from 12.6 m to 18.4 m.
3. Plates of lithium-polyethylene surrounding the beam pipe are placed on the floor of the EAR2 to absorb thermalised neutrons.
4. 57 cm of Pb disks are placed after the exit of the second collimator inside the vacuum chambers to reduce the γ background coming from the last section of the collimator.
5. Shielding elements such as Pb, B-PE and B_4C were placed in the last vacuum beam -line, fixed to the roof of the EAR2, just before the beam dump in order to reduce the photons and neutrons streaming

back to the detectors.

4.1.1. Detectors at the n_TOF facility

A wide variety of detectors are used at n_TOF for performing experiments to measure nuclear data from neutron-induced reactions as radiative capture, fission or light-nuclei spallation. Among these are: solid-state detectors, such as the silicon based neutron beam monitor [65] or CVD diamond detectors [66]; scintillation detectors, including a TAC made of BaF_2 crystals [13] and the C6D6 liquid scintillators [67] used for radiative capture detection; and, finally, gas-ionisation detectors, as the MicroMegas-based detectors [68], H19, a calibrated fission chamber from the Physikalisch Technische Bundesanstalt [69], or different sets of Parallel Plate Avalanche Counters, that are deeper described below [11, 12, 70].

Parallel Plate Avalanche Counters, PPAC

As already commented, the studies performed in this work were done using the scintillating detectors in parallel with the PPAC detectors that allow identify the (n,f) reaction events. Let's so to introduce the PPACs functioning and how they were used to our purposes.

Parallel Plate Avalanche Counters (PPAC) belongs to the gaseous detectors type that operate in proportional mode after application of an electric field between two parallel plates surrounded by a gas at low pressure. The type of gas in combination with its pressure and the distance that separates the plates, play an important role when detecting the charged particles passing through the detector.

In the proportional regime, the charged particle creates an specific number of pair electrons and positives ions that are drifted to the anode and the cathode respectively. During such drift, both the electrons and ions are able to create new pairs of electrons an ions. Such secondary electrons are accelerated enough due to the electric field that can ionise molecules and new electrons will be released creating an avalanche, form by a swarm of electrons that drifts to the anode, up to the gas moderate and extinguish it in a characteristic time given by the type of gas. The avalanche produced,

known as Townsed avalanche and proportional to the charge created in a first step following the Eq. 4.2 , induces charged both the anode an the cathode and as a result, a current signal is obtained where the electron contribution is much faster than the ions due to the fact that the mobility of the ions in a gas is around a 1% of the electrons. To a timing analysis the ions contribution will be filtered and remove of the output signal.

$$\frac{dn}{n} = \alpha \cdot dx \tag{4.1}$$

Where α is the firs Townsed coefficient. In the case that the electric field is uniform and constant, as in the case of parallel plate geometry, the coefficient α is a constant. Thus, the solution to the previous equation is:

$$N(x) = N(0) \cdot e^{\alpha x} \tag{4.2}$$

The gas used in the PPAC setup is C_3F_8, a non-flammable gas. The PPAC configuration adopted is illustrated in Fig 4.6 based on the model proposed in ref. The active area of detection is a 20 cm x 20 cm surface made of 1.5μm Mylar material coated with aluminium on each side. Both cathodes have the same size, however, the mylar suface is not continuous but stripped with a 2 mm pitch: on horizontally and the other vertically what allows the tracking of the FF traversing the PPAC detector, see Fig. 4.6. A gap of 2.5mm is in between the anode and each cathode. The bias voltage applied to the is 300V/cm·mbar.

Signal induced in both the anode and the cathodes are read and amplified by the associated electronics set in the plastic frame. In the case of the cathodes a delay line, connected to a preamplifier, is set at the end of the strips, being decoupled by capacitors of pF welded between the strips. The position of the avalanche is obtained by measuring the delay time between the pulse on the anode and the pulses propagating along the delay lines. The main advantage of the delay line is the reduction of readout channels: two per cathode instead of one per strip.

PPACs, as a detector working on the proportional regime, are not efficient for the detection of γ-rays since the probability for the γ radiation to interact in the gas is small. However, the detection efficiency for charged and FF fragments reaches up to 100%.

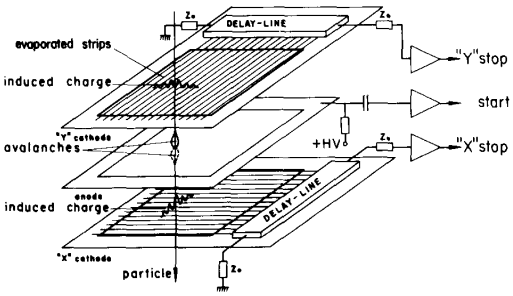

Figure 4.6.: PPAC schematic view. An anode in between of two stripped cathodes and their read-out electronics are represented. Note the induce charged in the three planes. [11]

PPACs offer great improvements over other types of detectors with regards to their time resolution, typically well below 1 ns (see Ref. [12] and references therein). Since PPACs are almost insensitive to gammas, they are widely used to detect fission fragments, even in a background with high levels of γ-rays or light charged particles. Unlike scintillator or semiconductor detectors, they are not damaged by radiation and can support high counting rates; this makes them useful for in-beam measurement of neutron and proton-induced reactions. In this work, it was taken advantage of these unique properties for tagging fission events when looking for coincidences with our scintillator detectors (see Section 4.3).

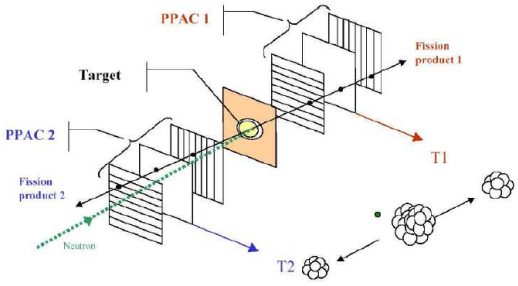

Figure 4.7.: Schematic working of a PPACs detectors

4.1.2. DAQ system

The n_TOF data acquisition system must so deal with signals having different shapes and characteristics, but for all of them its time stamp is crucial to be related every event with the neutron time of flight. A high-performance digital data acquisition system has been developed for the management and storage of the electronic detector signals. The system is based on flash analog-to-digital (fADC) modules, manufactured by Acquiris , with four input channels, ensambled in a cPCI crate housing up to 4 modules. The number of available channels is 60 in EAR1 and 32 in EAR2. The system has been recently upgraded to get an amplitude resolution of 8 to 12 bits, operating at sampling rates typically ranging from 100 MHz to 2 GHz, with a memory buffer of up to 175 MSamples, allowing for an uninterrupted recording of the detector output signals during the time-of-flight range of approximately 100ms. The fADC's starting time is picked-up from the CERN-PS proton bunches and when a time accuracy below 1 ns is required, the g-flash from the lead spallation target is used to get so the full time resolution (see Section 4.4.1) A fast zero suppresion algorithm can be performed in order to reduce the large quantity of date to be stored. When this option is chosen, once one detector's signal rises above a user-given trigger value, a data frame is selected containing only a given number of pre-samples and post-samples, before and after the selected signal.

A detailed description of this DAQ can be found in [71]. Once stored in digital form, in the memory blocks allocated to them, the electronic signals have to be of-line analysed, in order to obtain the time-of-flight and pulse information for each detected pulse.

The analysis routine for the PPAC detectors [70, 72, 73], removes the high-frequency oscillations in the baseline by means of a peak recognition function based on a derivative filter (Hanning filter). The original signal takes a bipolar shape after it has been derived, which it can be seen in Fig. 4.8. Peak discrimination is done by applying certain conditions to the derived signal. The negative part must arrive first, to ensure the negative polarity of the signal. The bipolar signal must then cross two thresholds (one positive and one negative) which were determined from the study of real signals. Additionally, the time between both peaks of

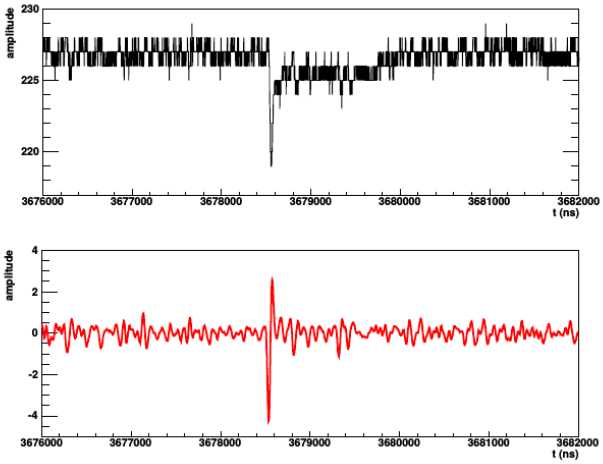

Figure 4.8.: Above: PPAC signal from an anode. Below: Filtered PPAC signal used for the analysis [12].

the derived signal and the ratio of both amplitudes are limited to certain values. Signals fulfilling all these requirements are kept and two parameters are stored for them in the DST file: the zero-crossing time of the bipolar signal and its peak-to-peak amplitude. The same pulse shape analysis is applied to all the PPAC detector channels.

4.1.3. Neutron energy calculation

The neutron kinetic energy is calculated from its path length of and the time-of-flight, according to the relativistic formula:

$$E_n = m_n c^2(\gamma - 1) \tag{4.3}$$

where m_n is the rest mass of the neutron, c the speed of light and γ the Factor. Expressing the Eq. 4.3 in terms of the flight path, L, and the time of flight, the equation leads to

$$E_n = m_n c^2 \left(\sqrt{\frac{1}{1 - \frac{1}{c^2}\left(\frac{L}{T}\right)^2}} - 1 \right) \tag{4.4}$$

For time of flight values $> 1\mu$s ($E_n \leq$ MeV), the classical expression for the kinetic energy, which corresponds to the first term of the Taylor series expansion of Eq. 4.4 , can be used.

$$E_n \approx \left(\alpha \frac{L}{t} \right)^2 \quad for E_n < MeV \tag{4.5}$$

where $\alpha \simeq 72.29$ when L is expressed in m, t in μs and E_n in eV.

In Fig. 4.9 (a) the difference between the relativistic and classical approximation can be appreciated. In (b), the relation neutron-energy time-of-flight is shown in the range where the prompt γ-rays from (n,γ) and (n,f) reactions are studied in this work. The kinetic neutron energy was calculated by using L $\simeq$ 185 m which corresponds to the flight path of EAR1 (L $\simeq$ 85 m for EAR2).

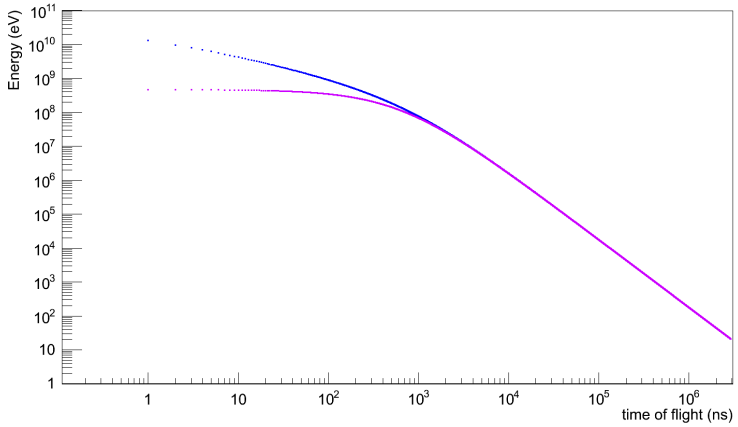

(a)

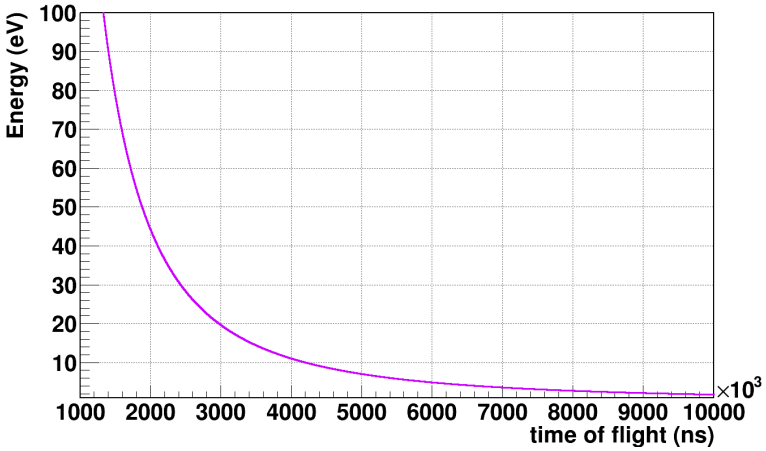

(b)

Figure 4.9.: Neutron energy vs time of flight. Note the difference at 1 μs between the relavistic (blue line) and the classical formula (violet line) (a). Neutron energy as a function of the time of flight in the region of interest to detect prompt γ-rays from neutron induced reactions.

4.2. Prompt γ-rays from (n,γ) reactions

The prompt γ radiation associated to the radiative neutron capture reactions was firstly used to characterise our scintillator detectors, comparing the results with those obtained in the lab-bench.

4.2.1. Neutron capture reactions ^{nat}Au(n,γ) and ^{nat}Ag(n,γ)

The neutron capture reactions were measured for two samples of 595.99 mg of ^{nat}Au and 807.41 mg of ^{nat}Ag using the $CeBr_3$-PMT and CsI(Na)-PMT detectors. In 2012 campaign the two scintillators were placed in EAR1 at 30 cm from the targets, accepting those photons forming an angle of 65° from the beam axis as is shown in Fig. 4.10.

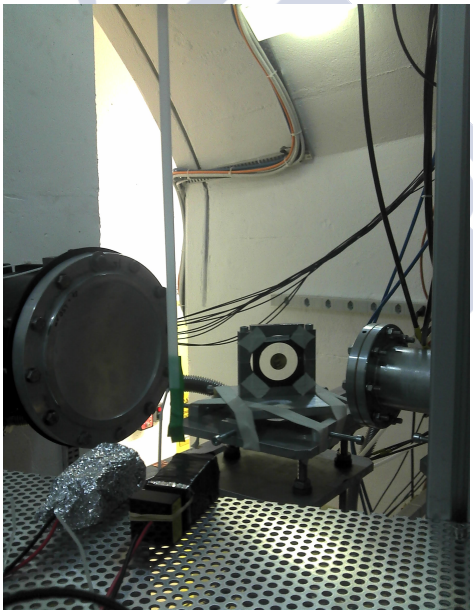

Figure 4.10.: Neutron capture set-up at EAR1

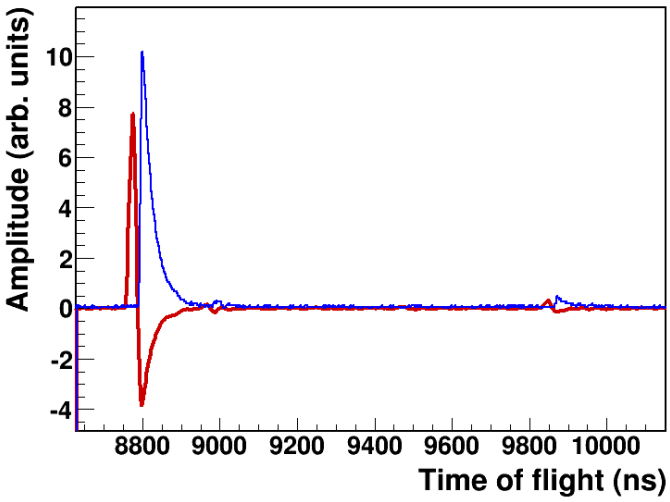

(a)

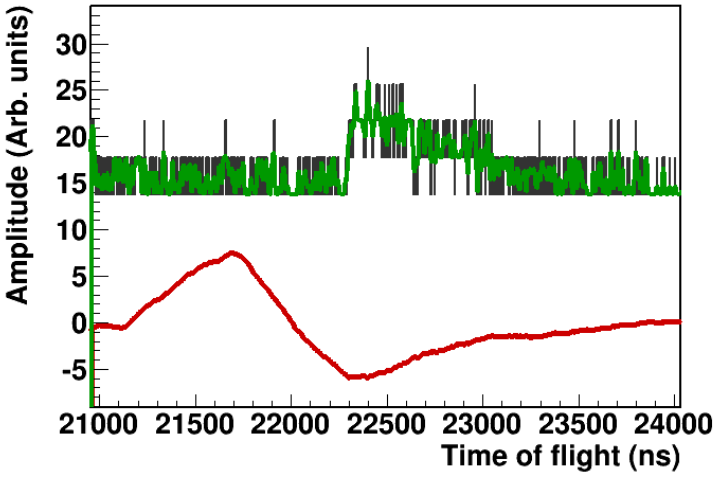

(b)

Figure 4.11.: Trapezoidal-filtered signals for $CeBr_3$-PMT and CsI(Na)-PMT. In (a), the blue line corresponds to a couple of the events from $CeBr_3$-PMT registered by the n_TOF DAQ. The red line is the filtered signal, showing a constant time offset. In (b), an original signal from CsI(Na)-PMT (black line) shows a baseline shift. The green line is the smoothed original signal showing a better shape. The red line corresponds to the trapezoidal-filtered signal. Note the baseline shift correction.

Acquisition Sampling Rate	500 MS/s	
Scintillator detector	$CeBr_3$-PMT	CsI(Na)-PMT
L (ns)	16	560
G (ns)	4	56
Delay time (ns)	12	1160

Table 4.1.: Trapezoidal filter parameters for $CeBr_3$-PMT and CsI(Na)-PMT detectors used in promt γ-rays mesurements at n_TOF.

4.2.2. Data analysis

The capture spectrum has been calculated through the time difference of the γ-ray impact on the scintillator detector and the time of the γ-flash as a reference time. No PKUP correction has been carried out in this calculation. The neutron energy selected for this study ranges from 0 to 100 eV. To find the time-of-flight of the signal produced by the γ-rays a trapezoidal filter was used. These filters, one dedicated to the $CeBr_3$-PMT signals, one dedicated to CsI(Na)-PMT signals, improve the signals making them higher, better shaped and baseline restored than the original ones. Two examples of filtered signals can be seen in Fig. 4.11. In (a), the blue line corresponds to a couple of the original signal from $CeBr_3$-PMT with different amplitude registered by the n_TOF acquisition system and scaled for comparison. The red line is the filtered signal. In (b), a original signal from CsI(Na)-PMT (black line) shows a baseline shift. The green line is the smoothed original signal to show a better shape. The red line corresponds to the filtered signal, where the baseline shift has been corrected. As it is observed in both filters, a delay time is present in the filtered signals due to the filtered processes. Such effect is so relevant and must be corrected in order to obtained an accurate measurement of the time-of-flight. The filter parameters used in these cases are shown in Table 4.1.

4.2.3. Capture results

The spectra obtained for the two samples and two detectors are shown in Figs. 4.12 and 4.13 where their shapes are compared with the ENDFB-VII.1 evaluated library in the case of ^{197}Au(n,γ) and CENDL-3.1 evaluated

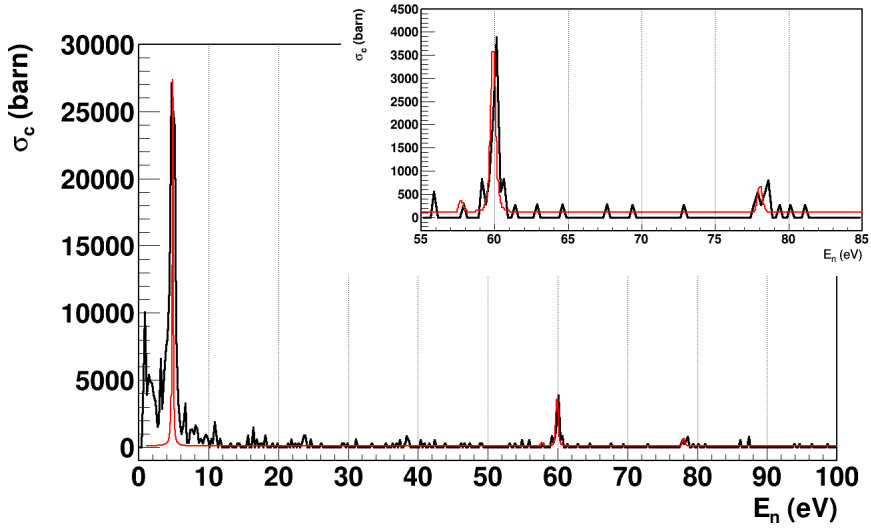

(a)

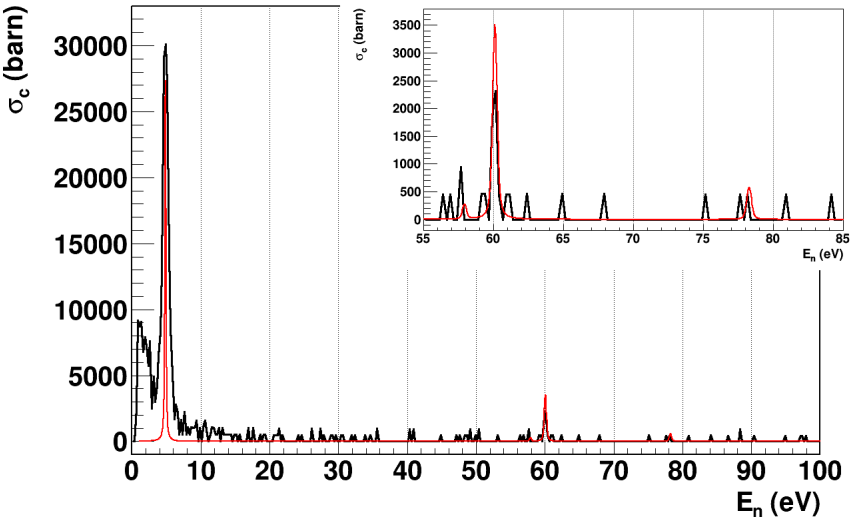

(b)

Figure 4.12.: ^{197}Au neutron capture cross section for ^{197}Au. Red line: ENDF/B-VII.1 evaluation. Black line: measured scaled for comparison with the evaluation. (a) corresponds to $CeBr_3$-PMT measurements, (b) corresponds to CsI(Na)-PMT measurements.

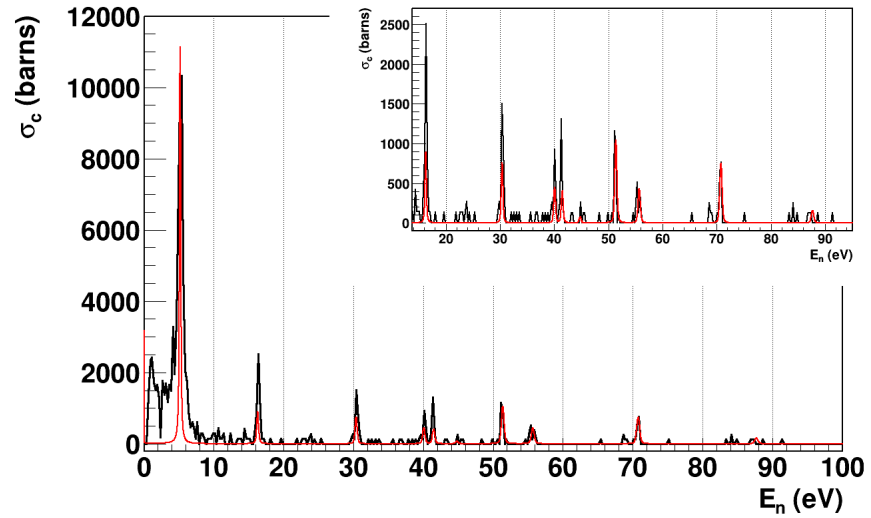

(a)

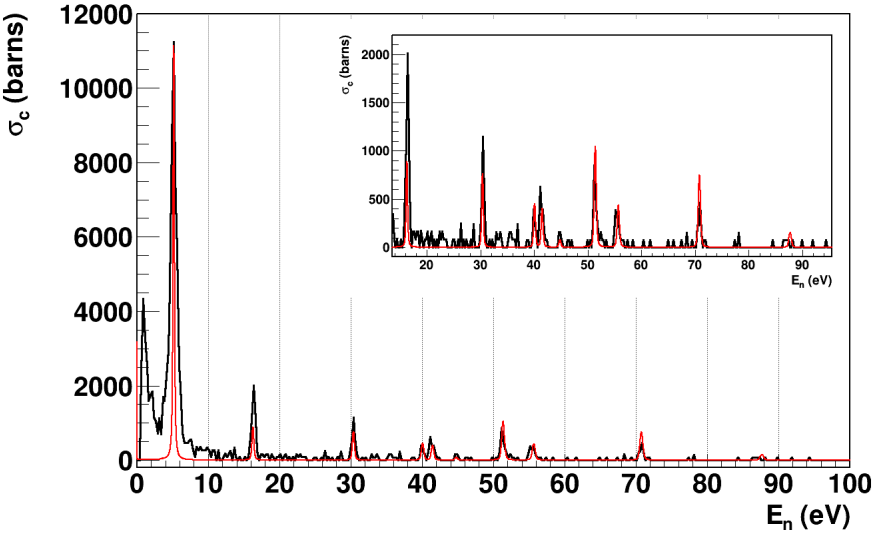

(b)

Figure 4.13.: ^{nat}Ag neutron capture cross section for ^{197}Au. Red line: CENDL-3.1 evaluation. Black line: measured scaled for comparison with the evaluation. (a) corresponds to $CeBr_3$-PMT measurements, (b) corresponds to CsI(Na)-PMT measurements.

library in the case of ^{nat}Ag (n,γ). The energy spectra was corrected by the neutron flux for the 2011 campaing.

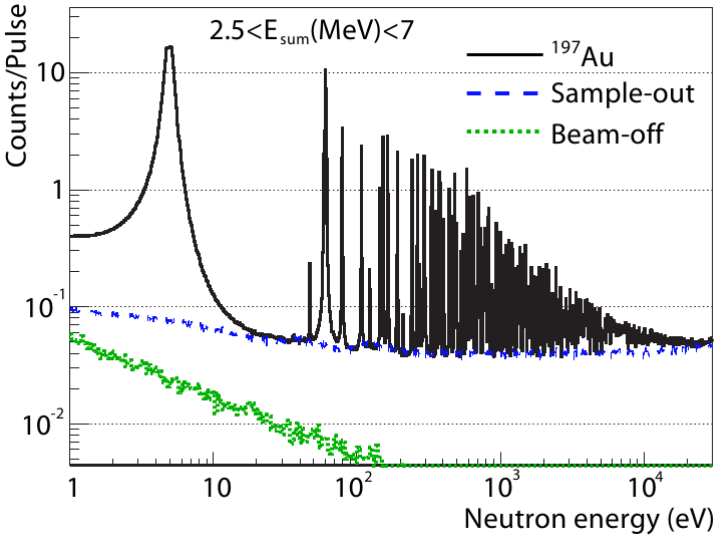

Figure 4.14.: Measured counting rate distributions corresponding to the ^{197}Au and the dedicated background measurements. Fig. taken from Ref. [13].

A background contribution is observed in every measurement at the lower region. As it is shown in Fig. 4.14 (see Ref. [13]), the contribution is mainly due to the fact of the activity of different materials in the experimental area, due to the in-beam γ-rays of of 2.2MeV from the ^{1}H(n,γ) reaction produced in the moderator material surrounding the spallation target see Ref. [74]. In any case, the rate between the resonances below 5 eV and the background contribution shows that the neutron capture reaction contribution is greater than the background. It is worth noting the green line in Fig. 4.14, showing how the beam-off noise raises at the lower energies; this is because the lower energies correspond to the larger time bins.

For the shake of comparison of the measured spectra of the ^{197}Au and ^{nat}Ag fand the above mentioned evaluated libraries, it were normalised to

the maximum value obtained by the largest resonance.

These capture measurements allow to tune-up the scintillator's setup, and its results confirm that the radiation detectors and the analysis techniques used in this work, are suited to measure the prompt γ-rays emitted from (n,γ) reactions.

4.3. Prompt γ rays from U5(n,f) reaction

After the capture measurements, some tentative measurements were done on the ^{235}U(n,f) reaction, where an important portion of the energy released, around 7%, is due to the prompt γ-rays. The request of a better characterisation of the fission γ yields have been formulated in the Nuclear Data High Priority Request List of the Nuclear Energy Agency since the required accuracy, a 7.5% [75], was not achieved in previous measurements done in 1970's [76, 77].

A better understanding of the fission process and a continuous development of nuclear technologies demand a detailed and precise study of the fission processes, mainly the yield of fission fragments, FF, and both the neutrons and the γ rays emitted during the fission process toward stability. The deeper study of the neutron emission during the fission process encourage, however, the study of the prompt γ-rays that implies uncertainties on the nuclear data needed for the design of new fast reactors. For example, the local heating can be mispredicted by up to 30% even in well known power reactors [78].

4.3.1. Experimental setup

During the 2012 campaign, two scintillators detectors, already described in the previous Chapters, were placed in parallel to the PPAC detectors (above described in Section 4.1), using the configuration showed in Fig. 4.15 . The two scintillator detectors stood near PPAC 7 and PPAC 8, where one ^{235}U target were in between, in order to get measured the prompt γ-rays resulting from de fission process, in coincidence with the PPAC pulses, that show to be faster than those from the scintillators, as

it is noticeable in Fig. 4.8. Thus, a method for coincidences, based on a specific trigger routine, has been developed. The main goal was observing the γ-rays from the resonances at low neutron energies.

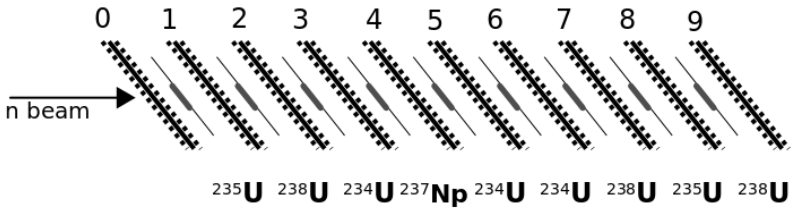

Figure 4.15.: PPAC targets

Nine targets and ten PPACs are contained in the same tight enclosure and so the challenge was to identify the origin of each fission event, with its corresponding time stamp. The coincidences were found as follows: the γ-flash time was obtained as a initial reference for both the scintillators crystals and for the PPACs anodes labeled as 7 and 8. Two time windows were then defined in order to find out the signal coincidences between the anodes and the scintillator detectors. Two different studies were performed: on the one hand, the study of timing signal coincidences between the $CeBr_3$-PMT and the PPAC anodes labelled and on the other hand, the study of the coincidences between the CsI(Na)-PMT and the anodes 7 and 8.

4.3.2. Data analysis

Coincidence trigger Firstly, the coincidence trigger used for such purpose is here explained.

In order to get the coincident measurements between both detectors, an algorithm was created that identifies all possible simultaneous signals. The main idea was to use binary arrays that can be identified with each PPAC and crystal detector. That simplifies later the analysis, chosing any coincidence condition just by applying a simple binary mask. For example, when wanted to identify coincident signals between PPAC #8 and the crystal the condition (mask) applied to the bit array would be

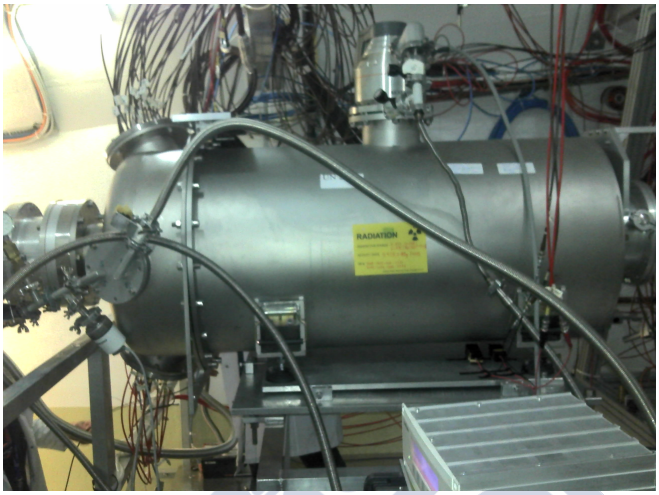

(a)

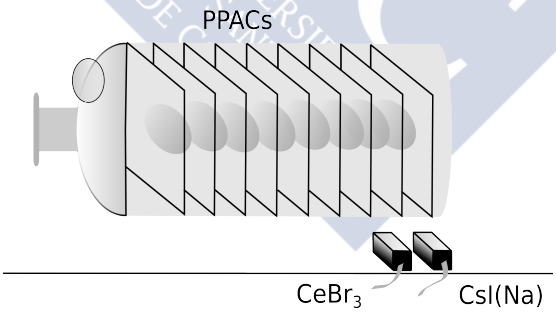

(b)

Figure 4.16.: Set up PPACs, scintillators

as follows: `if( num & (1«8) == 1 )`. The logical & bitwise AND operator checks for the value of the eighth bit stored in `num`, that is the bit array created to tag the signals and store them as an integer value. In case of multi-coincidence events, more complex structures can be required. For instance, the coincidence between the crystal, and the 7^{th} and 8^{th} PPAC detector can be expressed as follows:

$$if\ (num\ \&\ (1 << 8)\ ==\ 1\ \&\&\ num\ \&\ (1 << 7)\ ==\ 1), \tag{4.6}$$

or even simpler:

$$if\ (num\ \&\ (1 << 8 + 1 << 7)\ ==\ 1). \tag{4.7}$$

Furthermore, where anti-coincidence with other detectors are relevant, it can be easily selected by asking the specific bits to be explicitly zero.

The code works as follows, first, the measured times and the trees with data from different detectors are synchronized and calibrated. Then, the algorithm loops over the sorted by time events and in case it finds two concurrent signals within a time window of 50 ns it stores the time, the corresponding neutron energy, the velocity and other useful information as the amplitude, area and width of the signal for further analysis. The identification number of the PPAC detector is stored into a binary list for that event as true. Then a subsequent loop is done over the remaining detectors in order to identify other possible positive signals. These coincident measurements are added to the binary list as true values as well, conforming the final value of `num` to be stored in the tree. In parallel, also all the coincidence signals between the PPAC detectors are stored into another binary array. The schematic algorithm design is shown in Fig.4.19.

Analysis windows t_{ppac} is the time stamp when a pulse on the anode of the PPACs is detected. The routine used to analyse and store the data coming from the scintillator detector, routines used in Section for (n,γ) reactions 4.2, differs from the routine applied in the PPACs case as it was explained before. The coincidences are calculated as follows:

1. Searching coincidence between the crystal and one of the 10 anodes

is get by the condition:

$$|t_{Scin} - t_{Anode}| \; < \; timing\ window\ (ns) \tag{4.8}$$

where the timing window is different for $CeBr_3$-PMT and CsI(Na)-PMT. Once such coincidence has been found, a flag is stored in the Tree in order to avoid a repetition of the coincidence in the second search of the coincidence, as was explained in above paragraph.

2. A new coincidence search between the time of the signal anode previously found in point 1, is carried out. The timing distance between both time stamps is 25 ns.

$$|t_{Anode} - t_{Anode'}| < 25\ ns \tag{4.9}$$

A second flag indicates that the second coincidence has been found.

3. The parameters characterising the pulses, both the anodes of the PPACs and the scintillator detectors are stored in a new Tree.

The timing windows were find out using an iterative method from the low time window related to the time width of the PPACs signals (FHWM) and increasing it until the background is appearing in the neutron energy spectrum. The timing distribution of time difference for the average time of anodes 7 and 6 for both $CeBr_3$-PMT and CsI(Na)-PMT are shown in Fig.4.20. Both distribution shows non symmetrical timing windows. In addition, Figs. 4.17 shows this study for a set of timing windows taking into account the number of events registered as true coincidences. Two different contribution are observed. The flatter ones (black points) were fitted to a linear function and subtracted from the original plot giving as a result the plot formed by the blue dots. Considering the previously exposed, the timing window value chosen for the $CeBr_3$-PMT case is a symmetrical window, |50| ns, and a non symmetrical from -100 to 300 ns in the CsI(Na)-PMT.

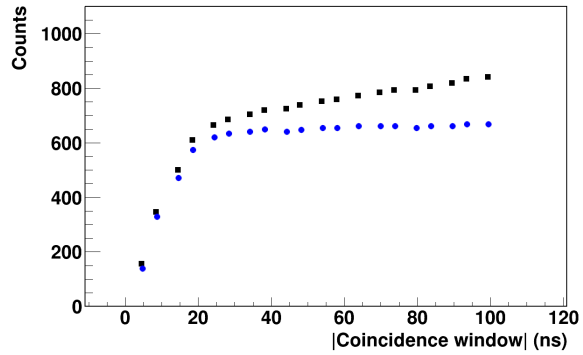

(a)

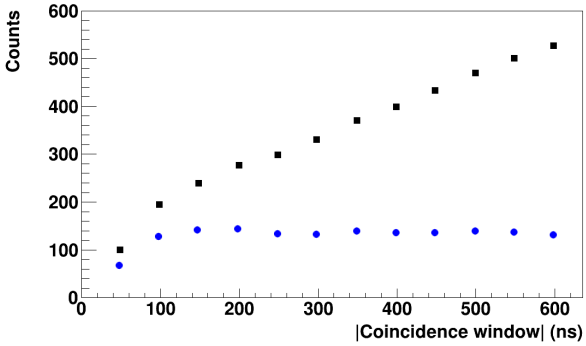

(b)

Figure 4.17.: Plateaus for $CeBr_3$-PMT (a) and CsI(Na)-PMT (b). The statistics for each timing window is shows (black dots). The flatter contribution was subtracted by fitting a linear function. The result is plotted (blue dots).

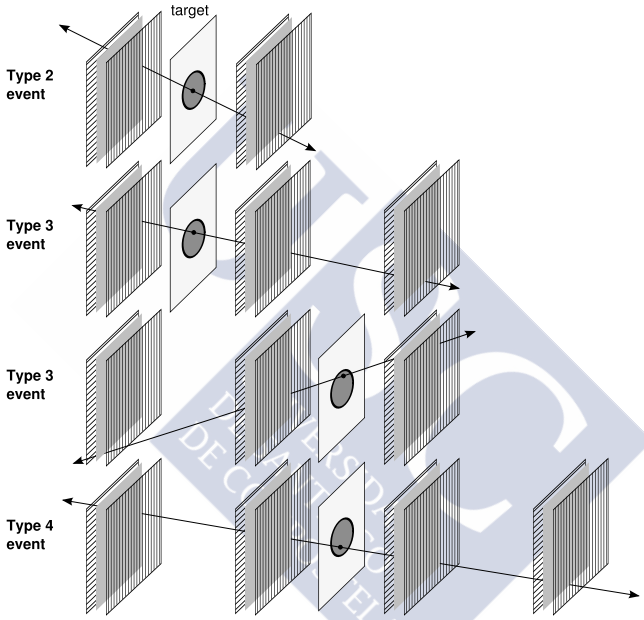

Figure 4.18.: Types of events that happen in PPACs detectors. Type 3 and 4 must be remove from the analysis to avoid the distorted measurements. [14]

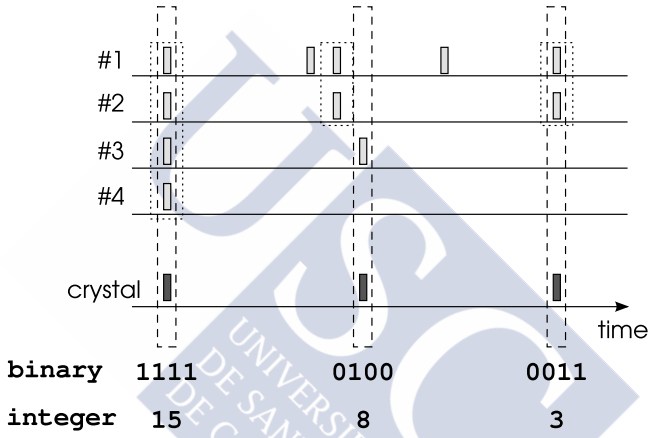

Figure 4.19.: Schematic representation of the coincidence algorithm. The dashed lines represent coincident signals between the crystal and the PPAC detectors. The dotted lines show the coincidence among PPACs. Each coincident measurement is stored using a specific integer number. This value later can be used to select via a binary mask one specific coincidence condition [14].

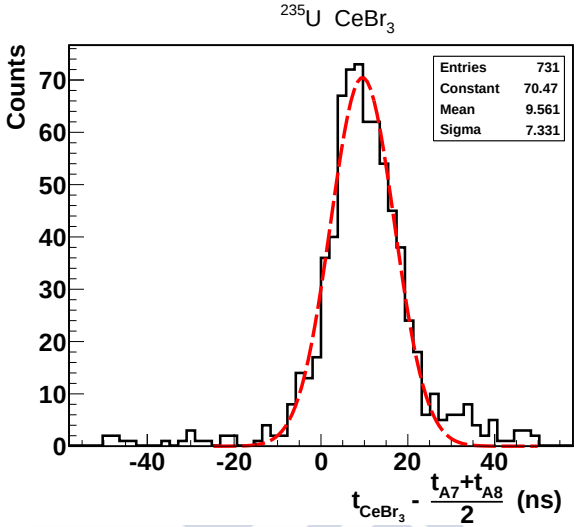

(a)

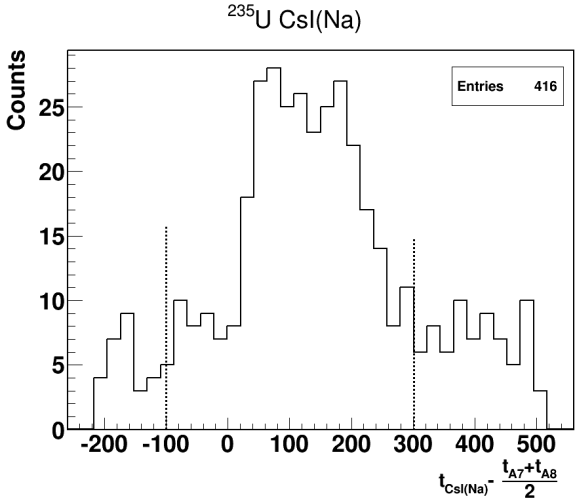

(b)

Figure 4.20.: Distribution of the time differences between a PPAC anode and a scintillator detector for $CeBr_3$-PMT (a) and CsI(Na)-PMT (b).

Contribution from other reactions. When analysing the coincidences for the ^{235}U(n,f) reaction, a high quantity of events are also detected as a single coincidences or accidental ones. Excluding the events tagged for such reaction, the events are plotted in a histogram for the $CeBr_3$-PMT case. In Fig. 4.21 above, a clear resonant signal is observed above the background. This background is removed using a potential fitting function ($y = A \times E_n^B$). Once it is removed, the contribution clearest observed corresponds to a resonance at $E_n \simeq 5.17$ eV. Studying the possible contributions off the targets placed in between the PPAC detectors, it is concluded that the contribution comes from the ^{234}U(n,γ) reaction, whose cross section shows a large resonance at that energy. The cross section value corresponds to 22277.7 barns, according to the ENDF/B-VII.1 evaluation library.

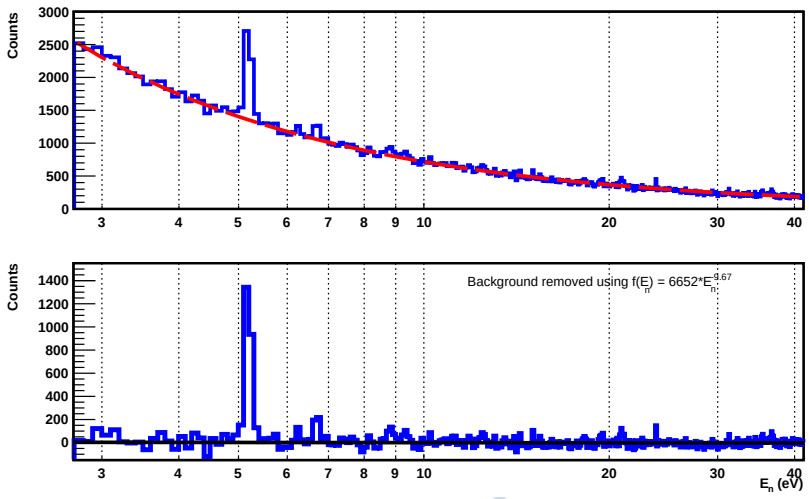

Figure 4.21.: ^{234}U(n,γ) contribution.

The spectra energy were corrected by the neutron flux on the 2011 campaing and the data were scaled in order to the compare with the evaluated function of the ^{235}U(n,f) cross-section from ENDF/B-VII.1 (Fig. 4.22). Even though the low statistics gotten, due to the very reduced beam time available, the good results confirm that the spectra can be measured using these kind of small and fast scintillator detectors. The promising results, even tough very preliminary, allow to keep open the way to further exper-

iments aiming to cope with the requests of deeper understanding of the prompt-gamma produced along the fission process.

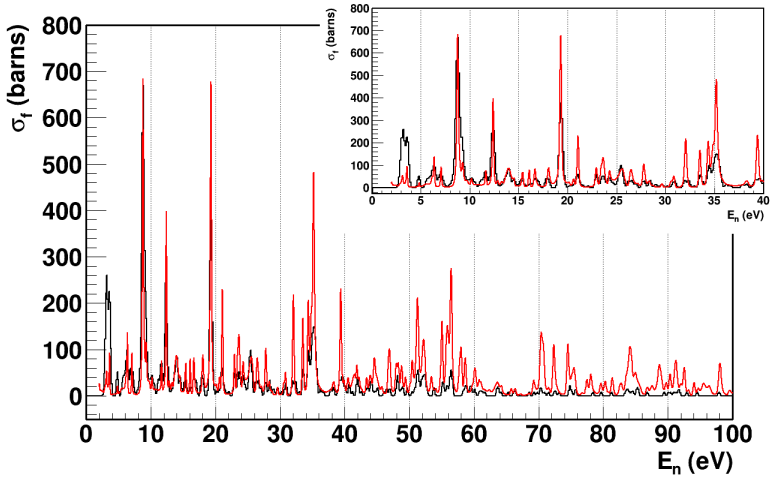

(a)

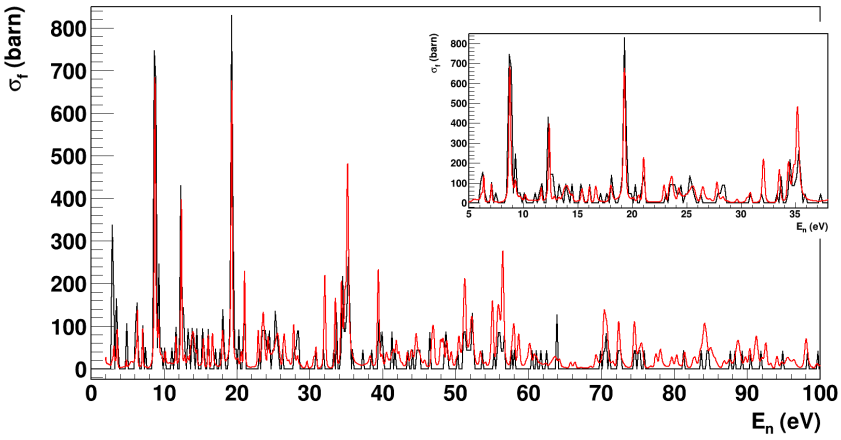

(b)

Figure 4.22.: γ fission neutron energy

4.4. γ-flash study

4.4.1. What γ-flash means?

During the spallation process, when protons of 20 GeV/c impinges on the lead target, a huge amount of radiation and both neutral and charged particles are produced as result of both hadronic and electromagnetic reactions at the very beginning of the process. These spallation products travel along the beam line interacting with its components producing new radiation and particles disturbing the neutron beam produced. At n_TOF experiment, the contribution of these particles and radiation to the detectors placed in the experimental areas is an inconvenient, since it blinds the detectors used for an specific lapse of time that depends, among others, on their nature and their associated electronics, preventing the measure of the most energetic neutrons released during the spallation process.See Fig. 6.8

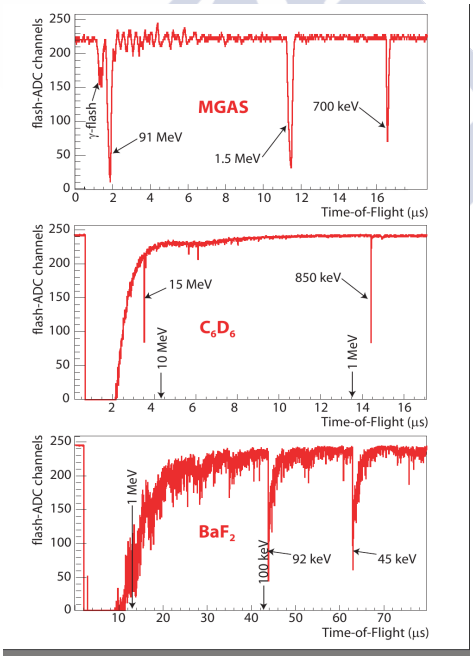

Figure 4.23.: g-flash signals produced

Regarding the γ-production, two components are differentiated: prompt, before TOF < 1 μs , mainly formed by γ-rays produced during the spallation process and delayed, after TOF > 1 μs, formed by γ-rays from radiative neutron capture reactions occurring in both the moderator and the cooling system as well as from material surrounding the spallation target.

The γ-flash refers the prompt radiation background explained above as well as charged particles plus a halo of both charged particles and radiation coming from the interaction of the high-energy neutrons and γ-rays with the second collimator showed in the beam line.

For EAR1:

Reduction of the section of the beam pipe passing through the concrete wall (performed in 2014).

Taking into account considerations to reduced the background, the so-called γ-flash is observed in both EARs.

The γ-flash is taking as a time stamp reference for the ToF since it is the first signal detected by the acquisition frame for each proton bunch impinging on the spallation target, being the signal provided by the PKUP the trigger to start the acquisition system for each channel.

In this work, the detectors $CeBr_3$-PMT, CsI(Na)-PMT and CeF_3_L50-PMT were used to characterised the γ-flash using sensitive detectors to γ radiation and charged particles, whose reduced active volumes make them appropriated for counting and timing measurements in this environment with such a so high background but not for energy deposition because its low peak to Compton ratio, as it was explained in Chapter 2

4.4.2. γ-flash measurements

$CeBr_3$-PMT and CsI(Na)-PMT were placed to measure the g-flash and find out its characteristics when it arrives to an inorganic scintillator crystal.

The γ-flash is the first signal, in timing terms, as it states above, that is registered by the detectors. The γ-flash is taking as a time stamp reference for the ToF since it is the first arriving signal at the speed of light. When detected it can be used to accuratelly know the energy of the neutrons

arriving inside the acquisition frame after every proton bunch. These signals are registered by an digitiser module that samples the signals. In this case, the sampling rate for both detectors is 1/2ns, i.e. frecuency.

The γ-flash signal blinds the detectors at the very beginning of the measurement. The lapse of time of the γ-flash depends on the nature of the detector and their associated electronics. Both the $CeBr_3$-PMT and CsI(Na)-PMT shows signal outputs both electrons and gammas and identical signal shapes, that means, that for the initial hypothesis for γ radiation are appropriate to analysis the structure of the γ-flash.

During 2012 n_ ToF campaign, a devoted measurement to study the *gamma*-flash was performed using mainly scintillator detectors. In this chapter, the results and measurements made/performed during that campaign are explained/exposed and showed.

During the 2012 campaign $CeBr_3$-PMT was placed parallel to the concrete wall that separates the Secondary Area to the EAR1 on the right side, following the direction of the neutron beam. The detectors, were placed 20 cm from the centre of the beam. The neutron beam travels along the experimental area through air. The collimator uses was the capture mode: 18 mm diameter.

Regarding the signals/waveforms acquired by such scintillator and comparing them with the acquired waveforms that coming from a γ-ray source, it is obvious that the set of γ-flash signals shown in Fig. X, are wider in terms of timing width as well as higher in terms of amplitude. Besides, it sometimes observe that the γ-flash can present a different waveform structure from bunch to bunch of protons; that observation leads to supposed that the γ-flash is formed by several individual γ rays and charged particles, mainly electrons, that reach/achieve the EAR1 faster than the scintillators are able to resolved in terms of timing, even using a fast system detection like the $CeBr_3$-PMT.

First, a detailed observation of the original pulses, see Fig X shows that:

- Pile-up is present in some pulses
- The width is wider than the γ-ray registered signal a γ-ray source in the oscilloscope.

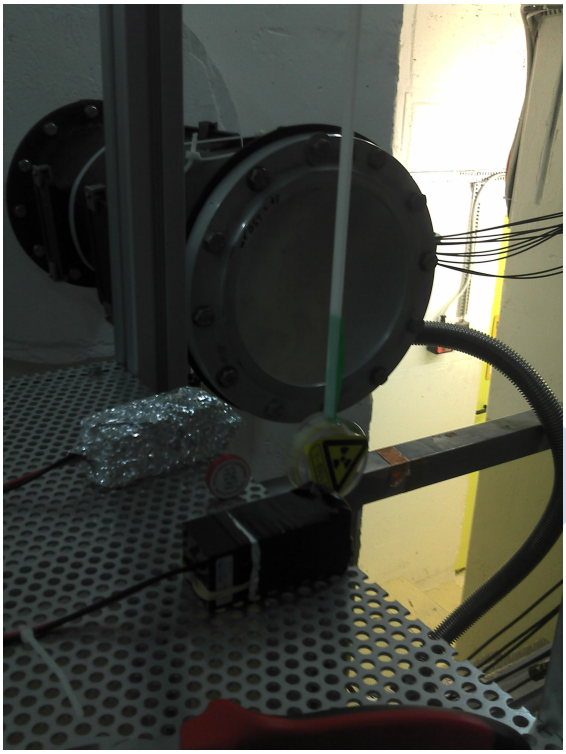

Figure 4.24.: $CeBr_3$-PMT and CsI(Na)-PMT detectors placed at EAR1.

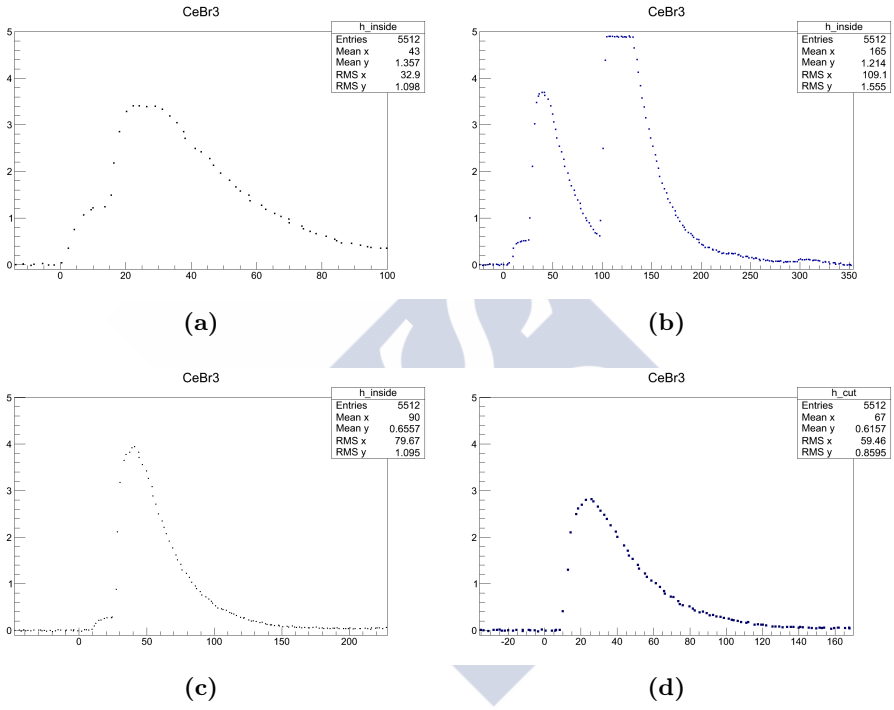

Figure 4.25.: γ-flash pulses from $CeBr_3$-PMT during the 2012 detector test for γ-flash.

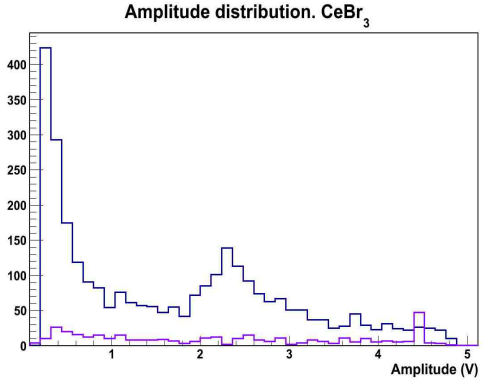

Figure 4.26.: Amplitude distribution of the γ-flash for the first and second pulses.

- The signals shows a different structure/shape from bunch to bunch of protons.
- A fraction of the pulses are larger than the capability of the acq system.
- Signals after the first registered are also produced in some acquisitions.

Therefore, to analyse the γ rays a set of observables have been defined based on the observations of the $CeBr_3$-PMT produced. The observables which will provide information about are related to the amplitude and time of the signals produced. In this case, the pulses are well-defined and no smooth is needed to improved the signal contour, thus, the definition of the observables is accurate through the analysis of the raw waveform. The observables chosen are the initial time of the signal, the maximum amplitude both the first and second pulses registered respectively.

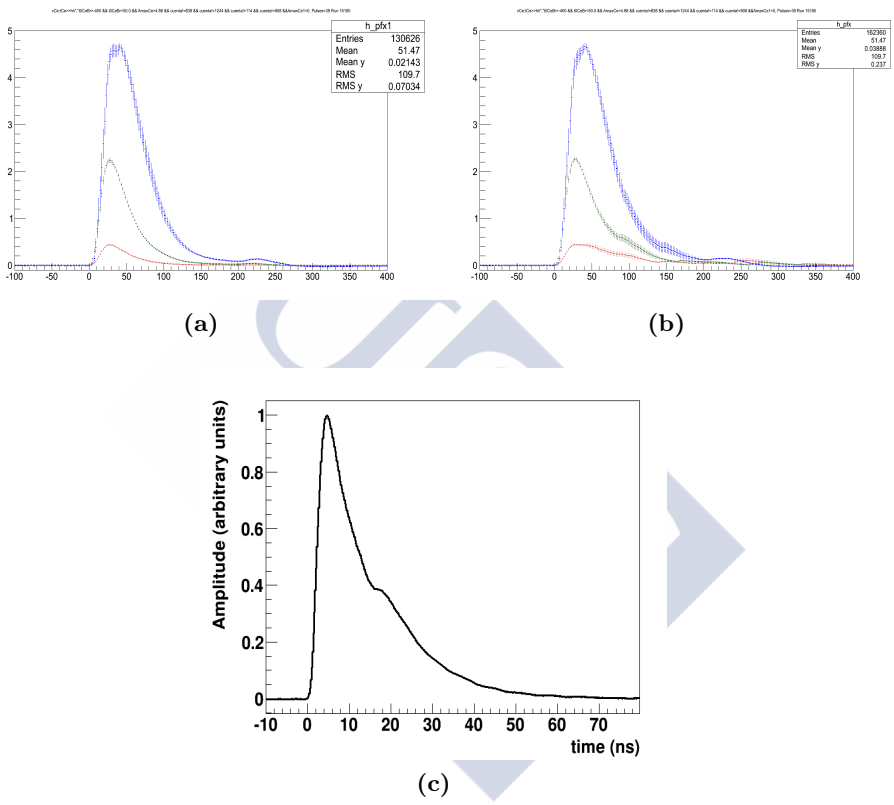

Figure 4.27.: γ-flash profiles for differen deposited energy ranges (related to amplitude distribution in Fig. 4.26) (a) Single pulses profiles. (b) Two or more pulses profiles. (c) γ-ray profile. Note the width of the signal produced by the γ-flash single contribution is larger than the a *gamma*-ray pulse.

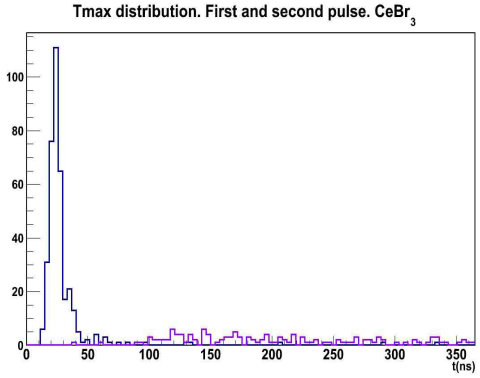

Figure 4.28.: Timing distribution of the γ-flash for the first and second pulses. Three component are distinguished: very prompt, prompt and delayed.

1. The amplitude distribution of the first-arriving pulses shows an accumulation ranging from 0.2 to 5 volts. A 10 % of the firsts signals are saturated. See Fig 4.26
2. Similarly to the second pulses distribution.
3. Concerning timing, three components are distinguished: very prompt, from 0 to 10ns, prompt, from 10 to 50 ns and delayed, >50 ns. See 4.28

Experiments dedicated to fission using PPACs detectors were performed in 2012. In parallel, both $CeBr_3$-PMT and CsI(Na)-PMT were placed at 40 cm far from centre of the beam. As the second collimator system was modified to have a diameter of 80 mm, larger than the one used during the capture detectors test, the γ-flash signals were all saturated in both scintillators. See Figs. 4.29

In the CsI(Na)-PMT case, a rebound is observed after the decay time of the pulses because a fADC problem arising when the input signals exceeds the maximum amplitude allowed. Furthermore, a dead time of the order of 10 μs appears, what is not observed in the no-saturated pulses, Fig. 4.30. In order to overcome this problem, a signal attenuator has been designed. A more detailed description of the attenuator is given in the Apendix D.

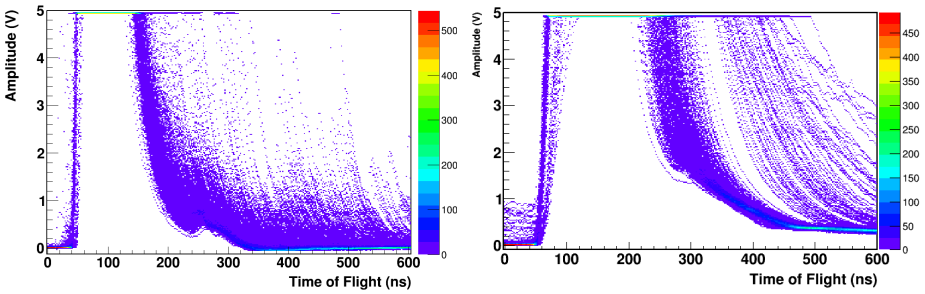

(a) **(b)**

Figure 4.29.: γ-flash pulses from $CeBr_3$-PMT (a) and CsI(Na)-PMT (b) during the 2012 PPAC fission measurements for γ-flash.

The effectiveness of such attenuator can be observed in Fig. 4.31, where the attenuated signals appears without the rebound and saturation problems.

During the 2014 commissioning campaign new measurements were performed in both EARs. Besides the $CeBr_3$-PMT, a very fast plastic scintillator was placed in parallel with the $CeBr_3$-PMT in order to measure the γ-flash in coincidence. The advantages of these set-up is, since the plastic scintillator is very thin and as a consequence its detection efficiency for γ rays is negligible but not for charged particles, that the analysis the data of both detectors provides a qualitative measure and separate of the contribution of the γ rays and charged particles. Besides these detectors, a third one is added to the measured system: a CeF_3_L50-PMT detector,described in Chapter 2. This new set-up measured the γ-flash in EAR2 during the 2014 commissioning. See Fig.4.32

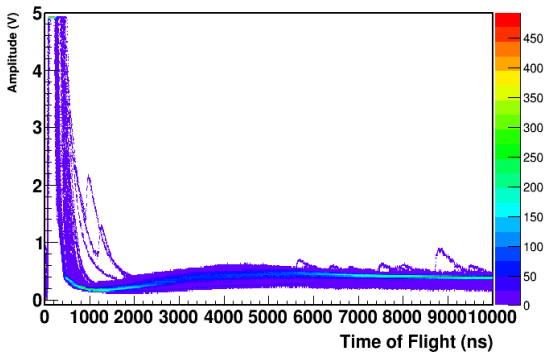

Figure 4.30.: γ-flash pulses from CsI(Na)-PMT. Note the rebound after the decay time of the saturated signals.

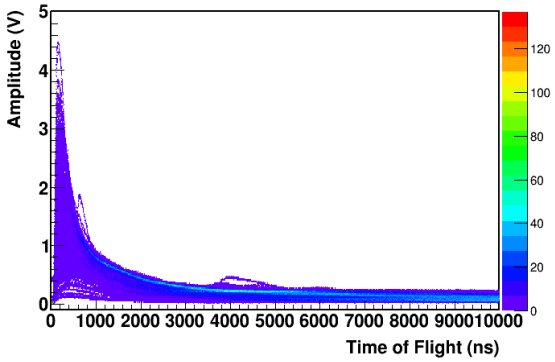

Figure 4.31.: γ-flash attenuated pulses from CsI(Na)-PMT using a Zener diode based attenuator. Note that the rebound after the decay time of signals is removed.

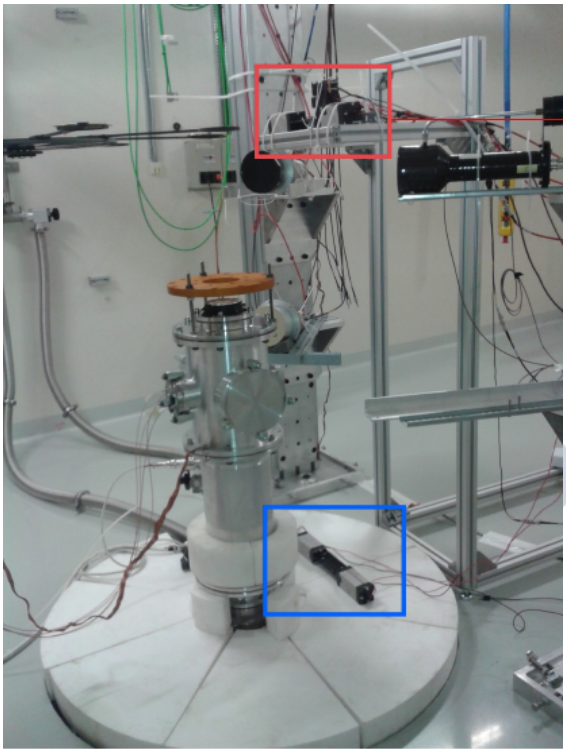

Figure 4.32.: Setup for γ-flash in EAR2, showing the detectors used.

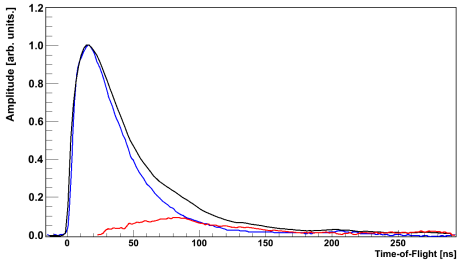

(a)

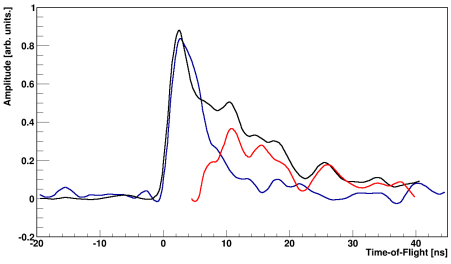

(b)

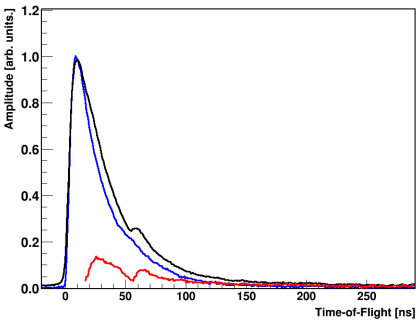

(c)

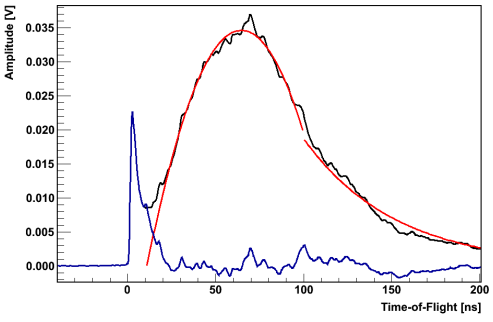

(d)

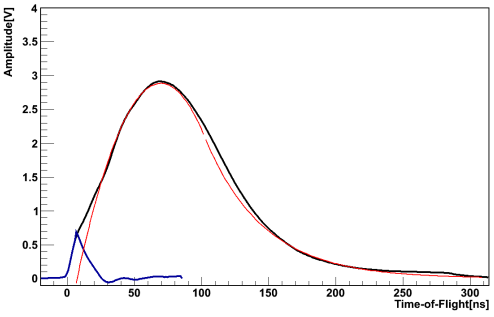

(e)

Figure 4.33.: Signal profiles

4.4.2.1. Comparison with other detectors

Two detectors with low γ-rays efficiency from different nature have been also tested in both experimental areas. A solid-state detector, a CVD diamond from TUW and a gaseouse Parallel Plate Avalanche Chamber from IPNO.

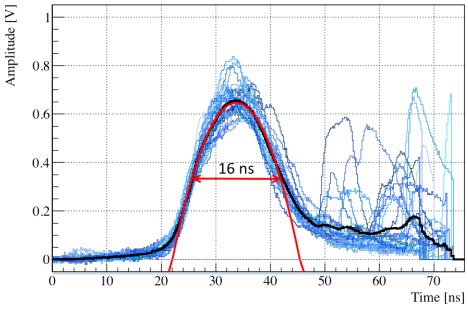

(a)

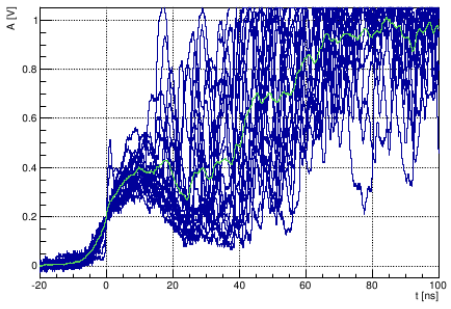

(b)

Figure 4.34.: γ-flash signals from CVD Diamond detector acquired in EAR1 (left) and EAR2 (right). [15]

CVD detector See the with of the signals: 16ns corresponding to the width of the bunch of prontons than impinges on the spallation target.

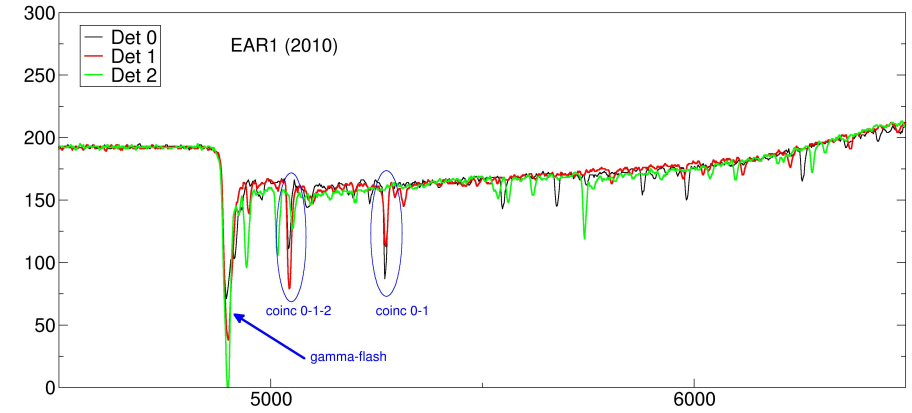

(a)

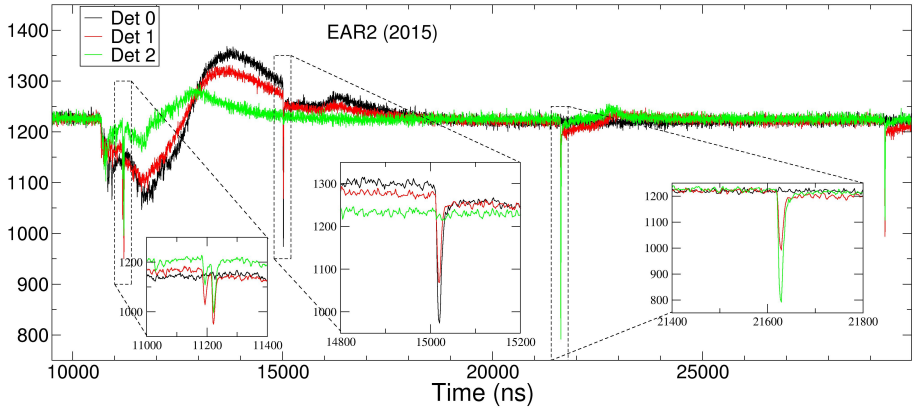

(b)

Figure 4.35.: γ-flash signals from PPAC detector acquired in EAR1, above, and EAR2, below.

PPAC detector

4.4.3. Simulations GEANT4

Using GEANT4 simlation [79], different components of the γ-flash can be distinguished:

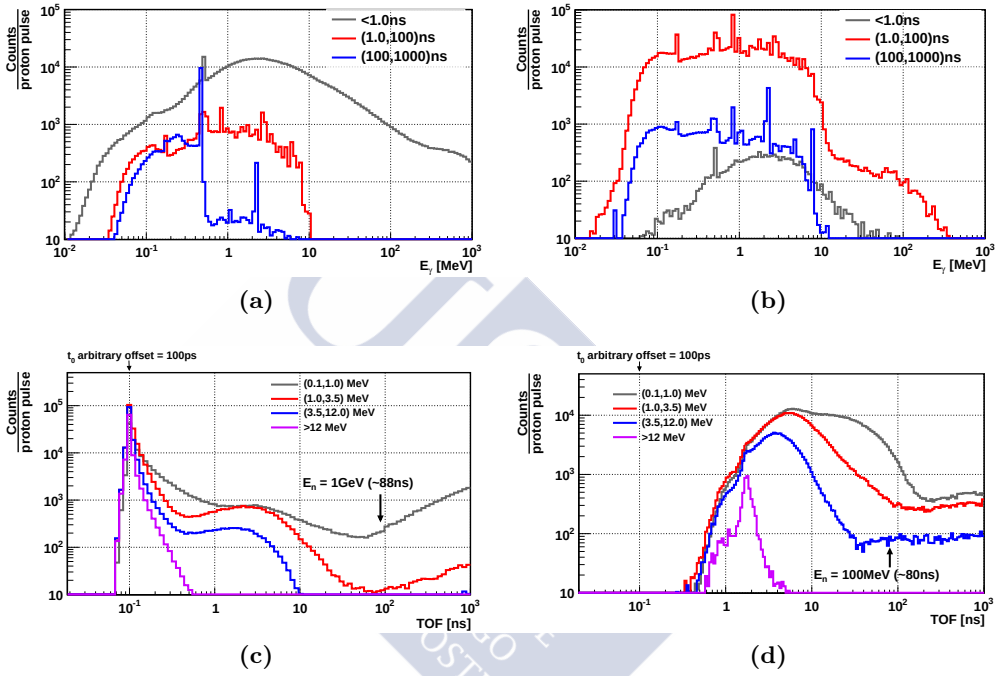

Figure 4.36.: GEANT4 simulations

5. Summary and conclusions

Summary

This thesis work was done in the frame of the study and development of new and better performing detectors carried out in the GENP group of the USC. Part of the acquired skills were then focused on the study of radiation detectors based on fast scintillator inorganic-crystals coupled to different photodetectors such as new photomultiplier tubes and PIN diodes. The γ-flash at the CERN-n_TOF facility brought a unique opportunity to perform tests looking for the limits in the detection of γ-rays and charged particles at very short times, and having as very precise timing the proton pulse impinging at the n_TOF spallation target. Different fast scintillators were tested, coupled to different photosensors, and different signal processing methods have been discussed.

The problems arising when dealing with signals coming from fast scintillator detectors have been discussed in the Chapter 1. Specific solutions, including the development of dedicated electronic circuits, were tested before their further implementation in several experimental set-ups. In particular, simple solutions were found to conditioning the output signal of different detectors, based on fast crystals as $CeBr_3$, CeF_3 and CsI(Na). The output was first analysed at the USC-GENP lab using the traditional spectrospic chain, as well as with flash-ADC acquisition systems, and then at the CERN-n_TOF experimental areas.

The detectors linearity, energy resolution and timing resolution, were firstly measured for γ-rays emitted by different radioactive sources in a range from 121 keV to 4444 keV. Even though the photopeak efficiencies of such small size detectors were reduced, a high detection efficiencies all along at a wide range of incident energies were attained. The design of an attenuator for the output signal from the CsI(Na) scintillator avoid distortion effects caused in the flash-ADC acquisition systems when the

input signal amplitude exceeds its full scale. Moreover, the capability to detect β particles as well as α particles were studied. To do this, methods based on the Pulse Shape Analysis technique have been developed looking for information on the kind of the incident radiation through detectors. By means of the observables defined for such signals, PSA has been performed to discriminate α particles from γ-rays and its modest success is discussed. The comparisons between the pulse shape analysis of the γ-rays and MIPs -bothβ particles and cosmic-rays- show that using these crystals does not allow a good identification of the kind of these impinging radiation.

One of the goals of this work was the search for scintillator detectors fast enough to allow detection of γ-rays and charged particles at very short time from the so-called γ-flash. The presence in the n_TOF experimental areas of such a so strong prompt signal produced in the spallation target, represents the biggest limitation in the upper energy limit that can be reached in measurements at n_TOF experiments so far.

Conclusions

The main conclusions of this work may be summarised as follows:

- For these relatively small crystals, high efficiency for γ-rays counting and accurate measurement of the deposited energy for β particles have been found, in accordance with the results that have been obtained by simulations using the EnsarRoot framework.
- The reaction (n,γ) for isotopes ^{107}Ag, ^{109}Ag and ^{197}Au, were measured in a range of neutron energies from 1 to 100 eV by the Time-Of-Flight technique. Despite the low statistics available, due to very reduced acceptance angle defined by the small size of the detectors, the usefulness of this technique was proven to detect prompt γ-rays from capture reactions in a noisy environment.
- The prompt γ-rays emitted from reaction ^{235}U(n,f) was measured in parallel to the PPACs reaction chamber, in a range of neutron energies from 1 to 100 eV by means of the coincidence method. The overall statistics was low but, nevertheless, the robustness of the coincidence method using the specifically developed software routines

was proven, allowing to select the γ-rays from a tagged fission reaction.

- Using the detectors developed in this work, the n_TOF γ-flash have been characterised in both experimental areas, EAR1 and EAR2. It can be deduced that the main contribution is coming from the γ-rays originated after the spallation process produced by the impinging protons on the lead target, followed by its conversion in high-energy forward focused e^+-e^- pairs. Furthermore, the results were compared with different solid state and gaseous detectors used in the n_TOF experiment, as well as with the simulations performed by other n_TOF groups, confirming such hypothesis.

USC
UNIVERSIDADE
DE SANTIAGO
DE COMPOSTELA

6. Resumen en castellano

La investigación en Físca Nuclear experimental necesita experimentos que requieren detectores específicos cuya precisión, en términos de resolución en energía y resolución temporal, sea la mejor posible. Debido a esto, es necesario desarrollar nuevos detectores al mismo tiempo que los continuos avances en los materiales y técnicas usados para la detección de núcleos ligeros, partículas cargadas y radiación γ producidos en procesos nucleares. La mayoría de estos detectores están basados en materiales centelleadores, que pueden ser tanto plásticos (órganicos) como cristales inorgánicos. El objetivo de este trabajo consiste en la caracterización de diferentes detectores nucleares basados en cristales centelleadores y su posible uso en la detección de radiación γ proveniente de procesos nucleares tales como la fisión nuclear la captura neutrónica.

A lo largo de la segunda mitad del siglo XX se han relizado numerosos estudios sobre detectores centelleadores. En la última década, la mejora de los procesos de fabricación de los cristales y el desarrollo de fotodetectores ha dado lugar a mejoras en medidas de calorimetría, resolución en energía, identificación de partículas y resolución temporal [18]. En este trabajo se han utilizado los siguientes detectores de radiación: cristales inorgánicos de bromuro de cerio ($CeBr_3$), yoduro de cesio dopado con sodio (CsI(Na)) y fluoruro de cerio (CeF_3), cuyas principales caracterísitcas se encuentran las Tablas 6.1 y 6.2, acoplados a diferentes fotodetectores, como nuevos tubos fotomultiplicadores y diodos PIN. Además de esto, se ha hecho uso de plásticos centelleadores muy rápidos para tratar de discriminar partículas cargadas de radiación γ.

Estos detectores han sido probados tanto en el laboratorio de desarrollo de detectores situado en la Universidad de Santiago de Compostela así como en la instalación nTOF en el Consejo Europeo para la Investigación Nuclear, CERN, situado en Ginebra (Suiza).

El uso de estos detectores rápidos implica una serie de problemas a la

Cristal centelleador	CsI(Na)	$CeBr_3$	CeF_3
Densidad (g/cm^3)	4.51	5.20	6.16
Constante de bajada, τ (ns)	630	18-20	5,27
Pico de emisión, λ (nm)	420	380	300,340
L.Y. (ph/keV)	35-42	45-60	4.3
Índice de refracción, n	1.84	2.09	1.62
Estructura cristalina	Cúbica	Hexagonal	Hexagonal
Z_{eff}	54	45.9	53
Higroscopicidad	Sí	Sí	No

Cuadro 6.1.: Principales caracterísiticas de los cristales centelleadores usados en este trabajo: $CeBr_3$, CsI(Na) y CeF_3.

Cristales centelleadores	$CeBr_3$	CsI(Na)	CeF_3_L50	CeF_3_L40
Dimensiones(mm^3)	18x18x25	18x18x25	18x18x50	18x18x40
Acabado	Pulido	Pulido	No pulido	Pulido
Encapsulado por	Scionix	USC	USC	USC
Fabricante	Scionix	MolTech	MolTech	MolTech

Cuadro 6.2.: Dimensiones, acabado, encapsulamiento e información de fabricación de los cristales utilizados en este trabajo.

hora de obtener la información contenida en las señales que se han producido por la interacción de partículas cargadas o radiación gamma. Para resolver estos problemas, se han propuesto una serie de soluciones que consistirían, por un lado, en el desarrollo de circuitos electrónicos y por otro, el uso uso de filtros digitales para el posterior análisis de la señales adquiridas y digitalizadas por parte de sistemas de adsición tales como osciloscopios o módulos conversores analógico-digitales usuados comúnmente en instalaciones de experimentos dedicados a la Física Nuclear.

Dentro de las soluciones relacionadas con los circuitos electrónicos, se encuentra el desarrollo de una tarjeta electrónica basada en la combinación de filtros activos. Esta tarjeta actúa sobre la señal de los detectores centelleadores como amplificador y modificador de la forma de la señal, adaptándola así a sistemas de espectroscopía, es decir, a módulos amplificadores espectroscópicos que forman parte de la tradicional cadena espectroscópica, ver Fig. 6.2, utilizada comúnmente para averiguar tanto la respuesta lineal del detector como la resolución en energía. Esta tarjeta ha sido específicamente diseñada en dos versiones diferentes: una para el detector $CeBr_3$ y otra para el CsI(Na). El uso de esta tarjeta se ha probado utilzando una cadena tradicional espectroscópica resolviendo los problemas de no linealidad y resolución en energía expuestos con anterioridad y se muestran los resultados en las Figs. 6.1.

Los cristales centelleadores tales como el bromuro de lantano y $CeBr_3$ presentan una emisión de luz muy elevada, denominado por sus siglas en inglés, L.Y.) cuando las partículas cargadas o la radiación gamma interactúan con ellos. Esto supone un problema en las primeras etapas de multiplicación de los tubos fotomultplicadores, que pueden llegar a saturalos. PAra solventar este problema, se ha desarrollado un circuito divisor de voltaje que modifica el zócalo de alimentación proporcionado por el fabricante, Hamamatsu, a través de elementos pasivos, como resistencias, colocados en paralelo al zócalo original.

Los sistemas de adquisición flash-ADC suelen presentar problemas cuando las señales de entrada superan el rango de amplitud permitido por estos módulos. Un valor característico de este rango suele ser pm 5 V. En algunos casos específicos, la señales proporcionadas por los detectores centelleadores pueden superar estos límites lo que se traduce en efectos no deseados

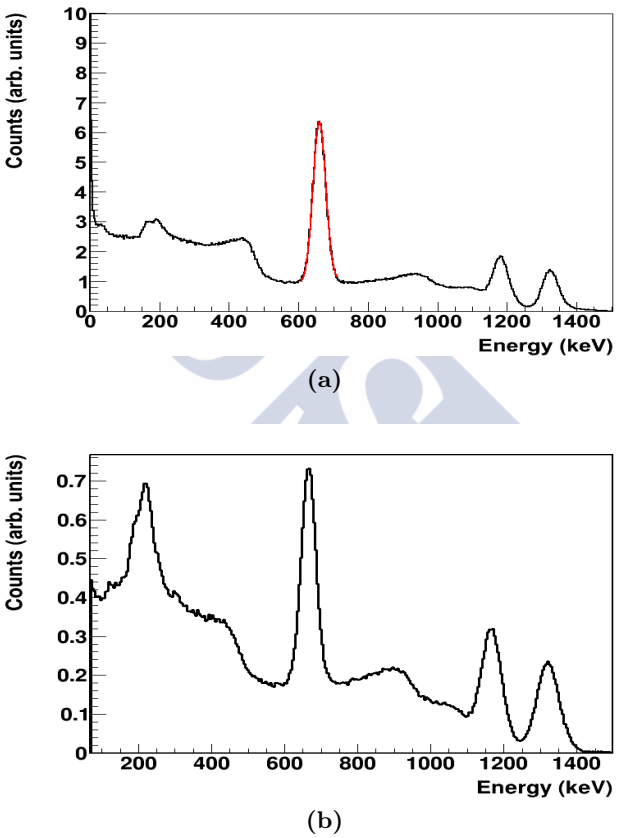

Figura 6.1.: Espectros adquiridos de ^{137}Cs+^{60}Co usando las tarjetas electrónicas *stretcher* para la adaptación de las señales del $CeBr_3$, (a), y el CsI(Na) (b). Los problemas de no-linealidad han sido resueltos.

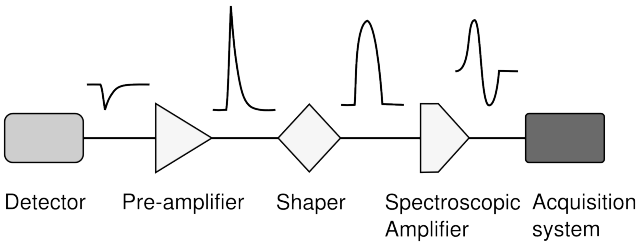

Figura 6.2.: Típica cadena de medida para la medida de la energía depositada, llamada *cadena espectroscópica.* Está compuesta por cinco etapas: el sistema de detección, una etapa preamplificadora, un amplificador que adapta la forma de la señal, el amplificador espectroscópico y por último, el sistema de adquisición. La evolución y modificación de la señal se representa esquemáticamente en la línea.

en las señales digitalizadas. Para el detector CsI(Na) se ha desarrollado y probado un atenuador basado en diosdos Zener. Al igual que en los dos anteriores casos, el diseño ha sido probado en condiciones reales con resultados óptimos.

Los algoritmos digitales para el análisis de la forma de pulso (PSA) son ampliamente usados para obtener la información contenida en las señales producidas en los detectores de radiación. Los observables de estos filtros son, entre otros, el área del pulso digitalizado, su anchura, amplitud máxima o tiempo de llegada. Además, este tipo de filtros consiguen mejorar problemas como desplazamientos de la línea de base así como el ruido que empeora la calidad de la señal. En este trabajo se han utilizado algoritmos denominados FIR, *Finite Impulse Response*. Estos filtros están bien definidos en el tiempo y no presentan oscilaciones. La señal filtrada de este tipo de filtros consiste en la convolución de la señal de entrada digitalizada con una serie de coeficientes, N, que definen el orden del filtro, como se muestra en la siguiente ecuación:

$$y[n] = \sum_{i=0}^{N} h_i \cdot g[n-i] \tag{6.1}$$

En este trabajo se han utilizado los filtros FIR triangular y trapezoidal.

Para comprender e intrepretar los resultados obtenidos es necesario conocer la interacción entre la radiación γ y las partículas cargadas y la materia así como el proceso de centelleo producido en los materiales que presentan estas caractarísticas, siendo proporcional a la energía depositada por la radiación. Para comprender el funcionamiento de los cristales centelladores se ha relizado una simulación Monte Carlo utilizando el programa informático EnsarROOT [17], para averiguar la respuesta de los cristales centelleadores cuando dos fuentes monocromáticas de radiación γ y partículas β o electrones para diferentes energías que comprende un rangdo de 2 MeV hasta 10 GeV, interaccionan con los cristales de CsI y $CeBr_3$. Los resultados obtenidos muestran que la eficiencia de detección de radiación γ de estos cristales, a pesar de su pequeño tamaño, es de incialmente un 40 % a partir de 2MeV para aumentar hasta un 60 % para energías mayores que 100 MeV. Ver Fig. 6.3 En cuanto a los electrones, se han definido dos observables: el valor medio de la energía doposita da en los cristales, dopositada en los cristales y el valor más probable, moda. De estos resultados se desprende que tanto la media como la moda aumentan de forma paralela hasta un cierto valor a partir del cual la media continúa aumentando mientras que la moda presenta una zona de plateau. El valor donde se produce esta diferencia de tendencia corresponde con la energía crítica de los cristales a partir del cual la emisión de frenado es dominante sobre la interacción por colisiones con los electrones del medio. Ver Fig. 6.4.

La colección de la luz producida en los cristales centelleadores requiere de un envoltorio adecuado que optimice esta recogida luz. Para ello es necesario utilizar los materiales adecuados. Además, atendiendo a la higroscopicidad de los materiales centelleadores, es necesario encapuslarlos para evitar la absorción de la humedad presente en el ambiete por parte de los cristales que empeora la calidad de estos. Los cristales empleados en este trabajo han sido envueltos y encapsulados en el laboratio de desarrollo de detectores de la USC, exceptuando el cristal centelleador de $CeBr_3$ que ha sido encapsulado por el fabricante, Scionix. Para el resto de cristales, se han utilizado dos capas de material ESR de 3M para su envoltorio y un encapsulamiento con una carcasa de aluminio. Uno de los cristales de CeF_3, cuya longitud es 40 mm, ha sido envuelto con dos tipos del envolto-

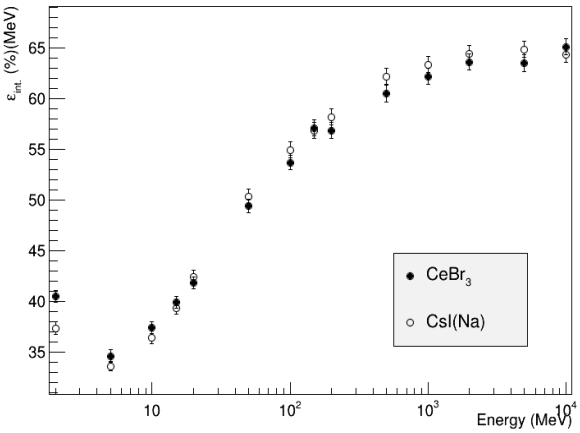

Figura 6.3.: Intrinsic efficiency comparison for bare $CeBr_3$ and CsI crystals.

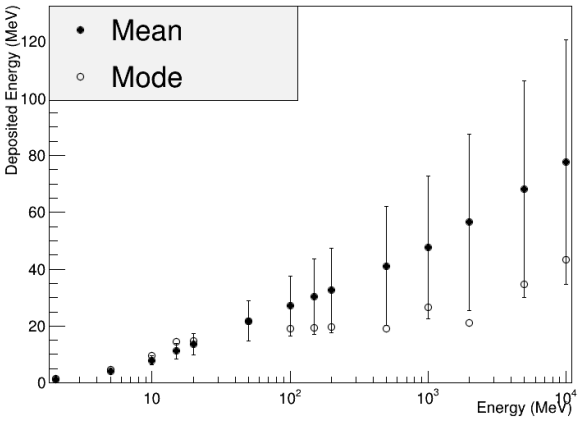

Figura 6.4.: Most probable deposited energy value (mode) and mean deposited energy value (mean) for $CeBr_3$ for electrons at different initial energies.

rio: uno completo y uno en el que se ha practicando una pequeña abertura para permitir el paso de partículas α.

Los fotodetectores empleados para la detección de los fotones generados en los cristales centelladores son cuatro tubos fotomultiplicadores mod. R7600U-200 y un diodo PIN mod. S3204-08, todos fabricados por Hamamatsu. El correcto acoplamiento entre los fotodectores y los cristales garantiza la máxima transmisión de luz producida a los fotodectores. Para ello se ha utilizado grasa óptica, BC-630 de Saint-Gobain Crystals, para el acoplamiento entre los cristales $CeBr_3$ y CeF_3 (con dos longitudes: 40 mm y 50 mm) y tres fotomultiplicadores mod. R7600U-200. Los detectores acoplados reciben los nombres de $CeBr_3$, CeF_3_L40 y CeF_3_50 respectivamente. El cristal de CsI(Na), ha sido acoplado a un fotomultiplicador mod. R7600U-200 utilizando el cemento óptico RTV 681 de Scionix. El detector acoplado recibe el nombre de CsI(Na). Por último, este mismo cristal fue acoplado a un diodo PIN cuyo modelo ha sido referenciado con anterioridad utilizando un adesivo óptico n = 1.582 de Meltmount.

A continuación, las técnicas y métodos expuestos con anterioridad se han aplicado para obtener la información de las señales producidas por los detectores. Para ello se han utilizado diferentes tipos de fuentes radiactivas: emisores γ como ^{152}Eu, ^{137}Cs, ^{60}Co and ^{88}Y, un emisor β, ^{90}Sr, una fuente de partículas α, ^{238}Pu, y una fuente de Am-Be, que emite tanto γ como neutrones. Las pruebas realizadas con estas fuentes radiactivas permiten el estudio de los detectores de radiación en un rango de energías desde 121 a 4444 MeV.

Para el estudio de la linealidad y la resolución en energía el montaje experimental consta de los detectores $CeBr_3$ y CsI(Na) cuya señal de salida es conectada a sus respectivas tarjetas electrónicas *strecher* cuya salida se conecta a un módulo espectroscóico mod. 2022 de CANBERRA [20]. La salida del amplificador espectroscópico alimenta el analizador multicanal MCA 8000A de AmpTek Inc. [48] El montaje para el detector PDCsI(Na) es similar, salvo que la tarjeta *stretcher* es sustituida por el módulo preamplificador MPR-1 de Mesytec [47]. Para dicho estudio, se ha utilizado la fuente radiactiva ^{152}Eu debido a la emisión de ocho picos de radiación γ de relativa alta intensidad, cuyas energías y cocientes de ramificación, entre paréntesis son: 121 (25.6 %), 244 (7.6 %), 344 (26.5 %), 778 (12.9 %), 964

(14.6 %), 1085 (10.2 %), 1111 (13.6 %) y 1408 (21.0 %). La resolución energía de los detectores se ha caulculado, una vez sustraída la contribución del fondo de radiación, a través de una función suma con dos términos: una función gaussian más un función linear. Los parámetros centro y desviación estándar de la función gaussiana, proporcionan el valor central del fotopico relacionado directamente con la energía y un valor relacionado con la resolución respectivamente. Se han realizado calibraciones energía-centro del fotopico para los detectores CsI(Na), $CeBr_3$ y PDCsI(Na) dando como resultado una relación lineal. En cuanto a la resolución en energía obtenida de los fotopicos de los espectros de ^{152}Eu, calculada siguiendo la Ec.

$$R(E) = \frac{FWHM}{E} \times 100 \equiv \frac{2{,}35\sigma}{E} \times 100 \tag{6.2}$$

donde σ es la desviación estándar de la función gaussiana y FWHM el ancho a la semi-altura del pico, se ha ajustado a una función de la forma

$$R(E) = \frac{p_0}{E^{p_1}} \tag{6.3}$$

para averiguar la dependencia de la resolución en energía en función de la energía. Este ajuste se ha utilizado para calcular la resolución en energía para el fotopico de ^{137}Cs a 662 keV y a una energía igual a 1 MeV, para ser comparado posteriormente con el valor de resolución obtenido a través del ajuste explicado arriba (función gaussiana más función linear) de la medida de un espectro de ^{137}Cs. Se ha estudiado el comportamiento de los detectores en un rango de temperatura cercano a la temperatura ambiente, utilizando el montaje experimental descrito anteriormente. Además se ha utilizado una sonda de temperatura mod. para monitorizarla. Los datos obtenidos a través de estas medidas confirman que la resolución en energía no se ve afectada en la región de temperatura estudiadas, estando de acuerdo con los resultados de las Refs. [9] y [54].

Los detectores de CeF_3 presentan una pobre resolución en energía, dificultado así la capacidad de distinguir fotopicos. Debido a su falta de higroscopicidad, la medida con partículas α ha sido posible debido a la abertura realizada en el envoltorio del detector CeF_3_L40. En la Fig. 6.5

se muestra el espectro depositado por las partículas *alpha* emitidas por una fuente radioactiva de ^{238}Pu. Como referencia, se utiliza el espectro adquirido por el mismo detector para radiación γ de 662 keV emitida por el ^{137}Cs. Se observa que la energía depositada en el cristal es menor que la depositda por la radiación γ, debido principalmente a la alta densidad de ionización [51, 52].

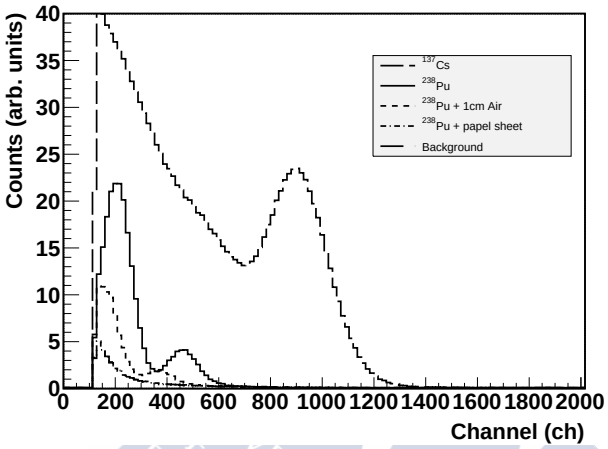

Figura 6.5.: Espectro ^{238}Pu usando CeF_3 para diferentes configuraciones de la medida. El espectro de ^{137}Cs se usa como referencia para la energía depositada.

La resolución temporal de los detectores $CeBr_3$ y CsI(Na) se ha medido utilizando el método de coincidencias. Para ello se han medido la forma de los pulsos producidos por un plásctico centellador acoplado a un fotomultiplicador y uno de los detectores colocados en paralelo producidas por el paso de rayos cómicos. La adquisición de las formas de la señal se ha realizado utilizando un osciloscopio fabricado por YOKOGAWA mod. 9140 cuya frecuencia de muestreo es 5 GS/s. Los pulsos producidos en el CsI(Na) han sido filtrados usando un filtro triangular para obtener mayor precisión a la hora de calcular el tiempo inicial de los pulsos. Los resultados obtenidos son una resolución temporal de 230 ps para el caso del $CeBr_3$ y de 0.920 ns para el caso del CsI(Na).

El tiempo de bajada de ambos detectores, $CeBr_3$ y CsI(Na), se ha ob-

tenido calculando el pulso promedio de un conjunto de formas de pulso proveniente de radiación γ de 662 keV. El tiempo de bajada obtenido es de 12 ns para el caso del $CeBr_3$ y dos componentes de 473 y 2588 ns se han observado para el caso del CsI(Na). Además, se ha relizado una comparación entre los pulsos promedio provenientes de rayos cósmicos (principalmente μs), partículas β y radiación γ. Los pulsos promedio para cada partícula no difieren unos de otros para ambos dectores lo que implica que no pueden realizar esta identificación.

Un filtro trapezoidal se ha uitlizado con los pulsos producidos en el detector $CeBr_3$, obteniedo como resultado un pulsos filtrado que presenta una mejor relación señal-ruido, una corrección de la línea de base así como una forma de pulso mejor definida que facilita la definición y cálculo de observables que contienen la información del pulso original. En la Fig. 6.6 se muestra un espectro de ^{137}Cs obtenido calculando el valor máximo de la amplitud de los pulsos filtrados gracias al filtro trapezoidal.

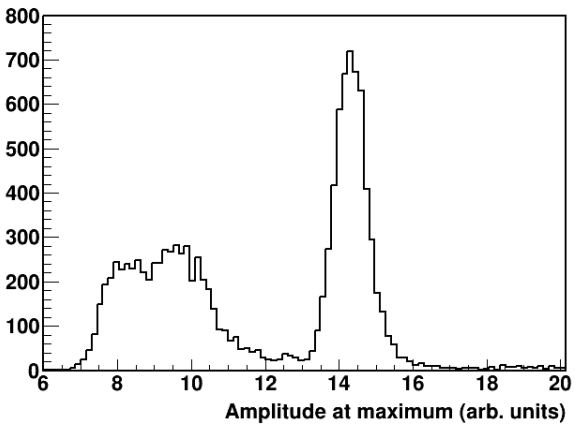

Figura 6.6.: Espectro de ^{137}Cs obtenido a partir de la señal filtrada por un filtro FIR trapezoidal del detector $CeBr_3$.

Debido a la posibilidad de detección de partículas α por el detector CeF_3_L40, se ha procedido a tratar de identificar las partículas α de la radiación γ a través de la definición observables de la señales producidas por el detector. El pulso promedio para cada tipo de partículas confirma que existen diferencias en su forma. Atendiendo a estas diferencias, se

definen como observables el área de bajada y la pendiente de la recta ajustada al flanco de subida de la señal. Representando ambos observables para cada tipo de partícula, se observa una ligera diferencia, pero no es suficiente para confirmar la identificación.

La instalación n_TOF (Neutron Time Of Flight) es una instalación situada en el CERN decicada al estudio de reacciones inducidas por neutrones, principalmente la captura radiactiva (n, γ) y la fisión (n, f) siendo de gran interés en los campos de la astrofísca y del desarrollo de nuevas tecnologías dedicadas a la producción de energía nuclear y a la transmutación de residuos radioactivos. Los neutrones son producidos una vez que los grupos protones de 7 ns (rms)y 20 GeV/c procedentes del acelerador (PS) inciden sobre un blanco de espalación. El blanco constituido por plomo está rodeado de un circuito de agua que actúa como moderador. A 185 m se encuentra la sala experimental 1 (EAR1) precedida por la línea de haz 1 en la que se encuentra diferentes elementos que optimizan el haz de neutrones antes de llegar a la sala expermiental. Verticalmente y desde el blanco de espalación, se encuentra la sala experimental 2 (EAR2), precedida por la línea de haz 2, que al igual que en la línea de haz 1, dispone de varios elementos para optimizar el haz de neutrones.

Durante la campaña de medidas realizada en 2012 en el experimento n_TOF se realizaron medidas de la radiación prompt-γ emitida en las reacciones de captura neutrónica de los isótopos ^{107}Ag, ^{109}Ag y ^{197}Au para los detectores $CeBr_3$ y CsI(Na). Para ello se realizó un algoritmo digital basado en el filtro trapezoizal para calcular el tiempo de inicio de las señales que es clave para la utilización de la técnica de tiempo de vuelo. Se han comparado los resultados obtenidos, siendo estos proporcionales a los datos proporcionados para las secciones eficaces de los tres isótopos proporcionados por la librería CENDL-3.1 para el caso de la Ag y la ENDF/B-VII.1 para el caso del Au.

En la misma campaña se realizaron medidas en coincidencia con los detectores gaseosos, PPAC (Parallel Plate Avalanche Counter), desarrollados y construidos en el IPN d'Orsay (Francia). En este detector, consiste en una vasija de alumio que contiene 10 PPACs entre los que se encuentran intercalados 9 blancos como se muestra esquemáticamente en la Fig. 6.7. La radiación prompt-γ emitida por la reacción (n,f) en el penúltimo blan-

co, ^{235}U ha sido medida por los detectores $CeBr_3$ y CsI(Na). El algoritmo utilizado para las reacciones de captura neutrónica es válido para analizar las señales producidas por los detectores. Un método específico de coincidencia se ha desarrollado para seleccionar los prompt-γ emitidos por la reacción de fisión (n,f). A pesar de la baja estadística, queda probado la validez del método para seleccionar dicha radiación.

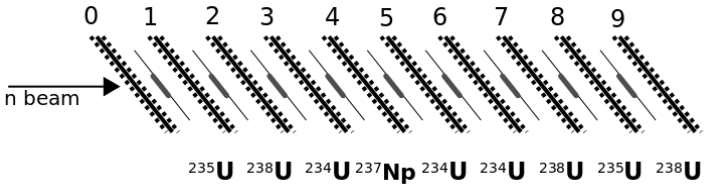

Figura 6.7.: Esquema de la configuración de las PPACs donde los blancos se encuentran intercalados.

Durante el proceso de espalación además de neutrones, se produce una gran cantidad de radiación asi como partículas neutras y cargadas. Estos productos de la espalación viajan a través de las líneas de haz 1 y 2 interaccionanado con los elementos dispuestos en ellas produciendo nuevas partículas y radiación perturbando el haz de neutrones. La contribución de estas partículas y radiación provoca incovenientes en las salas experimentales ya que ciega los detectores durante un lapso de tiempo dependiente de la naturaleza y electrónica asociada a los detectores, entorpeciendo la medida de los neutrones más energéticos producidos en el proceso de espalación. Fig. 4.20. Este indeseable efecto, se denomina, γ-flash.

Los detectores $CeBr_3$, CsI(Na) y CeF_3_L50 ha sido utilizados para caracterizar el γ-flash. Las medidas se han realizado durante las campañas de 2012 en la sala experimental 1 y la puesta en marcha de 2014 la sala expermiental 2. Se parte de la hipótesis de que el γ-flash es un efecto producido principalmente por la radiación γ producida durante el proceso de espalación y la desintegración de alguno de sus productos. Se ha estudiado el promedio de las señales producidas para el γ-flash para $CeBr_3$, CeF_3_L50 y un plástico centelleador, cuya eficiencia para radiación es muy baja,γ colocado en coincidencia con ambos. Los resultados obtenidos indican que hay una compronente denominada prompt formada principalmente por radiación γ. Esto también ha sido constatado por detectores de

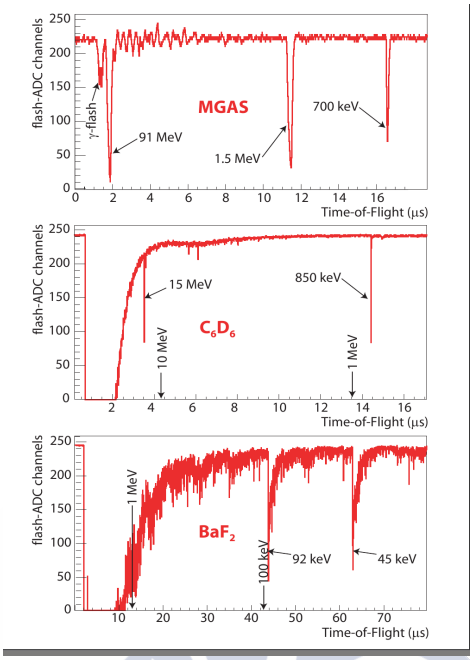

Figura 6.8.: Señales producidas por el γ-flash para diferentes detectores: Micromegas, C6D6 y BaF2.

estado sólido, diamante, gaseosos, PPACs. Los resultados obtenidos concuerdan con los obtenidos de las simulaciontes realizadas con el software GEANT4 realizadas por otros grupos de la colaboración n_TOF.

Conclusiones Las principales conclusiones de este trabajo son:

- Para estos cristales de tamaño relativamente pequeño, se han obtenido una alta eficiencia de detección para radiación γ y una medida precisa de la energía depositada por partículas β a través del programa de simulación EnsarRoot.
- La reacción inducida por neutrones (n,γ) para los isótopos ^{107}Ag, ^{109}Ag y ^{197}Au ha sido medida en un rango de energía de los neutrones comprendido entre 1 y 100 eV a través de la técnica de tiempo de vuelo. A pesar de la baja estadística disponible, debido a la muy

reducida aceptancia angular definida por el tamaño pequeño de los detectores, se ha probado la utilidad del uso de esta técnica para detectar la radiación *prompt*-γ emitida por las reacciones de captura en un ambiente con presencia de ruido.

- La radiación *prompt*-γ emitida por la reacción ^{235}U(n,f) ha sido medida en paralelo a la cámara gaseosa PPAC, in un rango de energías del neutron comprendido entre 1 y 100 eV a través del método de concidencias. La estadística conseguida ha sido baja, pero, sin embargo, la robustez del método de coincidencias usando las rutinas de software específicas ha sido probado, permitiendo seleccionar la radiación prompt-*gamma* que proviene de una reacción de fisión concreta.
- Usando los detectores utilizados en este trabajo, el *gamma*-flash n_TOF ha sido caracterizado en ambas salas experimentales, EAR1 y EAR2. Puede deducirse que la contribución principal proviene de la emisión de radiación γ que procede del proceso de espalación producido por los protones que inciden en el blanco de plomo, seguido de su conversión en pares e^+-e^- focalizados hacia adelante. Los resultados fueron comparados con diferentes detectores de estado sólido y gaseosos utilizados en el experimento n_TOF, así como con las simulaciones realizadas por otros grupos pertenecientes a la colaboración n_TOF, confirmando esta hipótesis.

USC
UNIVERSIDADE
DE SANTIAGO
DE COMPOSTELA

A. Voltage Divider

The use of decoupling capacitors is a common technique to supply current between dynodes stages. The E5996 socket includes this technique, capacitors that are connected following the serial method. Oscilloscope measurements of the PMT signals proceed from a $CeBr_3$ crystal irradiated by a ^{137}Cs radioactive source, show that the amplitude of the pulses is about 5 V and their duration is about 100 ns, falling exponentially from the maximum. The mean current over 50 Ω is approximately 100 mA, and the integrated charge, Q, is 10 nC. In order to maintain the detector within the linear region, see Fig. 1.2, the capacitance value C between the 10^{th} dynode and the anode, should be around 100 times the output charge as follows:

$$C > 100 \cdot \frac{Q}{V_{10^{th}dy}}, \tag{A.1}$$

where V is the voltage supply between the last dynode and the anode,

$$V_{10^{th}dy} = |-800\ V| \frac{220\ k\Omega}{2700\ k\Omega} = 64\ V \tag{A.2}$$

Thus,

$$C > 16\ nF \tag{A.3}$$

The original capacitor has 10 nF. Therefore, the C value shall be increased. A capacitance value of 22 nF was welded in parallel to C (C_3 in the scheme show in Fig. A.1), left) of the socket E678-32B from Hamamatsu. See [1]. So that, a variation of voltage between last dynode and anode is less than 1%.

$$\Delta V = \frac{\Delta Q}{C} = \frac{14\ nC}{32\ nF} = 0.44\ V \tag{A.4}$$

Gain reduction can be achieved by reducing the VD supply voltage. Conversely, the voltage distribution of the earlier VD stages should be

maintained to not affect the photoelectron collection efficiency and the secondary emission ratio of the first dynode. Due to this fact, a parallel resistance of 23.5 MΩ is connected between R_4 and R_8 (see Fig. A.1 , right). Every R'$_i$ has 470 kΩ resistance value. Thus,

$$R_i'' = \left(\frac{1}{R_i} + \frac{1}{R_i'}\right)^{-1} \text{ where } i \in [4,8]\,,\ R_i'' = 150\ k\Omega \tag{A.5}$$

The VD resistance value after modifications is 2.4 MΩ instead of the original value of 2.75MΩ, and the new nominal supply voltage between the anode and the cathode is 690 V, the nominal current circuit of 302 μA is increased and the gain is reduced due to the decrease of the voltage between dynodes Dy_3 and Dy_8 so that voltage applied between latter stages is enhanced. This is a corrective action to avoid output saturation caused by an increment in the electron density in the latter stages that leads to space charge effects disturbing the electron current. The ratio between dynode Dy_8 and the anode has been increased as it is shows in Table A.1. The new VD circuit follows a so-called tapered voltage divider circuit. An example of the improved linearity of the tapered VD versus normal VD is shown in Fig A.2

A.1

Electrodes	K	Dy1	Dy2	Dy3	Dy4	Dy5	Dy6	Dy7	Dy8	Dy9	Dy10	P
Hamamatsu	1.50	1.50	1.50	1.00	1.00	1.00	1.00	1.00	1.00	1.00	1.00	
USC design	2.2	2.2	2.2	1	1	1	1	1	1.47	1.47	1.47	

Table A.1.: Voltage dividers distribution from Hamatsu E5996 socket and the modified design by USC.

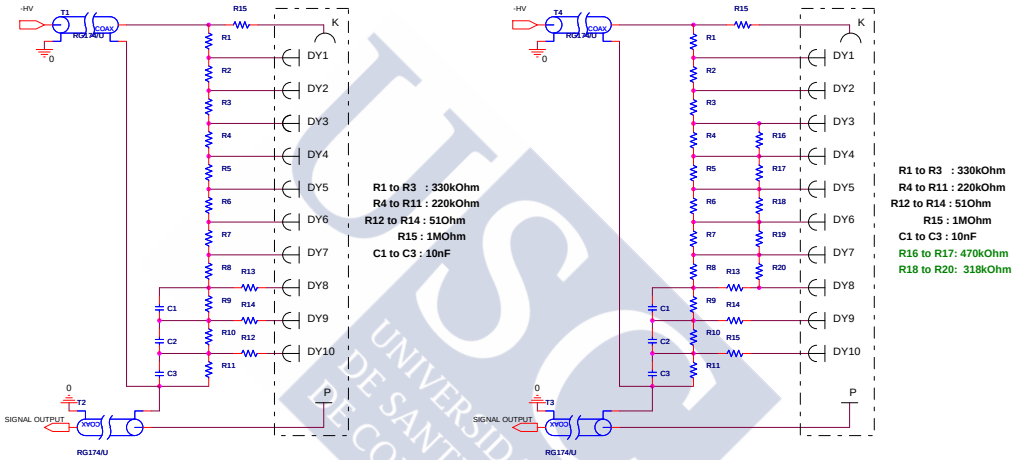

Figure A.1.: Left: Hamamatsu E5996 Voltage Divider. Right: modified version of the original Hamamatsu design to make it suitable for the very fast signals produced by high L.Y. crystals.

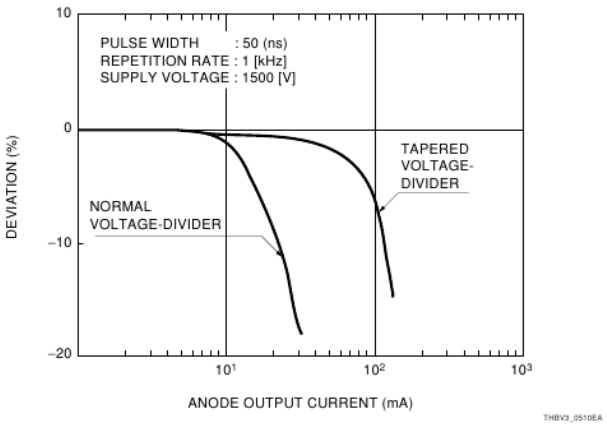

Figure A.2.: Deviation from linear behaviour in normal and tapered voltage divider circuits. The linear response is maintained for one order of magnitude more for the tapered design. Courtesy of Hamamatsu Photonics K.K.

B. Equivalent Series Resistance (ESR) in capacitors

An ideal capacitor has an impedance follow by

$$Z = \frac{1}{j\omega C} \tag{B.1}$$

where C is the electrostatic capacitance of the capacitor. The impedance |Z| decreases inversely with the angular frequency ω. Fig. B.2 shows the behaviour of Eq. B.1

However, in actual capacitors, resistive (ESR) and inductive (ESL) effects contributes to the impedance, as it sketched in Fig. B.2. The resistive contribution are due to the dielectric substances, electrodes and other components whereas some parasitic inductance are due to electrodes, leads and other components. This fact leads to the frequency characteristics of the impedance to curve V-shaped (or U-shaped depending on the capacitor), shown in Fig. B.3. In the idea case, the ESR contribution is zero. Taking into account this, it clue when designing circuits since this enable the designer to determine, for instance, the noise suppression capabilities or the voltage fluctuations control capabilities of a power supply line [16].

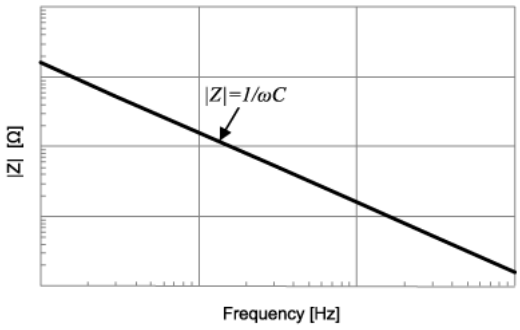

Figure B.1.: Frequency response of an ideal capacitor.Courtesy of Murata Electronics [16].

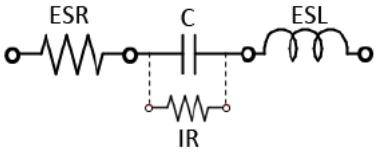

Figure B.2.: Equivalent circuit representation of an actual capacitor. Courtesy of Murata Electronics [16].

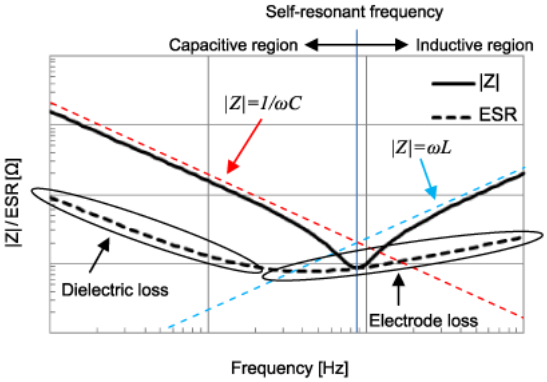

Figure B.3.: Frequency response of an actual capacitor. Courtesy of Murata Electronics [16].

C. *Stretcher PCBs* desing

The input signal is a current type, in order to convert it into a voltage type and to condition the impedance of the LEMO connector and the cable RG 174/U an impedance of 50 Ω is included at the input of the design.

The design, shows in Fig. C.1 consists in three active stages that are described below:

The signal from the $CeBr_3$-PMT is firstly conditioned prior to attack the Operation Amplifier, OA, to get proper operation within the bandwidth of the OA, is the LM6172 High Speed manufactured by Texas Instrument Incorporation [80], whose unity-gain bandwidth is 100 MHz . Since the $CeBr_3$-PMT rising time is around 10 ns, a RC passive filter is then arranged the bypass capacitor C_1. The capacitor C arranged in passive filter must be properly chosen in order to minimise the contribution of noise effects due to the equivalent series of resistance, ESR, that appear at high frequencies region. See Appendix B for a more detailed explanation.

The second stage is an active low-pass filter including a resistor, R19 in series to a in parallel RC chain form by R2 and C2, to control the gain of the filter and not to disturb/affect the frequency, 1/R2C2 = 0.5MHz , of the filter. At this point, the signal is still not conditioned for the SA input requirements. Two more active filter stages are needed: two low-pass filters, whose cut-off frequency is 1/R18C6 = 1 MHz and 1/R13C11 = 45kHz respectively for the second and the third stages. In both stages the OA LM6172 Dual High Speed whose unity-gain bandwidth is 100 MHz from Texas Instrument has been used/chosen. The output signal of the circuit meets the input requirements for the SA CANBERRA 2022. See Fig. C.2 (e)

An analog method has been followed to desing the *stretcher* circuit for the CsI(Na)-PMT.

The circuit has been designed and simulated using PSpice software, the

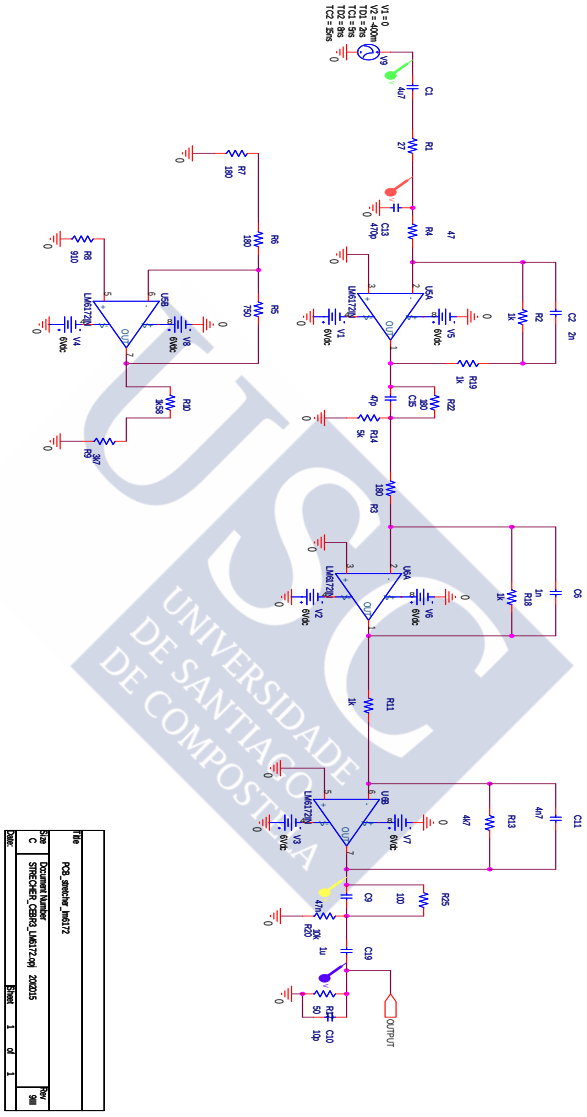

Figure C.1.: Stretcher circuit design for $CeBr_3$-PMT

PCB based on such design is implemented. Once the components were welded, the operation of the circuit is tested using a test probe connected to the oscilloscope YOKOGAWA DL9140 5GS/s 1GHz when the detector is providing signals from the detection of γ-rays from a radioactive source. The final value of the components have been determined by trial and error because of the presence of spurious impedances, among others, induces by the tracks.

Transfer function

When analysing the behaviour of an electronic circuit, applying mathematical properties simplify the calculations to find out the behaviour in the linear range of such circuit. Here most important properties are presented:

Superposition principle: For any two arbitrary input signals, Vinputa and Vinputb, the sum of both signals Vin1+Vin2, corresponds the sum of the independent output signals Vout1+Vout2.

Concepts such as *Impulse response* and *Transfer function* must be also introduced to understand the mathematical properties that will be exposed later/after:

Impulse response. The impulse response h(t) is the response of a system to a delta function like input pulse.

$$V_{in} = \delta(t)\ V_{out} = h(t) \tag{C.1}$$

Transfer function. The transfer function H(w) is the Fourier transform of the impulse response.

$$H(\omega) = \frac{1}{\sqrt{2\pi}} \int \exp^{-i\omega t}\, h(t)dt \tag{C.2}$$

A low passive filter, R1·C13 = 13 ns, is arranged previously to the first active stage in order to condition the input signal to the characteristics of the operation amplifier, onwards OA, LM6172 manufactured by TEXAS INSTRUMENTS []. This can be observed in the transfer function of such active filter:

$$H(\omega) = \frac{R2 + R3}{R1} \cdot \frac{1 + \omega \frac{R2R3}{R2+R3} C2}{1 + j\omega R2C2} \tag{C.3}$$

The output signal of this stage therefore, is inverted, amplified and integrated, what implies a wider signal. See fig. C.2 (a)

The output signal shows an undershoot which can be a problem when measuring pulse heights what is related to spectroscopy, especially at high rates producing a baseline shift which means a broaden of the photopeaks/peaks and, therefore, worsening of energy resolution. Such undershoot is caused by factor 1+jωR2C2 in Eq C.3, so to remove this undesirable effect, a so-called pole-zero cancellation circuit is arranged after the first active filter. Such circuit consists an a net of passive components, resistors and capacitors whose transfer function is

$$H(\omega) = \frac{1}{\sqrt{2\pi}} A \frac{1 + j\omega R22R14}{1 + j\omega AR22R14} \quad \text{where} \quad A = \frac{R14}{R22 + R14} \tag{C.4}$$

In this case, A = 0.96 and R22R14 = 8.5 ns which is a value close to 13 ns. The PSpice time domain simulation confirm the effectiveness of this pz cancellation method. See fig. C.2 (b) At this point, the signal is not still conditioned for the SA input requirements. Two more active filter stages are required: tow low-pass filter whose configuration is inverting. The transfer function of both filters are, for the second active filter:

$$H(\omega) = -\frac{R18}{R3} \frac{1}{1 + j\omega R18C6} \quad \text{where} \quad A = \frac{R18}{R3} = 5 \quad \text{and} \quad R18C6 = 22\mu s \tag{C.5}$$

for the third active filter:

$$H(\omega) = -\frac{R13}{R11} \frac{1}{1 + j\omega R13C11} \quad \text{where} \quad A = \frac{R18}{R3} = 5 \quad \text{and} \quad R18C6 = 1\mu s \tag{C.6}$$

The output signal at this stage is shown in Fig. C.2 (c)

The undershoot at this stage is corrected by the pz cancellation circuit, where

$$A = 0.99 \quad \text{and} \quad R20C9 = 4.7\mu s \tag{C.7}$$

The output signal at this stage is shown in Fig. C.2 (d)

A capacitor, C19 is arranged in series after the pz cancellation stage in order to eliminate any DC contribution.

The CsI(Na)-PMT *stretcher PCB* design is shown in Fig. C.3 The Operation Amplifier, OA, used in this desing is the High Speed AD8056 manufactured by Analog Devices Inc., whose unity-gain bandwidth is 300 MHz [81].

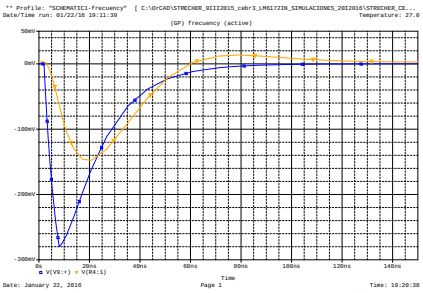

(a) Input signal (blue). Shaped signal after C1 (yellow)

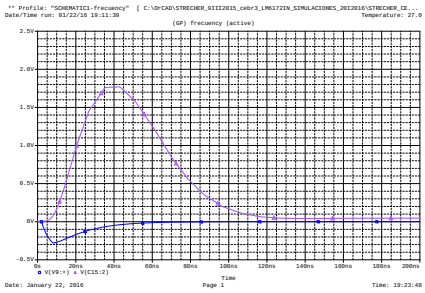

(b) First active filter output

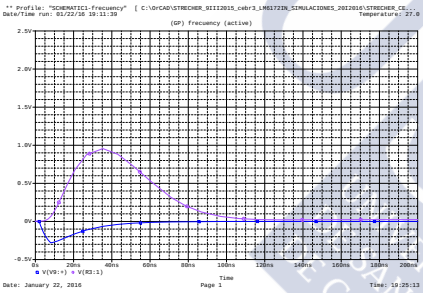

(c) PZ cancellation output

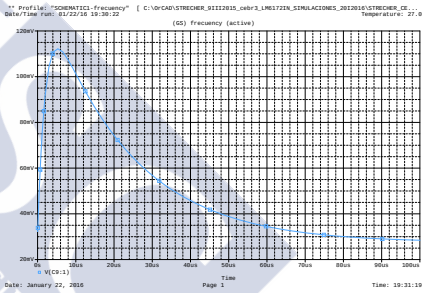

(d) Third active filter output

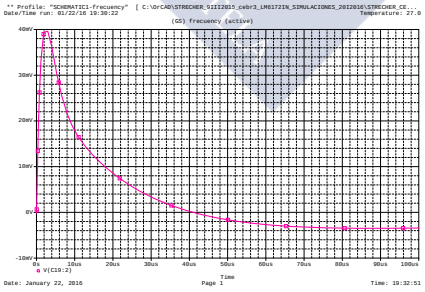

(e) Circuit output

Figure C.2.: Signal at different stages of the conditioning circuit simulated using PSpice for $CeBr_3$-PMT.

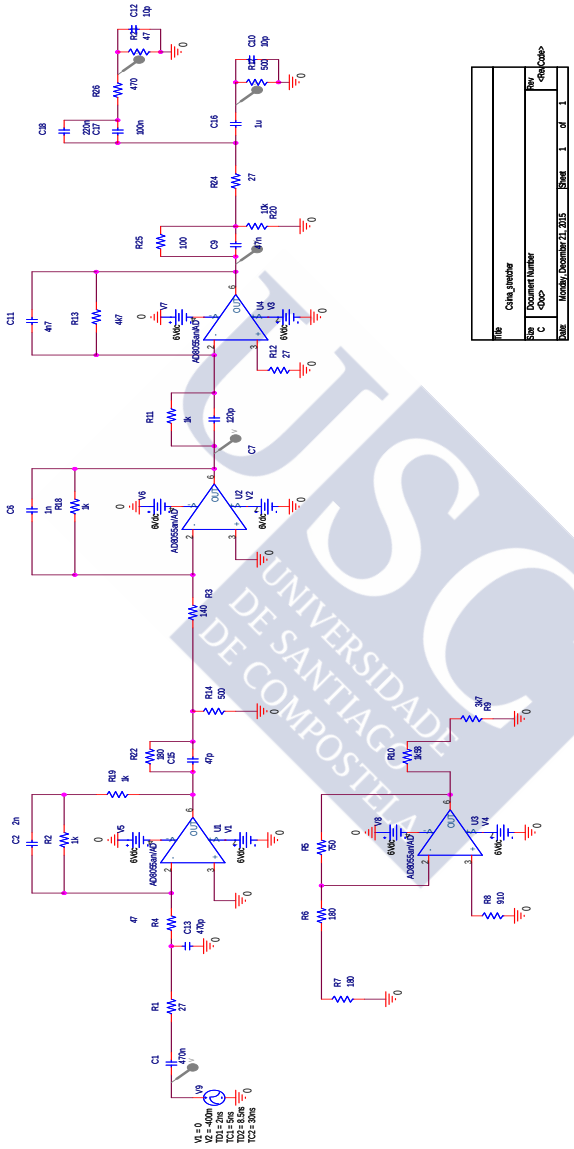

Figure C.3.: Stretcher design circuit for CsI(Na)-PMT.

USC
UNIVERSIDADE
DE SANTIAGO
DE COMPOSTELA

D. Attenuator design

The simulation of the Attenuator was simulated using PSpice program OrCAD 10.5 software package. It consists on the simulation of two Zener diode manufactured by Panasonic connected to a 30 ω resistor. The circuit can be seen in Fig. D.1

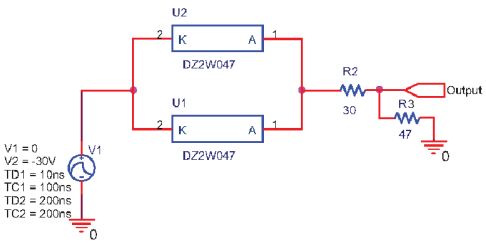

Figure D.1.: Attenuator desing based on Zener diode mod. DZ2W047 from Panasonic.

USC
UNIVERSIDADE
DE SANTIAGO
DE COMPOSTELA

E. Bethe-Bloch formula

$$-\frac{dE}{dx} = \frac{4\pi n z^2 Z^2 e^4}{m_e v}\left\{\ln\frac{2m_e c^2}{I\left[1-\left(\frac{v}{c}\right)^2\right]} - \left(\frac{v}{c}\right)^2\right\} \tag{E.1}$$

where n is the electron density of the material and Z its atomic number, m_e the electron mass, v is the speed and ze the charge of the particle, c the speed of light in vacuum and I is a tabulated parameter having the meaning of some kind of mean excitation potential of the stopping material.[82]

The maximum energy transferred in a collision to a free electron atom by an incident particle with mass M, is given by:

$$T_{max} = \frac{2m_e c^2 \beta^2 \gamma^2}{1 + 2\gamma m_e/M + (m_e/M)^2} \tag{E.2}$$

with $\beta = \frac{v}{c}$ and $\gamma = \frac{1}{\sqrt{1-\beta^2}}$

Commonly, the Eq. E.1 is rearranged taking into account the maximum energy transferred (Eq. E.2) and when some corrections are added:

$$-\langle\frac{dE}{dx}\rangle = K z^2 \frac{Z}{A}\frac{1}{\beta^2}\left[\frac{1}{2}\ln\frac{2m_e c^2\beta^2\gamma^2 T_{max}}{I^2} - \beta^2 - \frac{\delta(\beta\gamma)}{2}\right] \tag{E.3}$$

In Eq. E.3, $K = 4\pi N_A r_e^2 m_e c^2$ t where N_A is the Avogadro's number and the classical electron radius $r_e = e/4\pi\epsilon_0 m_e c^2$. The term $\delta/2$ accounts for the density effect correction to ionization energy loss. As the particle energy increases, the distance-collision contribution increases as $ln(\beta\gamma)$, neglecting polarisation effects in the material thus, the term $\delta/2$ is introduce in Bethe-Bloch formula E.3:

$$\delta/2 \longrightarrow ln\left(\frac{\hbar\omega_p}{I}\right) + ln(\beta\gamma) - \frac{1}{2} \tag{E.4}$$

where $\hbar\omega_p = \sqrt{4\pi N_e r_e^3 m_e c^2/\alpha}$ is the plasma energy of the medium and α the fine structure constant.

F. EnsarRoot

EnsarRoot [17] is the simulation and analysis framework for the ENSAR Project [83], under the Research Joint Action, SiNuRSE [84] and it is intended to solve problems identified in the simulation of complex nuclear physics experiments. EnsarROOT inherit most of its features from the FairRoot library [85] which is fully based on the ROOT system [86]. The framework uses the Virtual Monte Carlo concept which allows to perform simulations using different Monte Carlo engines such as Geant3, Geant4 or Fluka [87, 88, 89] without changing the user code. The framework also delivers base classes which enable the users to construct their detector and analysis tasks in a simple way. The event reconstruction is also a feature of such framework, that also provides a generic track follower based on Geane which allows precise and fast tracking algorithm developments [90].

EnsarRoot, based on the FairRoot library, includes event generators and specific physics lists for nuclear physics experiments, as well as examples of simple set-ups. The user is able to create simulated data and perform analysis within the same framework. It also provides an interface for track visualisation event-by-event and the detector geometry, see Fig. F.1.

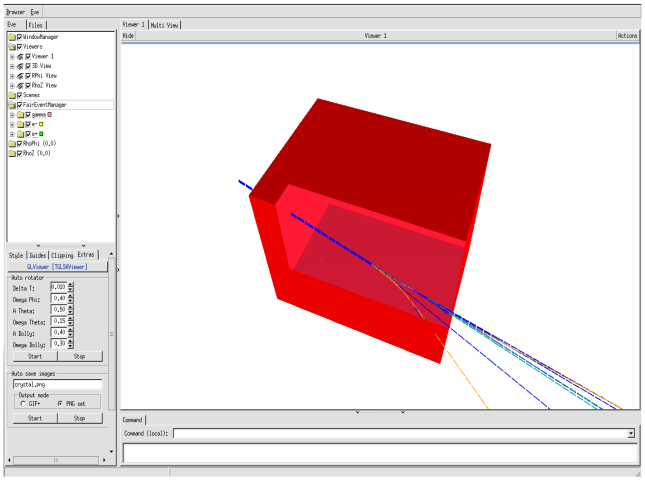

Figure F.1.: Event visualiser for the EnsarRoot framework[17]. A scintillator crystal is 3D sketched and the traces for different particles when an incident γ-ray hits the crystal are distinguished.

G. Spectra from EnsarRoot simulations

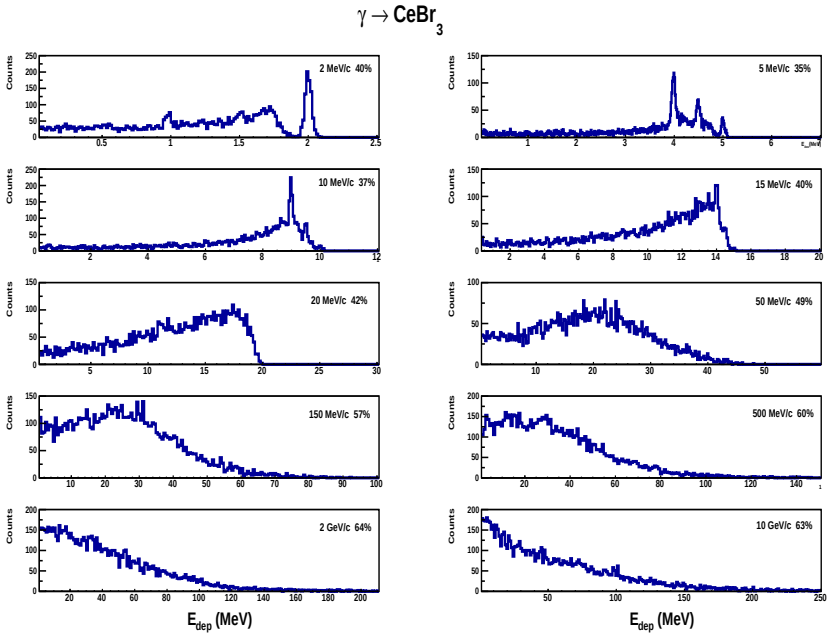

Figure G.1.: $CeBr_3$ bare crystal. Energy deposited spectra at different initial momentum. Incident particles: γ incident.

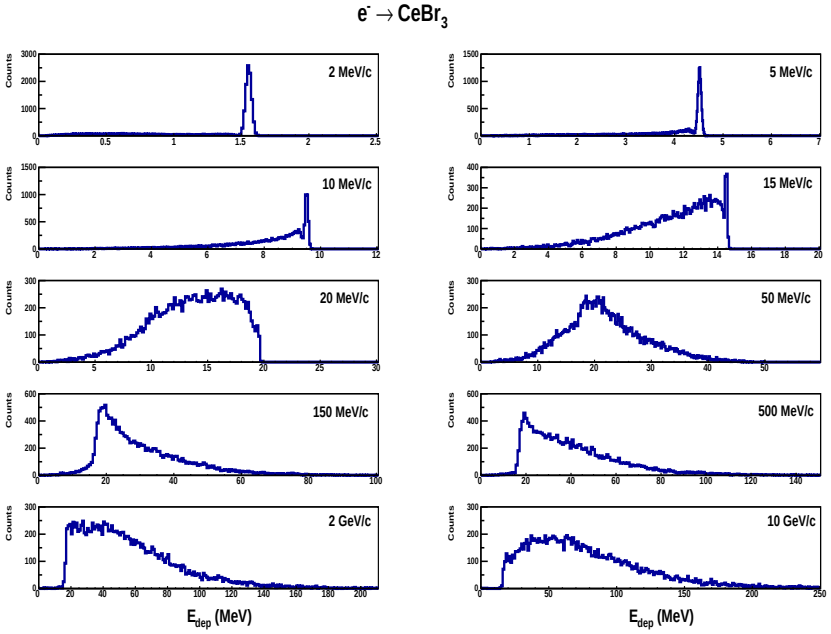

Figure G.2.: $CeBr_3$ bare crystal. Energy deposited spectra at different initial momentum. Incident particles: e^- incident.

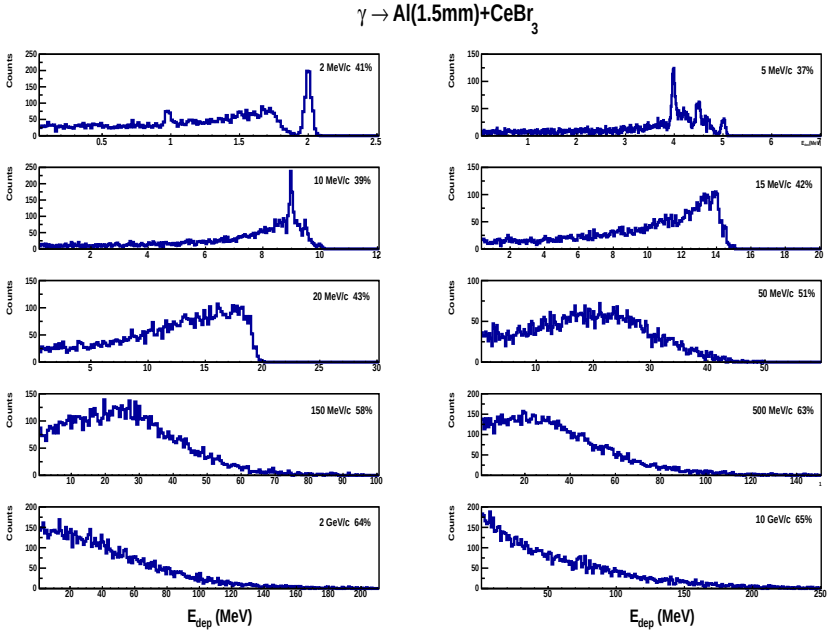

Figure G.3.: $CeBr_3$ bare crystal+Al foil 1.5 mm. Energy deposited spectra at different initial momentum. Incident particles: γ incident

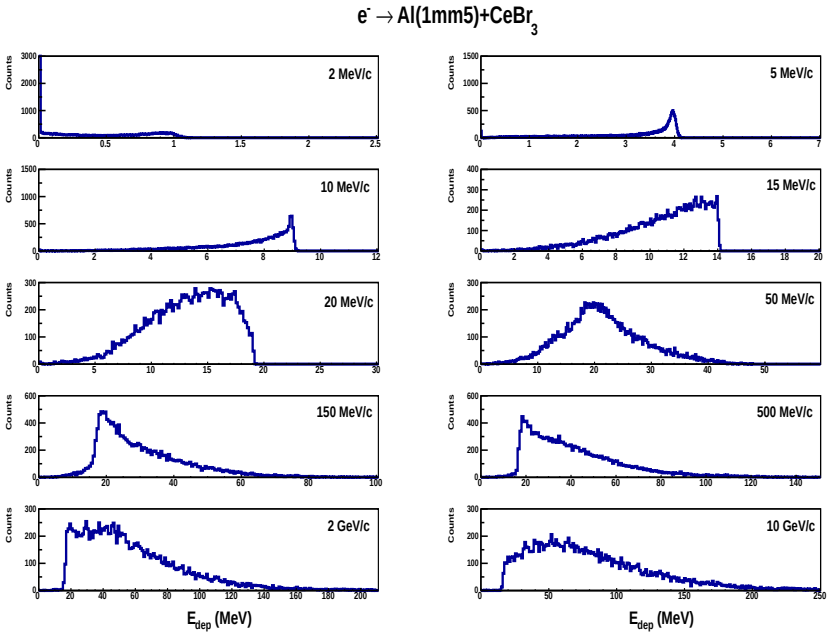

Figure G.4.: $CeBr_3$ bare crystal+Al foil 1.5 mm. Energy deposited spectra at different initial momentum. Incident particles: e^- incident

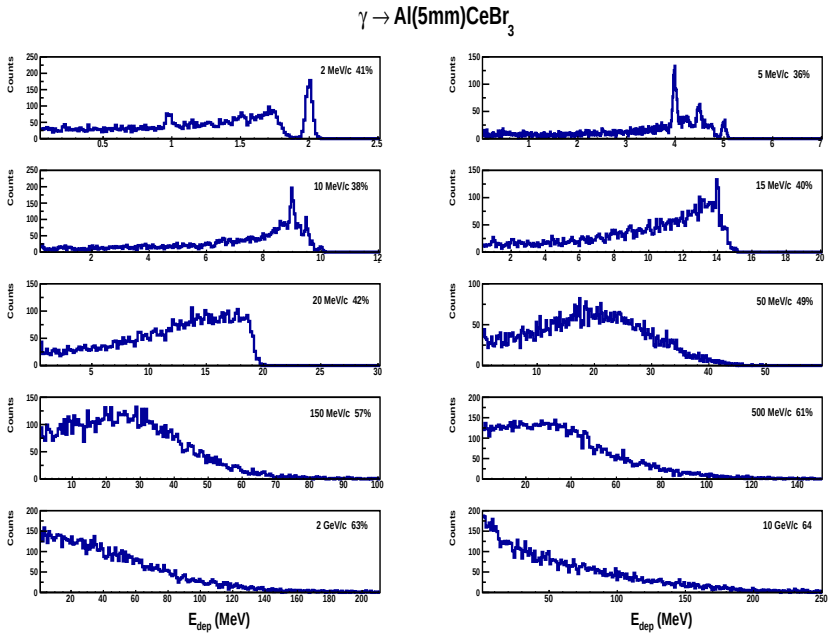

Figure G.5.: $CeBr_3$ bare crystal+Al foil 5 mm. Energy deposited spectra at different initial momentum. Incident particles: γ incident

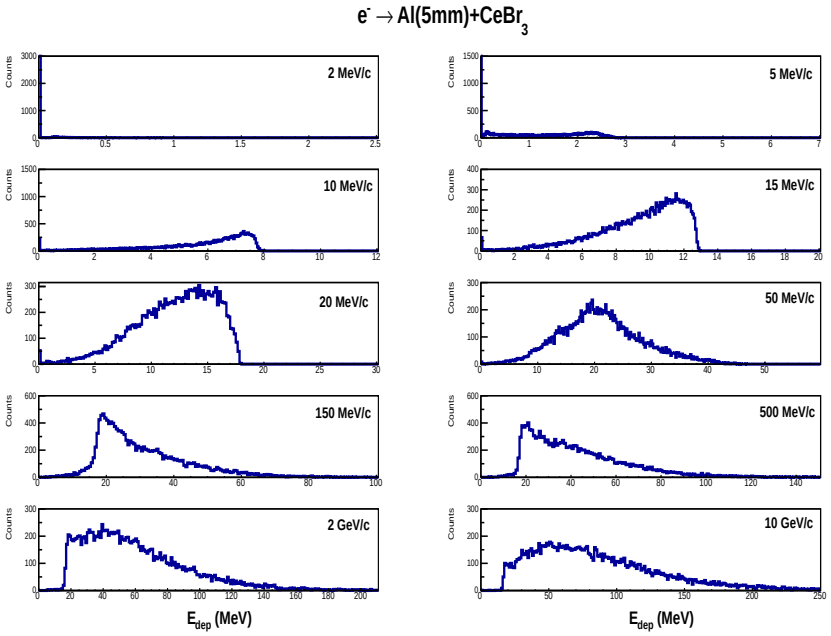

Figure G.6.: $CeBr_3$ bare crystal+Al foil 5 mm. Energy deposited spectra at different initial momentum. Incident particles: e^- incident

CsI(Na) simulations

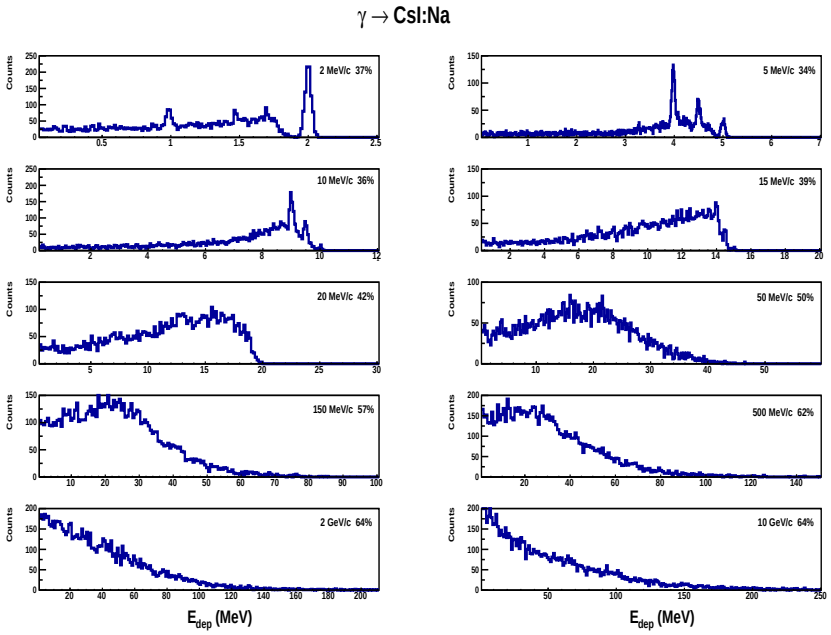

Figure G.7.: CsI(Na) bare crystal. Energy deposited spectra at different initial momentum. Incident particles: γ incident

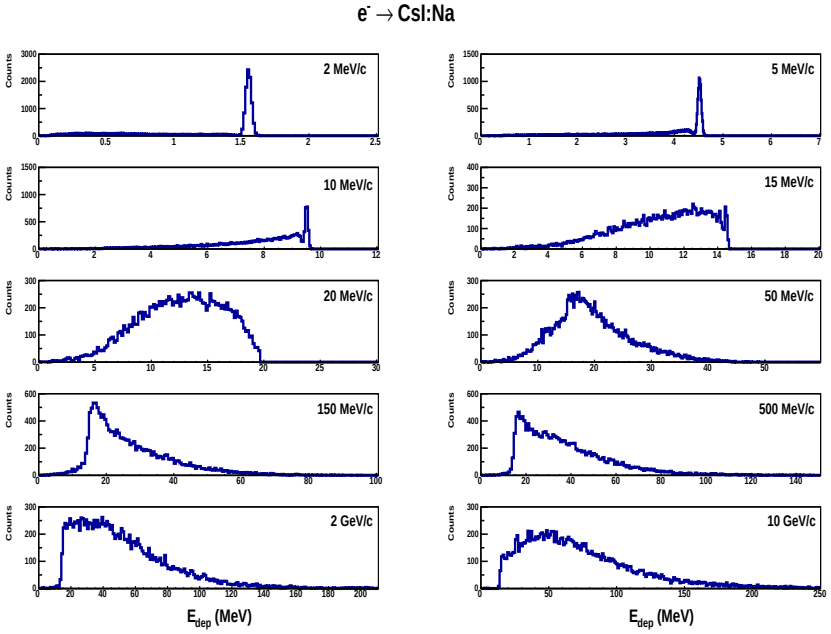

Figure G.8.: CsI(Na) bare crystal. Energy deposited spectra at different initial momentum. Incident particles: e^- incident

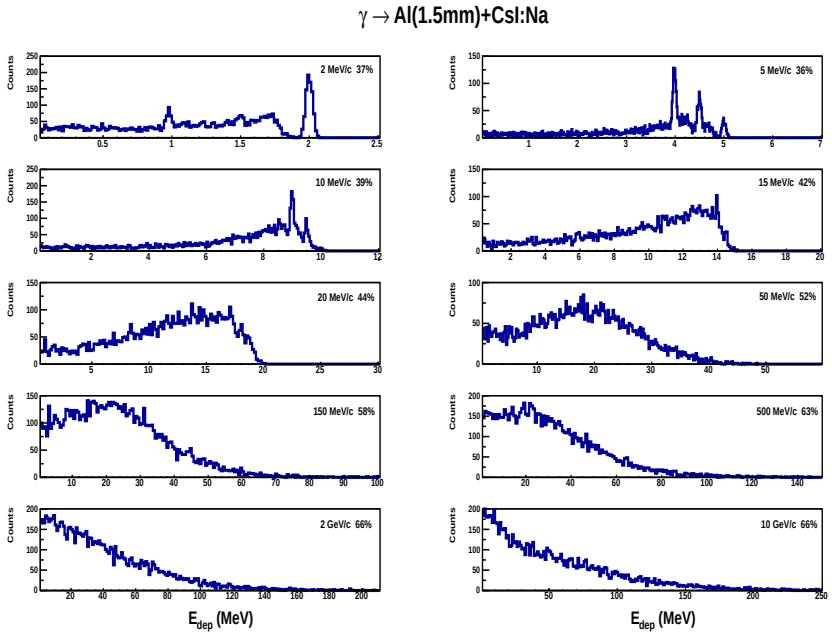

Figure G.9.: CsI(Na) bare crystal+Al foil 1.5 mm. Energy deposited spectra at different initial momentum. Incident particles: γ incident

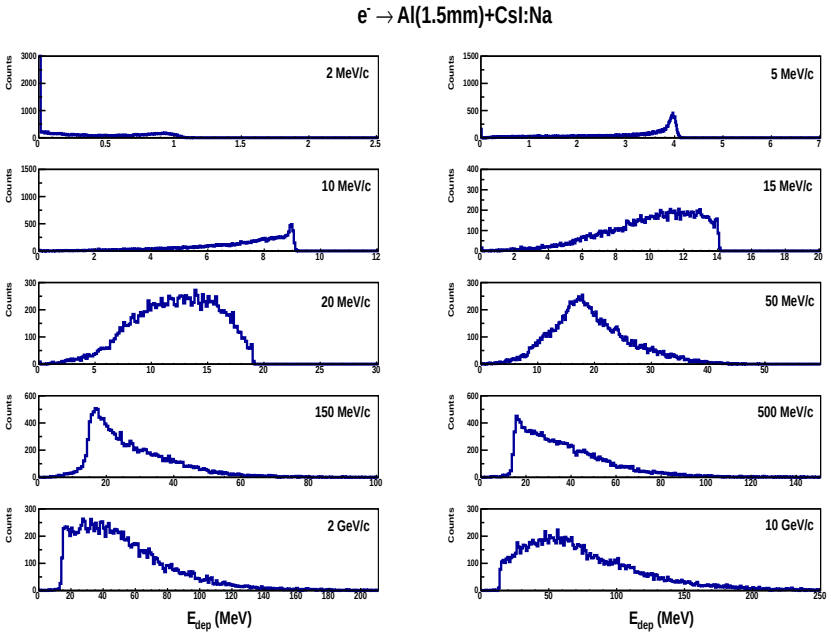

Figure G.10.: CsI(Na) bare crystal+Al foil 1.5 mm. Energy deposited spectra at different initial momentum. Incident particles: e^- incident

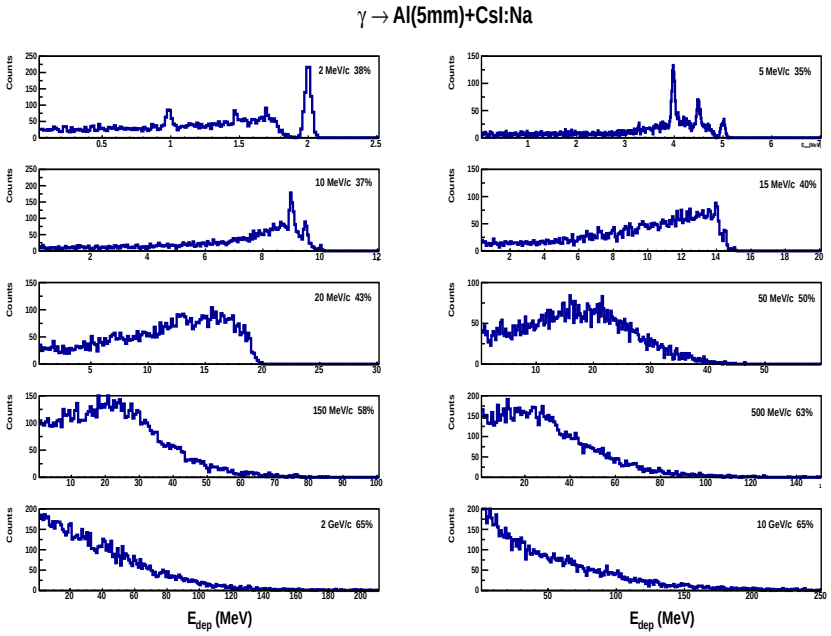

Figure G.11.: CsI(Na) bare crystal+Al foil 5 mm. Energy deposited spectra at different initial momentum. Incident particles: γ incident

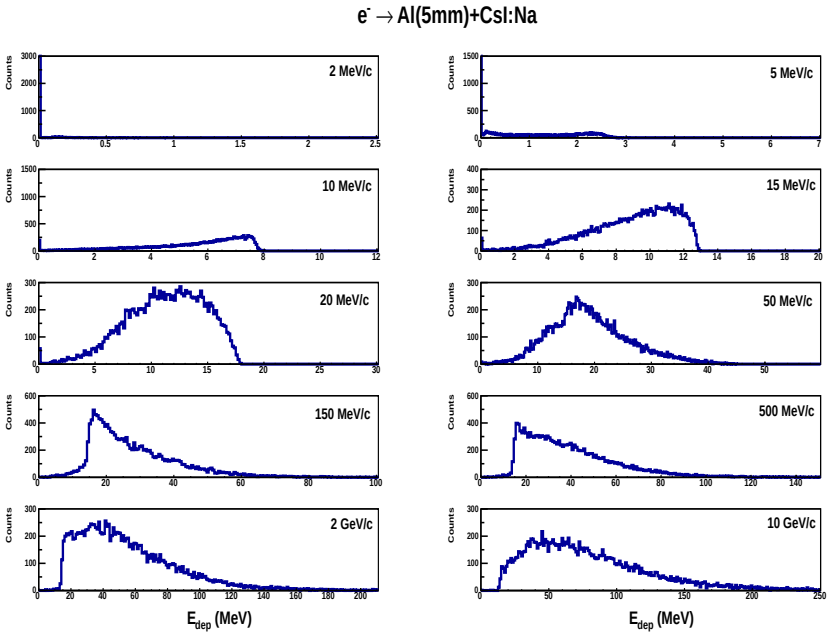

Figure G.12.: CsI(Na) bare crystal+ Al foil 5 mm. Energy deposited spectra at different initial momentum. Incident particles: e^- incident

Bibliography

[1] Hamamatsu Photonics K.K. Editorial Committee. *PHOTOMULTIPLIER TUBES. Basics and Applicaltions. 3rd EDITION (Edition 3a) No. TOTH9001E01a.* Hamamatsu Photonics K.K. Electron Tube Division, 2007.

[2] S.W. Smith. *Digital Signal Processing: A Practical Guide for Engineers and Scientists.* Demystifying technology series : by engineers, for engineers. Newnes, 2003.

[3] K. A. Olive et al. Review of Particle Physics. *Chin. Phys.*, C38:090001, 2014.

[4] Y. Yoshizawa and J. Takeuchi. The latest vacuum photodetector. *Nuclear Instruments and Methods in Physics Research Section A: Accelerators, Spectrometers, Detectors and Associated Equipment*, 387(1–2):33 – 37, 1997. New Developments in Photodetection.

[5] D. Renker and E. Lorenz. Advances in solid state photon detectors. *JINST*, 4:P04004, 2009.

[6] Hamamatsu Photonics K.K. Solid State Division. *Si PIN photodiode S3204/S3584 series. Cat. No. KPIN1051E10.* 2012.

[7] F.G.A. Quarati, P. Dorenbos, J. van der Biezen, Alan Owens, M. Selle, L. Parthier, and P. Schotanus. Scintillation and detection characteristics of high-sensitivity cebr3 gamma-ray spectrometers. *Nuclear Instruments and Methods in Physics Research Section A: Accelerators, Spectrometers, Detectors and Associated Equipment*, 729:596 – 604, 2013.

[8] Takao Inagaki, Yoshio Yoshimura, Yukio Kanda, Yoshikazu Matsumoto, and Kazuhiro Minami. Development of cef3 crystal for high-energy electromagnetic calorimetry. *Nuclear Instruments and Methods in Physics Research Section A: Accelerators, Spectrometers, Detectors*

and Associated Equipment, 443(1):126 – 135, 2000.

[9] Inc. Saint-Gobain Ceramics & Plastics. *CsI(Tl), CsI(Na), Cesium Iodide Scintillation Material.* 2007-2012.

[10] M. Barbagallo, C. Guerrero, and A. et. al. Tsinganis. High-accuracy determination of the neutron flux at n_tof. *The European Physical Journal A*, 49(12):1–11, 2013.

[11] A. Breskin and N. Zwang. A simple and accurate method for bidimensional position read-out of parallel plate avalanche counters. *Nuclear Instruments and Methods*, 146(2):461 – 463, 1977.

[12] D. Tarrío. *Neutron-induced fission fragment angular distribution at CERN n_ TOF: The Th-232 case.* PhD thesis, USC, 2012.

[13] C. Guerrero. *Measurements of the ^{237}Np and ^{240}Pu neutron capture cross sections at the CERN n_ TOF facility.* PhD thesis, UCM, 2010.

[14] G. Kornakov. Private communications.

[15] C. Weiss. *A CVD Diamond Detector for (n,a) Cross-Section Measurements.* PhD thesis, Vienna University of Technology, 2014.

[16] Ltd. Murata Manufacturing Co. *What are impedance/ESR frequency characteristics in capacitors? Category: Capacitor Room.* 2013.

[17] https://github.com/EnsarRootGroup/EnsarRoot/.

[18] P. Lecoq, A. Annenkov, A. Gektin, M. Korzhik, and C Pedrini. *Inorganic Scintillators for Detector Systems: Physical Principles and Crystal Engineering.* Particle Acceleration and Detection. Springer, 2006.

[19] William R Leo. *Techniques for nuclear and particle physics experiments: a how-to approach; 2nd ed.* Springer, Berlin, 1994.

[20] Canberra Industries Inc. *CANBERRA Model 2022A Spectroscopy Amplifier Data sheet.* 2015.

[21] CAEN S.p.A. *CAEN Model 968N Spectroscopy Amplifier Data Sheet.* 2015.

[22] AMETEK Inc. *ORTEC Model 570 Spectroscopy Amplifier Data Sheet.* 2014.

[23] Hamamatsu Photonics K.K. Electron Tube Division. *Photomultiplier Tubes R7600U series. Data sheet No. TPMH1317E02* . 2010.

[24] Yokogawa Meters & Instruments Corporation. *YOKOGAWA Digital Oscilloscope mod. DL9140 5GS/s Bulletin 7013-00E.* 2016.

[25] Tavernier S. *Experimental Techniques in Nuclear and Particle Physics.* Springer Berlin Heidelberg, 2010.

[26] Inc. Cadence Design Systems. *OrCAD Capture CIS 10.5.* 2005.

[27] Panasonic Corporation. *DZ2W047 Silicon epitaxial planar type. Data Sheet 20100202.* 2013.

[28] John G. Proakis and Dimitris G. Manolakis. *Digital Signal Processing (3rd Ed.): Principles, Algorithms, and Applications.* Prentice-Hall, Inc., Upper Saddle River, NJ, USA, 1996.

[29] National Instruments. http://www.ni.com/white-paper/4844/en/#toc2.

[30] Niels Bohr. On the constitution of atoms and molecules. Part II. Systems containing only a single nucleus. *j-PHIL-MAGAZINE*, 26:476–502, September 1913.

[31] H. Bethe. Zur Theorie des Durchgangs schneller Korpuskularstrahlen durch Materie. *Annalen der Physik*, 397:325–400, 1930.

[32] F. Bloch. Zur bremsung rasch bewegter teilchen beim durchgang durch materie. *Annalen der Physik*, 408(3):285–320, 1933.

[33] Glenn F. Knoll. *Radiation detection and measurement.* John Wiley & Sons, 2 edition, 1989.

[34] J.B. Birks. *The theory and practice of scintillation counting.* International series of monographs on electronics and instrumentation. Macmillan, 1964.

[35] S. Marrone, E. Berthomieux, F. Becvar, and et. al. Pulse shape analysis of signals from baf2 and cef3 scintillators for neutron capture experiments. *Nuclear Instruments and Methods in Physics Research Section A: Accelerators, Spectrometers, Detectors and Associated Equipment*, 568(2):904 – 911, 2006.

[36] 3M Optical System Division. *VIKUITI^{TM} ESR Brochure.* 2010.

[37] M. Gascón. *Espectroscopía gamma mediante el uso de cristales de CsI y fotomultiplicadores.* PhD thesis, USC, 2007.

[38] M. Robles. *Caracterización de una matriz de 4x4 pixeles de 3640 microceldas de SiPM.* PhD thesis, USC, 2011.

[39] Hamamatsu Photonics K.K. *Hamamatsu News 2016 Vol. 1.*

[40] R. Mirzoyan, M. Laatiaoui, and M. Teshima. Very high quantum efficiency {PMTs} with bialkali photo-cathode. *Nuclear Instruments and Methods in Physics Research Section A: Accelerators, Spectrometers, Detectors and Associated Equipment*, 567(1):230 – 232, 2006. Proceedings of the 4th International Conference on New Developments in PhotodetectionBEAUNE 2005Fourth International Conference on New Developments in Photodetection.

[41] Saint-Gobain Ceramics and Plastics. Inc. *Detector Assembly Materials. Organic Product Accessories Data sheet.* 2005-14.

[42] RTV. 681 from scionix netherlands.

[43] Cargille Meltmount^{TM}. Meltmount n = 1.582.

[44] K.G. Subhadra D.B. Sirdeshmukh, L. Sirdeshmukh. *Alkali Halides: A Handbook of Physical Properties.* Springer-Verlag Berlin Heidelberg, 2001.

[45] S.G. Lias. *Ionization Energy Evaluation.* NIST Chemistry WebBook, NIST Standard Reference Database Number 69. Eds. P.J. Linstrom and W.G. Mallard, National Institute of Standards and Technology, Gaithersburg MD, 20899.

[46] iseg Spezialelektronik GmbH. *NHQ mod. 225M High Precision Dual Channel HV Module in NIM Standard Data Sheet.* 2016.

[47] mesytec GmbH & Co. KG. *mesytec MPR-1 charged preamplifier module. Data sheet V1.3_ 01.* 2016.

[48] AMPTEK Inc. *Multichannel Analyzer 8000A Data sheet.* 2016.

[49] Inc. Canberra Industries. *Nuclear Measurement Fundamental Principles. Spectra Analysis.* 2010.

[50] A. F. Iyudin, V. V. Bogomolov, S. I. Svertilov, I. V. Yashin, N. V. Klassen, S. Z. Shmurak, and A. D. Orlov. Peculiarities of intrinsic

background in labr3: Ce and cebr3 scintillating crystals. *Instruments and Experimental Techniques*, 52(6):774–781, 2009.

[51] C. Grupen and B. Shwartz. *Particle Detectors*. Cambridge Monographs on Particle Physics, Nuclear Physics and Cosmology. Cambridge University Press, 2008.

[52] P.A. Rodnyi. *Physical Processes in Inorganic Scintillators*. Laser & Optical Science & Technology. Taylor & Francis, 1997.

[53] RS Components. *RS - 1315 Data-Logger Thermometer. Data sheet RS Stock No. 712-6039*. 2015.

[54] W. Drozdowski, P. Dorenbos, A. J. J. Bos, G. Bizarri, A. Owens, and F. G. A. Quarati. $CeBr_3$ scintillator development for possible use in space missions. *IEEE Transactions on Nuclear Science*, 55(3):1391–1396, June 2008.

[55] M. J. Kim, H. J. Kim, H. Park, K. Tanida, S. Kim, J. K. Cheon, and K. B. Lee. Scintillation properties of csi:na,^{133} ba crystal. *IEEE Transactions on Nuclear Science*, 60(2):1049–1052, April 2013.

[56] P. Belli et al. Performances of a CeF-3 crystal scintillator and its application to the search for rare processes. *Nucl. Instrum. Meth.*, A498:352–361, 2003.

[57] F. Käppeler, R. Gallino, S. Bisterzo, and Wako Aoki. The *s* process: Nuclear physics, stellar models, and observations. *Rev. Mod. Phys.*, 83:157–193, Apr 2011.

[58] IAEA: International Status and Prospects of Nuclear Power. *http://www.iaea.org/Publications/Booklets/NuclearPower/np08.pdf*.

[59] U.S. DOE Nuclear Energy Research Advisory Committee and the Generation IV International Forum. *A Technology Roadmap for Generation IV Nuclear Energy Systems*. 2002.

[60] W. Maschek, X. Chen, F. Delage, A. Fernandez-Carretero, D. Haas, C. Matzerath Boccaccini, A. Rineiski, P. Smith, V. Sobolev, R. Thetford, and J. Wallenius. Accelerator driven systems for transmutation: Fuel development, design and safety. *Progress in Nuclear Energy*, 50(2–6):333 – 340, 2008. Innovative Nuclear Energy Systems for Sustainable Development of the World. Proceedings of the Sec-

ond COE-INES International Symposium, INES-2, November 26-30, 2006, Yokohama, Japan.

[61] *The NEA Nuclear Data High Priority Request List (HPRL).*

[62] C. Guerrero, A. Tsinganis, E. Berthoumieux, and et. al. Performance of the neutron time-of-flight facility n_tof at cern. *The European Physical Journal A*, 49(2):1–15, 2013.

[63] C. Paradela. *Estudio de un monitor de neutrones para la instalacion n_ TOF.* PhD thesis, USC, 2002.

[64] C. Weiß, E. Chiaveri, and S. Girod et al. The new vertical neutron beam line at the cern n_tof facility design and outlook on the performance. *Nuclear Instruments and Methods in Physics Research Section A: Accelerators, Spectrometers, Detectors and Associated Equipment*, 799:90 – 98, 2015.

[65] S. Marrone, P.F. Mastinu, and U. Abbondanno et. al. A low background neutron flux monitor for the n_tof facility at cern. *Nuclear Instruments and Methods in Physics Research Section A: Accelerators, Spectrometers, Detectors and Associated Equipment*, 517(1–3):389 – 398, 2004.

[66] C. Weiss et al. A new CVD Diamond Mosaic-Detector for (n,α) Cross-Section Measurements at the n_TOF Experiment at CERN. *Nucl. Instrum. Meth.*, A732:190–194, 2013. [,190(2013)].

[67] Measurement and analysis of 241am(n,γ) cross sections with c6d6 detectors at the n_tof facility at cern. *Nuclear Data Sheets*, 119:72 – 75, 2014.

[68] Y. Giomataris, P. Rebourgeard, J. P. Robert, and Georges Charpak. MICROMEGAS: A High granularity position sensitive gaseous detector for high particle flux environments. *Nucl. Instrum. Meth.*, A376:29–35, 1996.

[69] D B Gayther. International intercomparison of fast neutron fluence-rate measurements using fission chamber transfer instruments. *Metrologia*, 27(4):221, 1990.

[70] L. S. Leong. *Fission fragment angular distributions cross section validation.* PhD thesis, Universite Paris Sud, 2013.

[71] U. Abbondanno, G. Aerts, F. Alvarez, and et. al. The data acquisition system of the neutron time-of-flight facility n_tof at {CERN}. *Nuclear Instruments and Methods in Physics Research Section A: Accelerators, Spectrometers, Detectors and Associated Equipment*, 538(1–3):692 – 702, 2005.

[72] L. Tassan Got. *Extraction of PPAC signals.* 2001.

[73] L. Tassan Got. Private communications.

[74] The n_TOF collaboration. *CERN n_ TOF Facility: Performance Report.* CERN INTC-2002-037, 2003.

[75] Nuclear Data High Priority Request List of the NEA (Req. ID: H.4).

[76] V. V. Verbinski, Hans Weber, and R. E. Sund. Prompt Gamma Rays from U-235 (n, f), Pu-239 (n, f), and Spontaneous Fission of Cf-252. *Phys. Rev.*, C7:1173–1185, 1973.

[77] Frances Pleasonton, Robert L. Ferguson, and H. W. Schmitt. Prompt Gamma Rays Emitted in the Thermal-Neutron-Induced Fission of U-235. *Phys. Rev.*, C6:1023–1039, 1972.

[78] I. Stetcu, P. Talou, T. Kawano, and M. Jandel. Properties of prompt-fission γ rays. *Phys. Rev. C*, 90:024617, Aug 2014.

[79] S. Lo Meo, M. A. Cortés-Giraldo, and C. et. al. Massimi. Geant4 simulations of the n_tof spallation source and their benchmarking. *The European Physical Journal A*, 51(12):1–10, 2015.

[80] Texas Instruments Incorporated. *LM6172 Dual High Speed, Low Power, Low Distortion, Voltage Feedback Amplifiers. Data Sheet SNOS792D.* 2015.

[81] Inc. Analog Devices. *AD8055/AD8056 Voltage Feedback Ampliers. Data Sheet C01063-0-2/06(J).* 2006.

[82] E.M. Henley and A. Garcia. *Subatomic Physics: Solutions Manual.* World Scientific, 2008.

[83] http://www.ensarfp7.eu/.

[84] *ENSARRoot: a virtual Monte-Carlo platform for the ENSAR community. SiNuRSE JRA05, European Nuclear Science and Applications Research (ENSAR) Project, Seventh Framework Programme of the*

European Commission (FP7). http://igfae.usc.es/ sinurse/.

[85] http:/fairroot.gsi.de/.

[86] Rene Brun and Fons Rademakers. Root - an object oriented data analysis framework. *Proceedings AIHENP 96 Workshop, Lausanne, Sep. 1996, Nucl. Inst. Meth. in Phys. Res. A*, 389:81–86, 1997.

[87] R Brun, F Bruyant, M Maire, A C McPherson, and P Zanarini. *GEANT 3: user's guide Geant 3.10, Geant 3.11; rev. version.* CERN, Geneva, 1987.

[88] S. Agostinelli et al. GEANT4: A Simulation toolkit. *Nucl. Instrum. Meth.*, A506:250–303, 2003.

[89] A Ferrari, Paola R Sala, A Fassò, and Johannes Ranft. *FLUKA: A multi-particle transport code (program version 2005).* CERN, Geneva, 2005.

[90] P. Cabanelas. Private communications.